ACOUSTIC DETERMINATION OF PRETENSIONED BOLTS

4th Semester, 3rd June 2014, Design of Mechanical Systems, Aalborg University

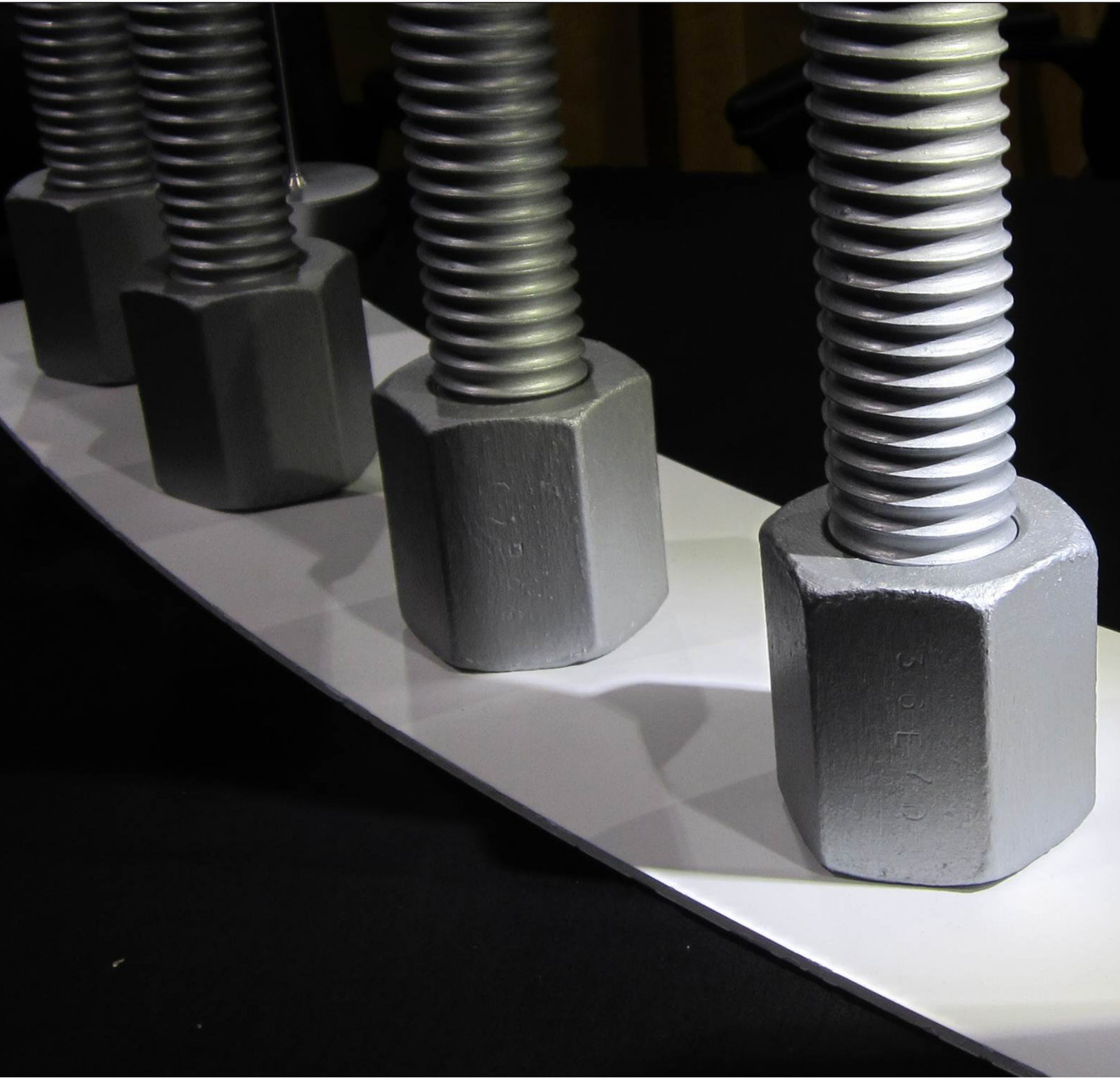

by Anders Lybæk Knudsen & Michael Mortensen

Title:
Acoustic determination
of bolt pretension

Semester:
Design of Mechanical Systems -
4th semester, spring semester 2014

Semester theme:
Master Thesis

Project period:
3rd February 2014 - 3rd June 2014

ECTS:
30

Supervisor:
Sergey Sorokin

Project group:
Michael Mortensen
Anders Lybæk Knudsen

Study Board of Industry and Global Business Development
Fibigerstræde 16
DK - 9220 Aalborg East
Phone +45 99 40 93 09
lft@m-tech.aau.dk
www.ses.aau.dk

Synopsis:
This project contains experiments and analysis of the acoustical response of bolted joints. Initially experiments have been performed to obtain the response of a bolted joint, under different levels of pretension. The purpose of this is to determine if there is a change in the response of the structure, related to this change in pretension, and whether this is acoustically measurable. It has been found that there is a clear shift, in the resonant frequencies of the structure, when pretension is changed. To find the cause of this shift, a FE model of the bolt has been established, and it was found that changes in boundary conditions are causing the shift in resonant frequencies. In order to validate this hypothesis, further experiments is carried out on different bolt sizes, followed by a more detailed FE model, and an analytical model. It is concluded that it is possible to use acoustic measurements to determine if a system is properly pretensioned, but to mature the method further investigations has to be made.

Michael Mortensen

Anders Lybæk Knudsen

Copies: 6
Number of pages: 71
Appendix: 42 pages and an Appendix CD

By signing this document every group member confirms that everyone has participated equally in the project work, and everyone hereby are responsible for the content of this report.

Preface

This Master's thesis is the documentation of the work carried out from February 3^{rd} 2014 to June 3^{rd} 2014 on the fourth semester of the Mechanical Engineering curriculum for the master program in Design of Mechanical Systems at Aalborg University. The project has been supervised by professor, D. Sci. ,Sergey Sorokin. The work carried out represents 30 ECTS points per student.

The topic for the thesis is proposed by the company Brüel & Kjaer in the framework of MAKUNET. The supervisor from Brüel & Kjaer is Research Engineer, Ph.D., Dmitri Tcherniak. A CD is appended with results, MATLAB-, ANSYS-scripts, and a digital copy of the report. References are made during the report to the CD and the folder path that contains the referenced data is listed in a footnote. A digital version of the report is found on the Appendix CD. The picture used on the front page is found in Rust Bullet [2014].

References in the report are cited in accordance with the Harvard Referencing System. This implies that, sources are cited by author's surname and year of publication, outside text; [surname,year], inside text; surname [year]. Full references to the corresponding sources are found in the reference list at the end of the main report. Abbreviations created during the report are stated by the whole word or term first time it occurs and is followed by the abbreviation given in parenthesis, e.g. Design of Mechanical Systems (DMS). A list of nomenclature is presented, that describes the most commonly used symbols throughout the report.

The authors would also like to thank research assistant, Ph.D., Radoslav Darula, for the help provided with setting up, and evaluating the tests performed in the laboratory.

Abstract

Formålet med dette projekt er, at vurdere hvor vidt det er muligt at bestemme forspændingen i boltene i en boltesamling. Projektet er foreslået af Brüel & Kjær, som en del af MAKUNET. Baggrunden for problemstillingen er, at der ved eksitering af to identiske bolte under forskellig forspænding, afgives et hørbart forskelligt akustisk signal. Dette har antydet at det kunne være muligt at anvende akustiske signaler til bestemmelse af forspænding, hvilket kan lette arbejdet i forbindelse med inspektioner af boltede samlinger. I løbet af dette projekt er årsagen til denne forskel i den afgivne lyd undersøgt, og det er søgt at afdække hvor vidt det kan gøres praktisk anvendeligt.

Projektet er indledt ved at lave en række initierende forsøg, for at fastlægge hvor vidt målbare forskelle i responsen, af en 140mm M12 bolt ved forskellige forspændinger, kan opfanges. Forsøgs resultaterne opsamles akustisk med en mikrofon samt mekanisk via accelerometre, til eksitering af boltene anvendes en modal hammer med indbygget kraft transducer. Indledningsvist er der anvendt en opsætning med flere bolte, men for at simplificere responset der analyseres er der i hoveddelen af projektet anvendt en opstilling med blot en enkelt bolt. Ud fra forsøgene er det fundet, at resonans frekvenserne for strukturen stiger i takt med at forspændingen øges, dette gør sig gældende for både stål og aluminiums strukturer. I forbindelse med dette er også indflydelsen af spændskiver undersøgt, hvilket dog viste sig at være uden betydning for responsen. Ligeledes er det undersøgt om dæmpning vil kunne anvendes som mål for forspændingsgraden, hvilket dog kunne afvises.

Eftersom det er blevet konstateret at det er muligt, at se en ændring af resonans frekvenserne, når forspænding øges, er mekanismen bag denne ændring blevet undersøgt. Da ændringen i frekvenser er så stor, at den ikke kan forklares med ændringer i stivheden, er det i stedet undersøgt hvor vidt ændringer i systemets randbetingelser, kan være årsagen til de observerede skift i resonans frekvenser. For at undersøge dette, er der opstillet en FE model af bolten for to forskellige randbetingelser, simpelt understøttet og fast indspændt, analysen af disse modeller viste, at den ændring der kunne observeres mellem de to modellers egenfrekvenser, stemte godt over ens med de eksperimentielle resultater. For at undersøge hvor vidt de fundne resultater også er gældende for andre størrelser af bolte, er både M18 og M24 bolte undersøgt eksperimentielt, og samme tendenser som for M12 bolte kunne observeres.

En mere avanceret FE model opstilles for at se om forskellen mellem den simple FE og Test bliver mindre og for at forklare resultaterne fra M18 og M24 forsøgene. Den avancerede model bliver løst både for egenfrekvenser og for harmonisk respons. Resultaterne for egenfrekvenserne viser en mindre forskel mellem FE og tests end den simple FE model. Det tyder på at der en svag kobling mellem bolten og strukturen. Den harmoniske model viser at der er stor forskel på amplituden af bolten og amplituden af målepunkterne på strukturen. Derudover er der stor forskel på amplituden af bolten og amplituden af målepunkterne for de forskellige bolte og forskellige resonans frekvenser. Derfor konstrueres der en analytisk model der skal forsøge at beskrive dette problem.

Den analytiske model bliver anvendt til at beskrive hvor meget energi der bliver overført fra bolten til strukturen og hvor stor indflydelse dæmpning har på denne overførsel af energi. Den analytiske model er udledt ud fra Hamilton's principle og Timoshenko bjælke teori. Modellen viser at dæmpningen har meget lille indflydelse på responset målt på strukturen og at meget lidt af det indførte energi fra lasten bliver overført til strukturen.

Ud fra resultaterne i projektet, har det vist sig at det bør være muligt, at anvende akustiske målinger til at bestemme hvor vidt bolte i en samling er spændt tilstrækkeligt.

Contents

Nomenclature

Symbol:	**Description:**	**Unit:**
A_b	Cross sectional area of the bolt	$\left[mm^2\right]$
A_c	Cross sectional area	$\left[m^2\right]$
A_i	Amplitude at point i	[-]
A	Area	$\left[mm^2\right]$
C_i	Constant	[-]
E	Modulus of Elasticity	[GPa]
F_{pt}	Clamping force exerted by the pretension	[N]
F	Force	[N]
G	Shear modulus	[GPa]
I	Area moment of inertia	$\left[m^4\right]$
L	Length	[m]
P_t	Prestress in the bolt in percent	[-]
Q_r	Quality factor at resonance	[-]
Q_{hp}	Half power of the quality factor at resonance	[-]
S_p	Proof strength of bolt	[MPa]
S_c	Compresive strength	[MPa]
S_t	Tensile strength	[MPa]
T_{cf}	Torque required for the desired clamping force	[Nm]
T	Kinetic energy	[J]
V	Potential energy	[J]
ΔW_d	Dissipated energy	[J]
α	Angle	[deg]
β	Constant	$\left[\frac{1}{m}\right]$
δ	Variation	[-]
ε	Strain	[-]
ν	Poison's Ratio	[-]
ω_d	Damped eigenfrequency	$\left[\frac{rad}{s}\right]$
ω_i	Frequency at point i	$\left[\frac{rad}{s}\right]$
ω_n	Undamped Eigenfrequency	$\left[\frac{rad}{s}\right]$
ω_r	Resonant frequency	$\left[\frac{rad}{s}\right]$
ω_{R1}	First half power point	[Hz]
ω_{R2}	Second half power point	[Hz]

Continued on next page

Symbol:	**Description:**	**Unit:**
ω	Frequency	$\left[\frac{rad}{s}\right]$
$\psi(x,t)$	Angular displacement of a Timoeshenko beam	[-]
ρ	Density	$\left[\frac{kg}{m^3}\right]$
σ	Stress	[MPa]
ζ	Damping ratio	[-]
c_c	Critical damping constant	$\left[\frac{N\,s}{m}\right]$
c	Damping constant	$\left[\frac{N\,s}{m}\right]$
d_b	Diameter of bolt	[mm]
d	Diameter	[m]
f_r	Undamped resonant frequency	[Hz]
f	Frequency	[Hz]
k_{sg}	Gauge factor	[-]
k	Spring constant	$\left[\frac{N}{m}\right]$
m	Mass	[kg]
t	Time	[s]
$w(x,t)$	Deflection along the length of the beam	[m]
$z(t)$	Mass deflection	[m]

1

Introduction

One of the main challenges in constructing mechanical systems, is to join different components. One way of assembling components is via a bolted joint, where a suitable number of bolts is used to secure two surfaces through tightening of the bolts. Bolted joints are widely used for joining all sorts of constructions and are considered classical machine elements. The advantage of assembling parts in this way, is that the joint is easily separated and assembled again, which is why bolted joints are widely used. Bolted joints are seen every day and some common joints are the mounting of rims on cars, combustion engines cylinder heads, steel bridges, and the assembly of airplanes. An airplane like the Boeing 747, which has been the worlds largest airplane, uses about 2.5 million fasteners [Norton, 2006].

When a bolted connection is assembled, the bolts in the assembly are tightened to a much higher degree, than what is required to simply hold the joint together. This is known as pretensioning the bolts, and creates friction which counteract forces trying to shear joint apart, but more importantly greatly increases the bolts resistance to dynamic loading. As most structures are exposed to some sort of dynamic loading, this is a very important aspect of bolted joints.

Considering a simple bolted joint shown on Figure 1.1, the reason for the increased resistance towards dynamic loading can be explained, using a bolt pretension diagram.

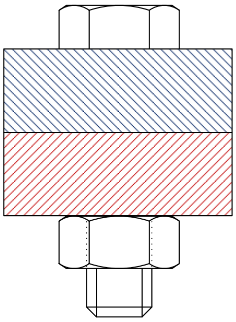

Figure 1.1 A bolted joint connecting 2 materials

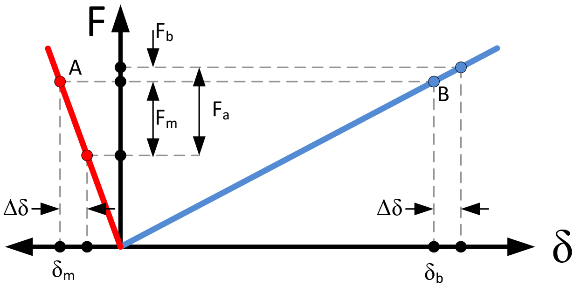

Figure 1.2 Bolt pretension diagram showing the deflection on the bolt and the surrounding material

A bolt pretension diagram is shown in Figure 1.2, and is a method for showing how the pretension load is distributed between bolt and surrounding material. To the right of the y-axis, indicating the applied force, the relation between elongation of the bolt and the applied force. The bolt stiffness is seen from the slope of the curve. To the left of the y-axis the stiffness of the clamped material in the joint is seen. The reason for the two components being on different sides of the y-axis is that, as the bolt is tensioned, it is elongated, while the clamped material is compressed. Note that the slope is steeper for the material than for the bolt, indicating that the area of the material in compression is larger than the cross sectional area of the bolt.

In the bolt pretension diagram shown in Figure 1.2 the bolted joint is subjected to a Force F_a. The force introduce an additional displacement $\Delta\delta$ in the joint and affecting both the clamped material and the bolt. From the bolt pretension diagram in Figure 1.2 it is seen, that the bolt is loaded very little and the material is unloaded more, absorbing much of the applied load. Thus the bolt experiences very little extra load, making the joint very strong to fatigue due to the amplitude of stress in the bolt being very small, and the variation in the clamped material being in compression. This makes a bolted joint very attractive when the bolts are pretensioned, especially compared to welding where fatigue can be much harder to avoid.

The benefits gained from pretensioning the bolts require that a sufficient level of pretension is reached. A bolt is usually pretensioned to either 70% or 90% of the bolts proof strength, depending on the application. If the bolt is pretensioned to 90%, it is only possible to use the bolt once and the bolt is scrapped if the joint has to be separated. A bolt pretensioned to 70% is able to be used several times. During a structure's lifetime it is possible that some bolts are loosened, for example due to vibrations in the structure, resulting in a decrease in the pretension, which can lead to failure of bolts or even the entire structure.

To avoid breakdown due to untightened bolts, bolted joints often contain several bolts more than required from a structural point of view due to safety. However it is necessary to be able to check the level of pretension of the bolts in a structure. This can be easy to do on for example the wheel nuts on a car or a truck, using a torque wrench, but when going to a larger scale for example the joint between the foundation and the tower of a wind turbine it becomes much more complicated and time consuming. Thus methods for determining the pretension in a simpler manner are desirable, as they might save a lot of time on maintenance and might even make it possible to reduce the number of extra bolts included for safety reasons.

Other methods for examining the pretension exists, fx. ultrasonic inspection. This does however require specialized personnel and equipment. Based on the observation that there is a change in the acoustical emission between a tightened and untightened bolt, Brüel & Kjær A/S has suggested that there might be a way to determine bolt pretension using microphone measurements.

This project seeks to investigate whether acoustical measurements can be used to determine the pretension in bolts. This would mean, that by positioning a microphone correctly and hitting a structure at a given location, with an impact hammer, it would be possible to check whether a bolt is sufficiently tightened. This would allow for a much faster determination of which bolts in a structure need tightening, and reduce the need for a torque wrench, as it only has to be applied for tightening the bolts, where it is actually needed.

Some work in regards to the acoustical response of bolt under pretension has been performed as described in Knudsen [2013]. This project builds on some of the experiences obtained in that project, where it was found that an increase in the first resonant frequency in a pretensioned bolt is observable. The purpose of this project is to uncover the mechanisms that cause this change and to determine whether it is feasible to use acoustical measurements to determine pretension for industrial purposes.

Preliminary work
2

To gain an understanding of why the acoustical response of a bolted connection changes, for different levels of pretension in the bolts, some initial work is required. The purpose of this chapter is to describe the preliminary work, which consists of a series of experiments designed to gain an understanding of the problem. The results found during the preliminary work, will serve as a foundation for the further work in the project where the phenomenon is modeled and methods for practical estimation are investigated.

Some work in relation to acoustical response of pretensioned bolts has already been performed as described in [Knudsen, 2013]. However a model describing the correlation between pretension and acoustical response was not established. In that project an aluminum cylinder with four holes for bolts was examined, in order to have a starting point for the experiments in this project, a similar structure is manufactured and tested. The working drawing for this component can be found in Appendix B named multibolt.

The structure is tested by hitting with an impact hammer at the structure, and at the bolt head of four 140mm M12 bolts, which have been applied different levels of pretension as shown on Figure 2.1 and 2.2. The response is captured using a microphone and two or three accelerometers, depending on the desired results.

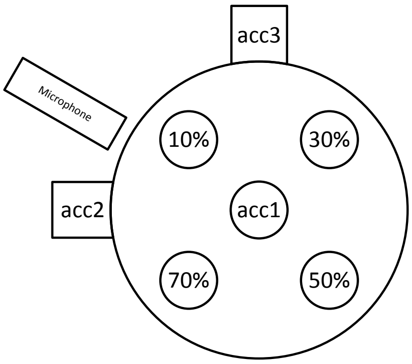

Figure 2.1 Simplified model of the placement of the bolts, accelerometers and microphone.

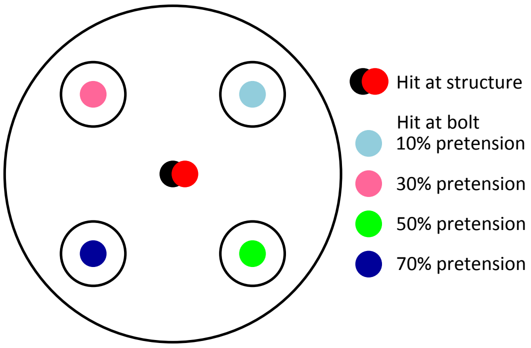

Figure 2.2 Location of the points to be hit with the impact hammer.

The physical test setup can be seen in Figure 2.3, the equipment and data acquisition setup will be described in detail later, in Section 2.1.

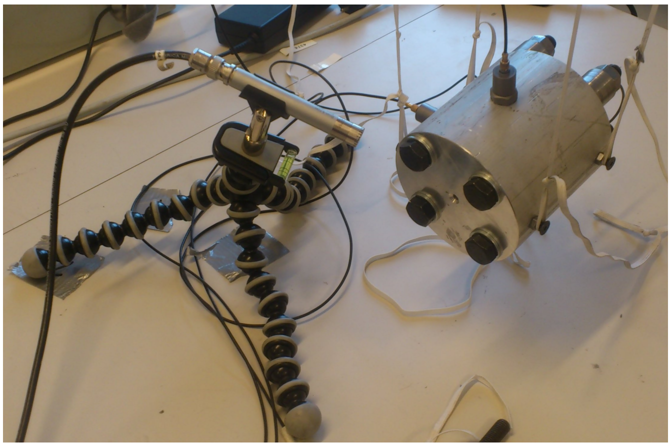

Figure 2.3 Setup for multibolt experiment.

In Figure 2.4 and 2.5, the Frequency Response Function (FRF) obtained with accelerometer 2 can be seen, for hits on the structure and the bolts respectively. It can be seen from Figure 2.4 that there is a clear difference in the response of the structure with and without bolts. Especially around 3kHz there are a series of sharp peaks, indicating that there are resonances of bolts in this frequency range.

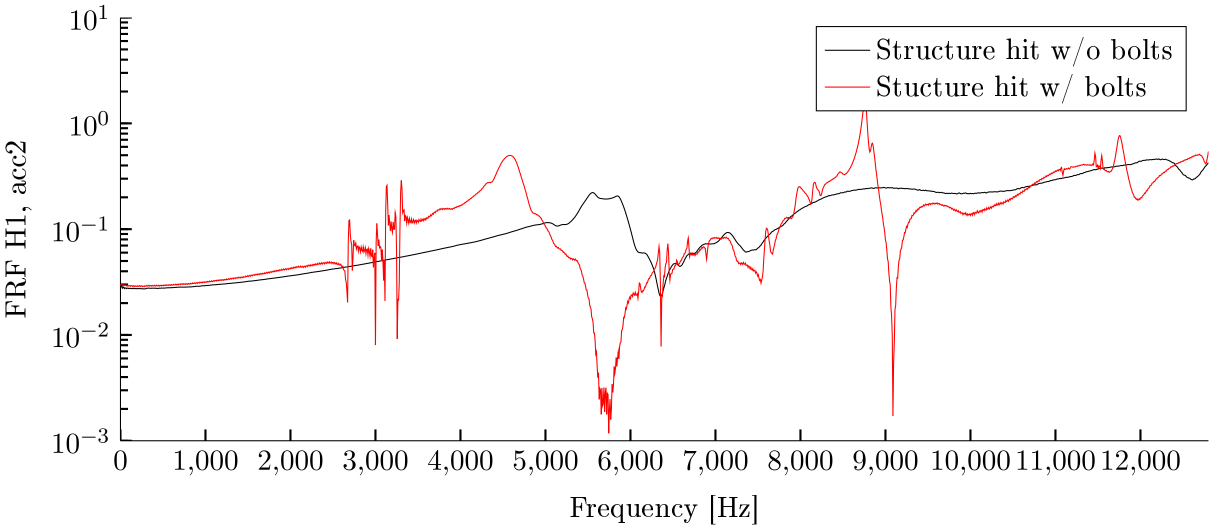

Figure 2.4 Frequency response H1, with acc2, for structural hits.

In Figure 2.5 a closeup of the frequency range of interest can be seen. Here the change in frequency response when hitting different bolts can be seen. It can be seen that hitting a certain bolt accentuates a specific peak, indicating that each peak is associated with a specific bolt. However it is not clear how much influence the distance from the bolt being hit to the accelerometer has, as well as how the bolts affect each others response.

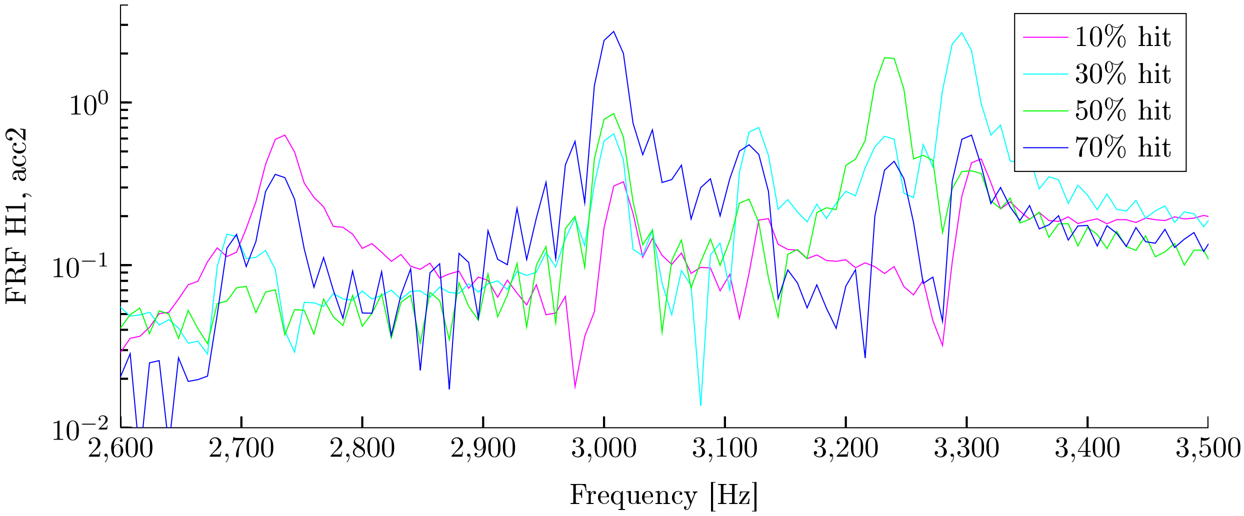

Figure 2.5 Frequency response H1, with acc2, for bolt hits.

What can be concluded from this test, is that it is possible to see and separate the resonances of bolts under different levels of pretension in the same structure. However the mechanics describing the behavior need to be determined, in order to be able to distinguish the pretension of the individual bolts in such a structure. Thus the structure needs to be simplified, in order to gain a better understanding of the effects of bolt pretension.

This new and simpler system contains only a single bolt, which will be tested under various levels of pretension. In the new system, a cylindrical block of material is manufactured with a hole in the center for mounting a 140mm M12 bolt. Drawings for this part can be found in Appendix B named singlebolt. As only a single bolt is present, in this setup it is possible to investigate the changes in response in more detail, and eliminate problems regarding changes in the setup, such as distance between accelerometers and the bolt.

2.1 Test setup

In this section the basic test setup used throughout the project is described. As described, the tests are performed for a cylinder containing a single pretensioned bolt. This cylinder is suspended by four elastic strings attached to the ceiling of the lab, to give the system as compliant boundary conditions as possible. The strings are attached to the cylinder by four small screws protruding from the side of the cylinder, as shown on Figure 2.6.

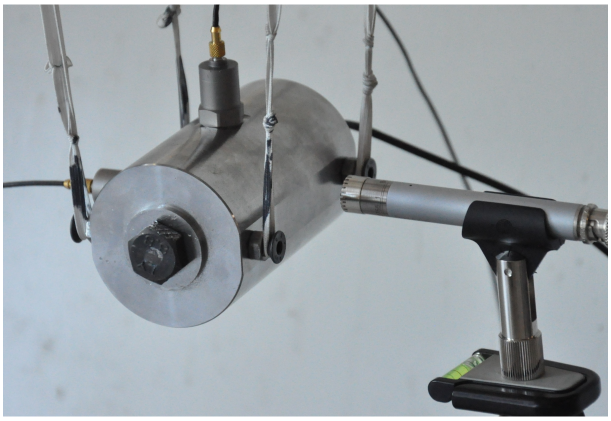

Figure 2.6 Basic test setup.

To pretension the bolts to the desired level, a torque wrench is used to tighten the bolts. However, as torque wrenches are not very precise when used for pretensioning and as the level of pretension in the bolt is vital to the measurements, a force transducer is used to check clamping force exerted by the bolt on the structure. From this force, the pretension in the bolt can be calculated. In Appendix A the method for calculating clamping force and required torque for pretensioned bolts is described. As no suitable transducer is available at institute of Mechanical and Manufacturing Engineering, a transducer is manufactured for the specific purpose of determining the clamping force, which is described in detail in Appendix A.1.

In order to imitate a regular bolted connection, a washer is placed between the bolt head and the cylinder, between the cylinder and the nut a force transducer, which has the same inner and outer diameter as a standard washer, is placed.

2.1.1 Measurement equipment

To obtain the response of the system, a Brüel & Kjær (B&K) Pulse 3560C dual channel FFT analyzer, and the software PULSE, is used to find the Frequency Response Function (FRF). For the system input signal a Endevco impact hammer is used and for the system output, a microphone and two accelerometers are used. Detailed information of the used equipment, such as type and serial number for the individual items is found in Appendix C.

The specific equipment, its usage, and positioning will be described in the following, along with the reason for choosing it.

Impact hammer

To excite the structure an impact hammer is used. At the start of the project a B&K 8202 steel tipped impact hammer was used. However after the first couple of tests a malfunction of the force transducer in the hammer occurred, and thus it was necessary to find a replacement, which is an aluminum tipped Endevco 2302-10 impact hammer. Due to the change of hammer and especially the material of the tip, a different range of frequencies can be exited. This is relevant as it was easier to hear the difference in pretension for hits with the aluminum tipped hammer, which is suspected to be caused by the lower cutoff frequency of the aluminum tip, i.e. the frequency where the force signal is at its lowest, indicating that the frequencies of interest lies below 9kHz.

To test this hypothesis a series of tests were performed, looking at only the autospectrum of the structure. As it can be seen from Figure 2.7 and 2.8, no significant change occurred with respect to the location of the resonance peaks. The amplitude of the signal changed which is natural as the autospectrum is dependent on the impact force and thus does not indicate a change in response due to change of the tip material.

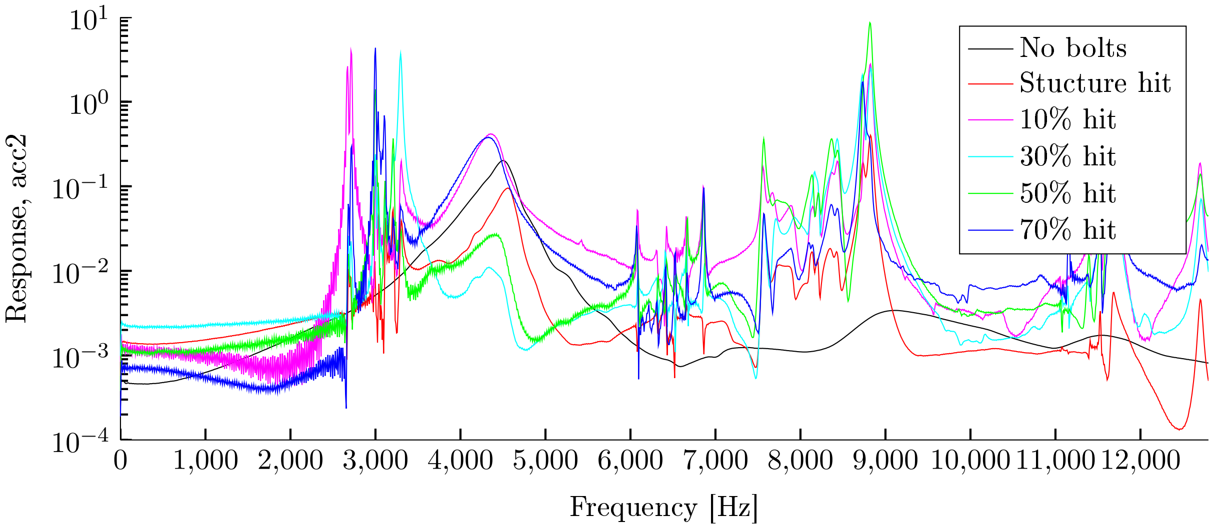

Figure 2.7 Response obtained with accelerometer 2 for the steel tipped hammer.

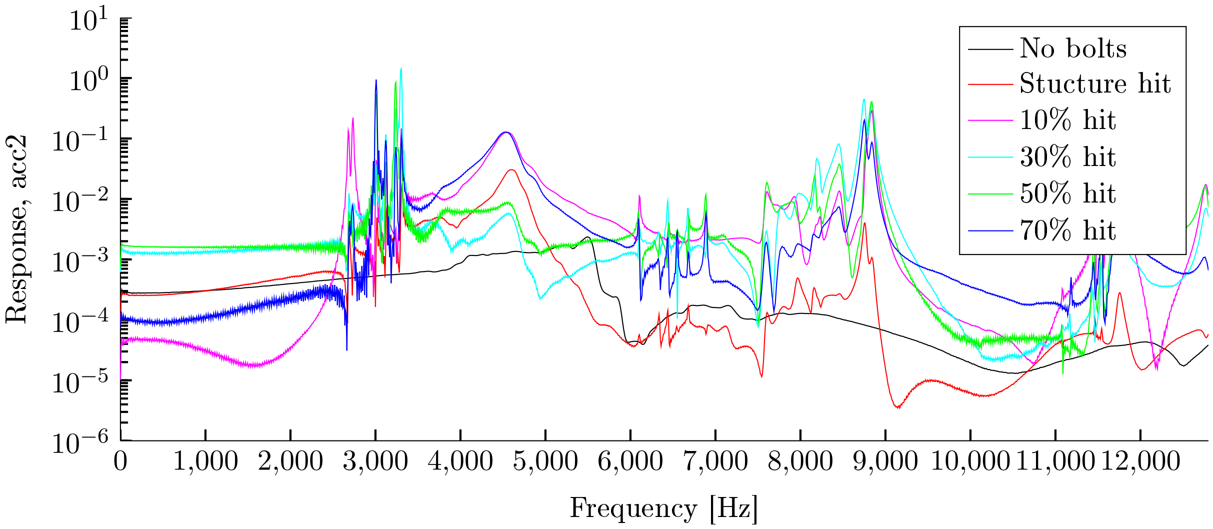

Figure 2.8 Response obtained with accelerometer 2 for the aluminum tipped hammer.

As no significant change was introduced by the hammer change, the aluminum tipped hammer will be used henceforth, expecting neither better nor worse excitation of the structure.

Accelerometers

To obtain the response of the structure, caused by the impact from the hammer, accelerometers are used. The reason for using both accelerometer and microphone measurements, is that since the accelerometers are in direct contact with the structure, the motion is directly measured, and also acoustical noise from the environment is disregarded in the obtained response. Thus the accelerometers can be used to better understand what to look for in the response when evaluating microphone measurements.

In order to get usable readings from the accelerometers, choosing the correct position and type of the accelerometers is critical. To determine the best positions for the accelerometers, they have initially been positioned orthogonally on the structure as shown on Figure 2.9, and then moved axially along the surfaces to find where the response is largest. The further the accelerometer was placed from an edge the better results were obtained and therefore all accelerometers are placed as close to the middle of the surface as possible. The designation, acc1, acc2 and, acc3 for the accelerometer names will be used henceforth to refer to the specific accelerometers, regardless of the actual number of accelerometers used in a given test.

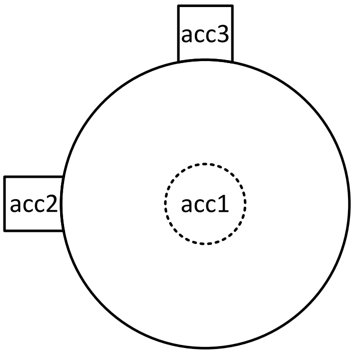

Figure 2.9 Orthogonal placement of accelerometers.

Initially type 4374 accelerometers were placed on the cylinder, however these were not sensitive enough, resulting in an extremely noisy signal. Thus to get better results, more sensitive accelerometers were tested, for acc1 a type 4384V accelerometer gives sufficient sensitivity, but for acc2 and acc3 type 4382V are required for satisfactory readings. Besides the increased sensitivity, the type 4384V and type 4382V accelerometers have the advantage of having a threaded hole for mounting onto the structure, making it possible to assure the position of the accelerometer is always the same, where the type 4374 have to be mounted using for example bees wax.

As the Pulse 3560C analyzer only has four slots for signal inputs, and the hammer and microphone each takes up one slot, there are only two slots for accelerometers. Thus it is necessary to determine which of the accelerometers to remove from the test setup. To determine this, the results of the test used to evaluate the tip of the hammer in Section 2.1.1 are used. These tests have been performed in the setup with four bolts, using three accelerometers as the hammer signal was removed due to the defect force transducer. In Figure 2.10, 2.11, and 2.12 the response obtained for each accelerometer, when the structure is hit at the 70% pretensioned bolt can be seen. As it can be seen from the figures, acc1 does not capture the resonances at around 3kHz which is why this accelerometer is removed from the setup.

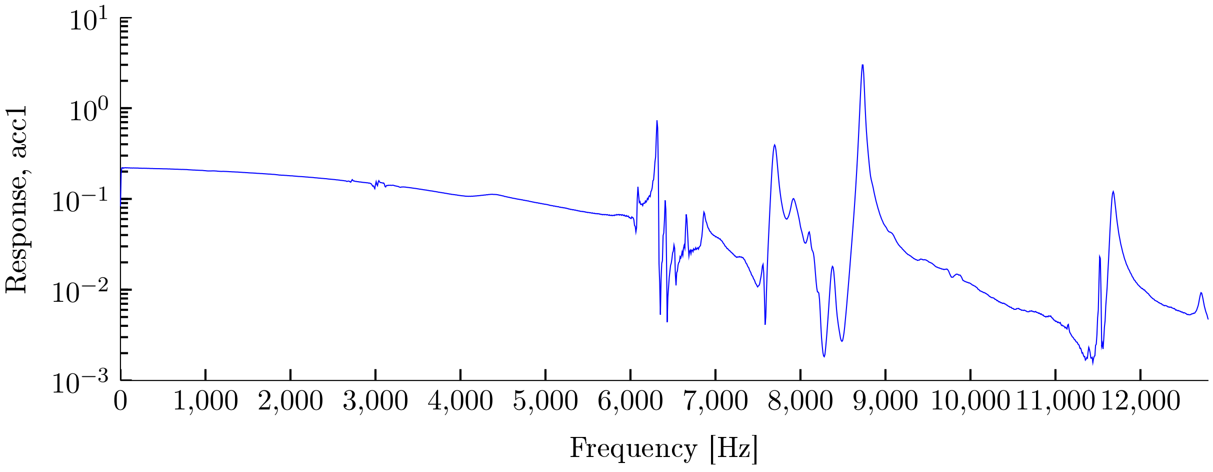

Figure 2.10 Response obtained with accelerometer 1.

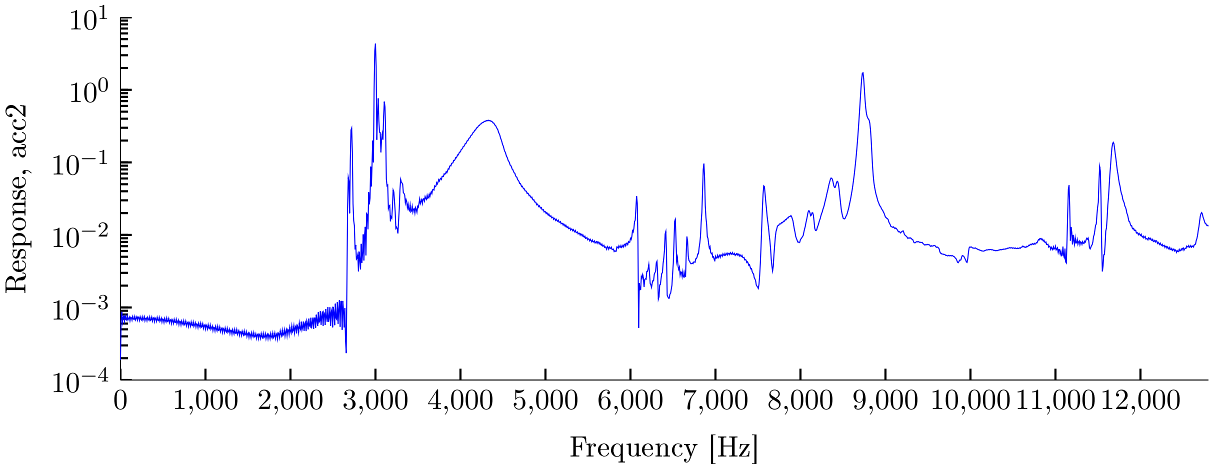

Figure 2.11 Response obtained with accelerometer 2.

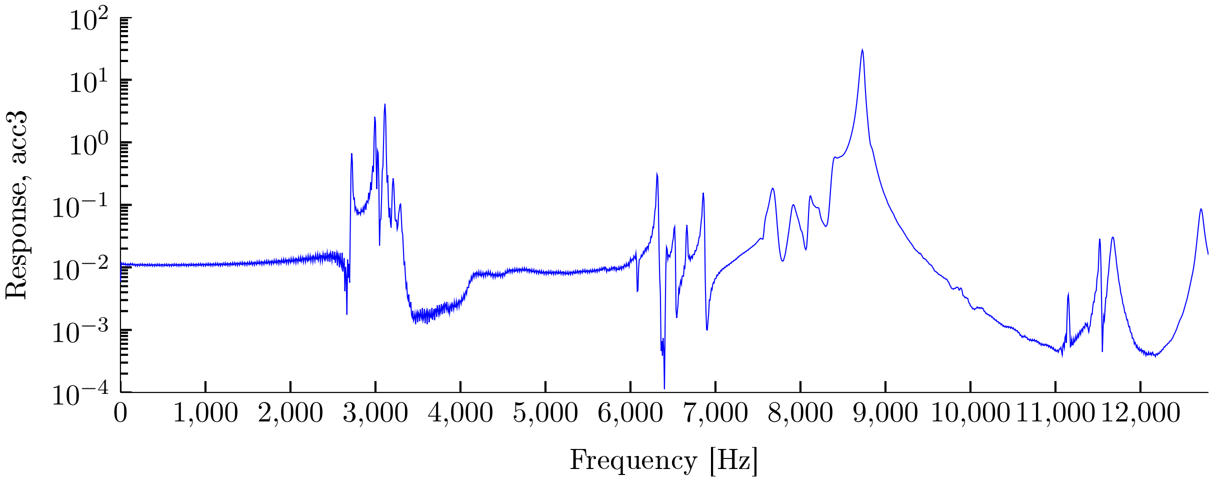

Figure 2.12 Response obtained with accelerometer 3.

Microphone

To capture the acoustical response a half inch microphone of type 4189 is used. As the quality of acoustical response is paramount for the project, it is important that the microphone is positioned correctly. Therefore different positions of the microphone have been tested, for a bolt pretensioned to 80%. In Figure 2.13, 2.14, and 2.15 the different positions can be seen, and in Figure 2.16, 2.17, and 2.18 the measured response from the microphone can be seen with the corresponding accelerometer measurement. Here it is obvious that the microphone at position 3, captures the response far better than the others, thus this is the position that will be used for the setup.

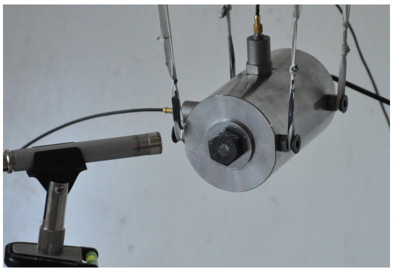

Figure 2.13 Mic position 1.

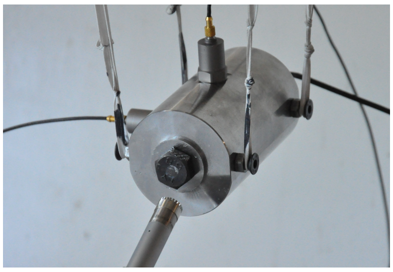

Figure 2.14 Mic position 2.

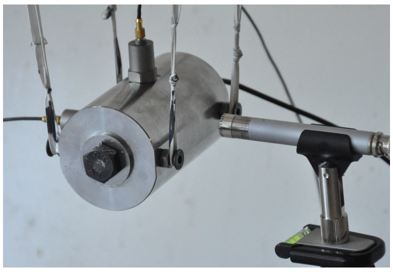

Figure 2.15 Mic position 3.

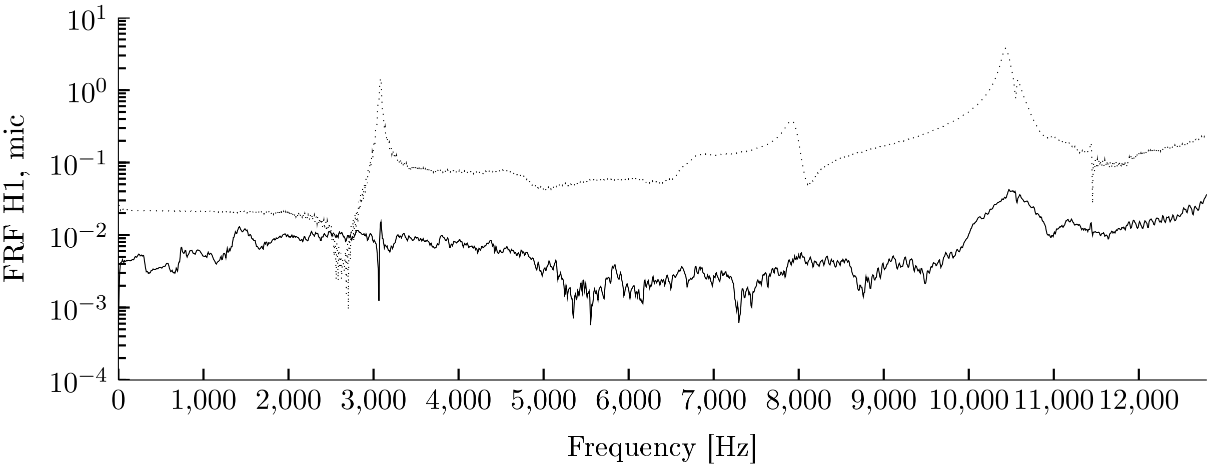

Figure 2.16 Response obtained with the microphone at position 1.

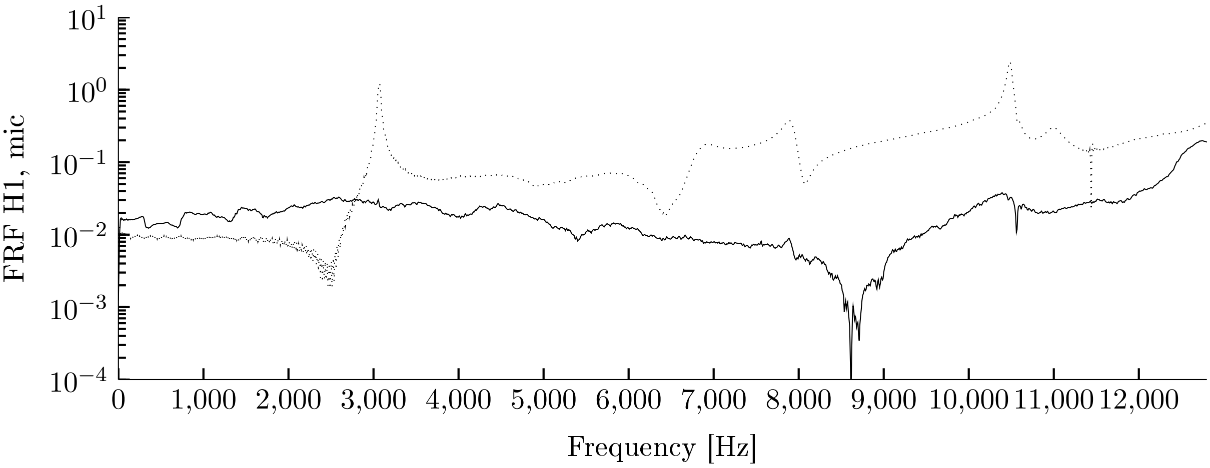

Figure 2.17 Response obtained with the microphone at position 2.

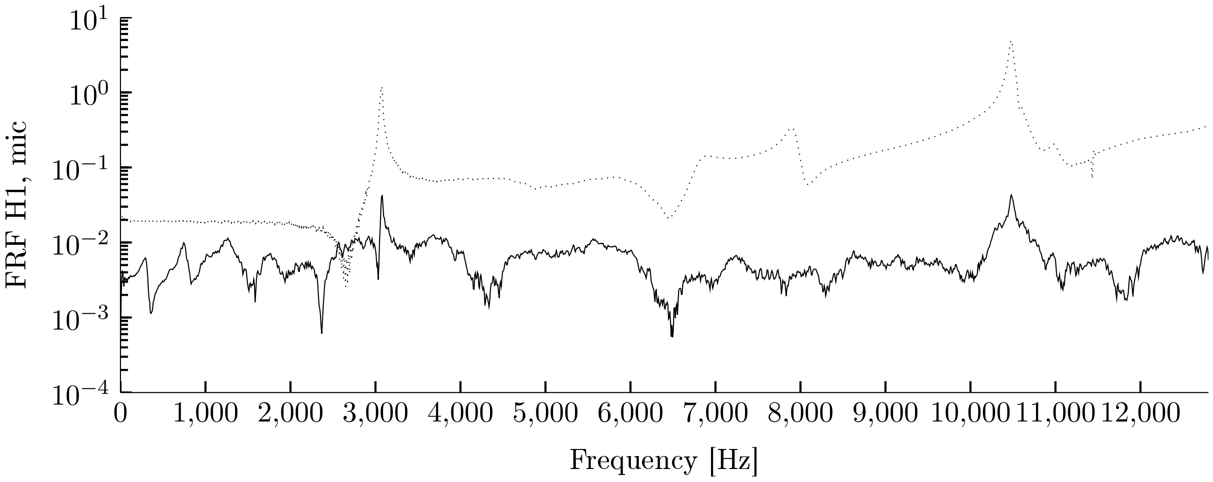

Figure 2.18 Response obtained with the microphone at position 3.

2.1.2 Pulse software setup

As previously stated, the software Pulse is used for the data acquisition and processing. The program used to handle the input is called labshop and is set up in the following way.

- A blank project is created
- The equipment described in Section 2.1.1 is added in the configuration organiser.
  - The hammer signal is set to input port 1
  - The microphone signal is set to input port 2
  - The accelerometer 2 signal is set to input port 3
  - The accelerometer 3 signal is set to input port 4
- These are then configured and calibrated under signals in the measurement organiser.
  - The peak inputs for the signals are adjusted using the levelmeter. The max peak input is set as close as possible to the maximum received value, from the system response, without getting overloaded.
- A group is added for each type of equipment in the measurement organiser, e.g. a hammer, a microphone and, an accelerometer group, each containing the relevant signals.
- Under setup in the measurement organiser, an FFT analyzer is set up.
  - The FFT analyzer i setup for baseband analysis in a frequency range of 0-12.8kHz divided into 1600 lines, as this is the highest resolution allowed by the duration of the structural response, this results in a resolution of 8Hz in the frequency domain.
  - The obtained response is averaged linearly over ten hits on the structure.
  - The analyzer is triggered by the signal of the hammer going above a certain threshold.
  - In the spectra section of the FFT properties, the analyzer is set to measure all auto- and cross-spectra.
  - The time weighting window is set to exponential, for the acceleration and microphone signals, and to transient for the hammer signal.
- A time capture analyzer is added in the measurement organiser containing all the equipment groups, in order to have the time data should additional post-processing become necessary.

- In function organiser groups are made for autospectrum, frequency response H1, compressed and expanded time, and an export group.
    - The purpose of the export group is to extract:
        - Frequency response H1 for accelerometer 2 with respect to the hammer signal
        - Frequency response H1 for accelerometer 3 with respect to the hammer signal
        - Frequency response H1 for microphone with respect to the hammer signal
        - Autospectrum for the hammer
    - Extracted files are saved as .uff files and can be used in matlab.

After each test is performed, the measurements are saved and named after the pretension in the bolt, for example a test of the structure with a 60% pretensioned bolt is called 60hit, while one with 70% is called 70hit and so on. Each Pulse file contains only a single series of experiments to avoid files becoming too large. All result files from experiments can be found on the Appendix CD[1].

2.2 Frequency response determination

Using the setup established in Section 2.1, a series of tests are performed to determine the change in response of the system when the pretension of the bolt is changed. To accomplish this the response of the structure is tested for pretension ranging from 10% to 90% with an interval of 10%. The structure used in [Knudsen, 2013], and for the initial tests, is made of aluminum, however the majority of bolted structures are made from steel. To make sure that the results found are not only applicable to an aluminum structure, a cylinder of both steel and aluminum is manufactured and tested, allowing for a more robust model of the system.

In Figure 2.19 and 2.20 the response obtained with acc2 can be seen for the steel and aluminum structure respectively. In the plots, the response of the structure is plotted with a different line for each pretension level. It can be seen that the first resonances for the steel structure lies in the 3kHz region while its around 4kHz for the aluminum structure. It is also evident that the measurements for 10% pretension, and to some degree for 20%, deviates from the rest of the measurements, which behaves in more or less the same way.

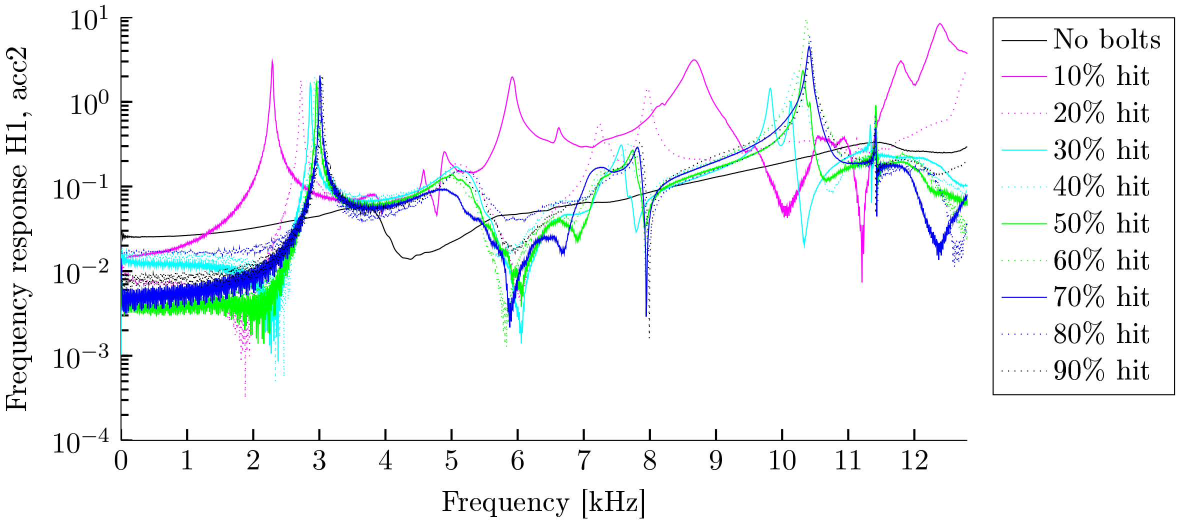

Figure 2.19 Response obtained with acc2 for the steel structure.

---

[1] Appendix CD\Test Results

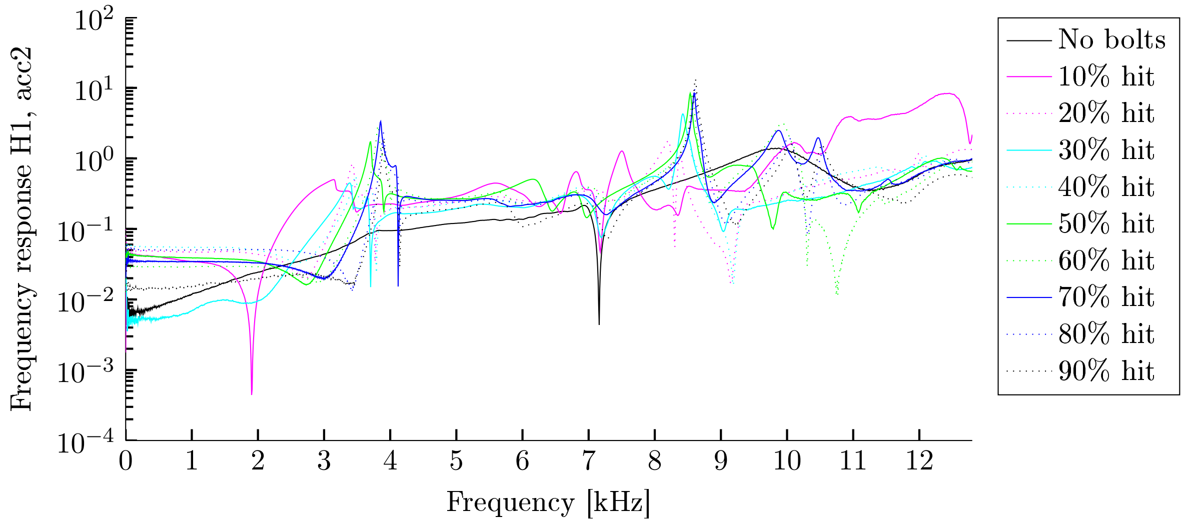

Figure 2.20 Response obtained with acc2 for the aluminum structure.

To get a better idea of the change introduced by the increasing pretension, a closeup of the region of the first resonances is evaluated. In Figure 2.21 a closeup of the first group of resonance peaks is seen. As it can be seen from the figure, the peaks are moving to higher frequencies when the pretension is increased, this is also seen at the higher order eigenfrequencies for both steel and aluminum. In Table 2.1 the location of the first eigenfrequencies, obtained with acc2, can be seen. For the response of the steel structure, a steady increase can be observed from 30% pretension and up, and from 50% for the aluminum structure, each of approximately 200Hz.

Measurement	**10%**	**20%**	**30%**	**40%**	**50%**	**60%**	**70%**	**80%**	**90%**
Acc2 steel	2288	2720	2864	2928	2960	2984	3008	3024	3040
Acc2 aluminum	3144	3432	3384	3480	3704	3816	3856	3896	3896

Table 2.1 Location of the first resonance peak for a given level of pretension, from acc2 measurements.

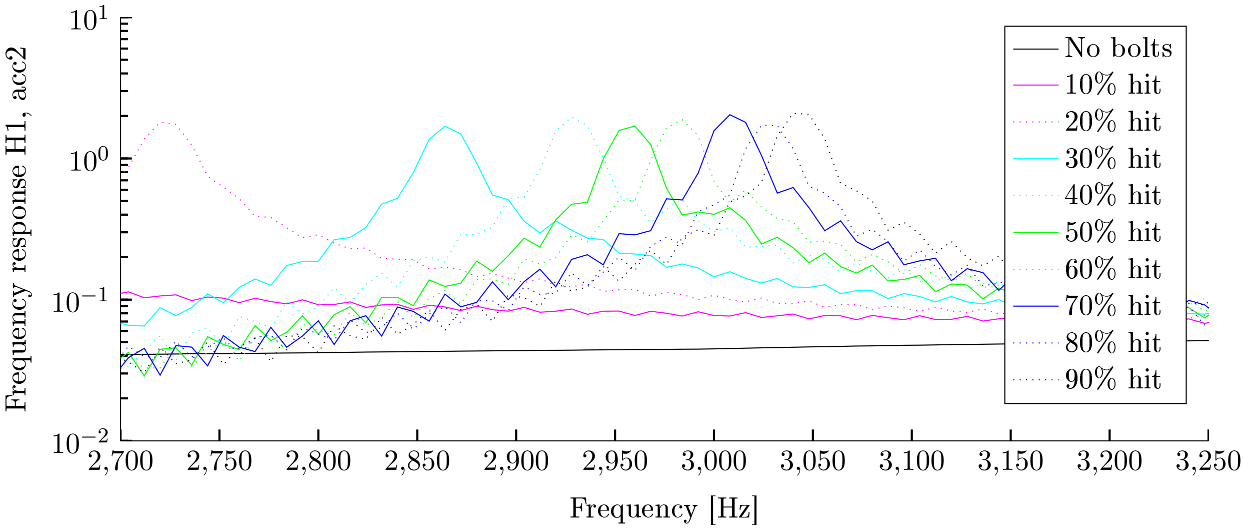

Figure 2.21 Response obtained with acc2 for the steel structure.

In Figure 2.22, the acoustical response for the steel structure can be seen. The first group of resonances is captured well by the microphone, as seen by the series of sharp peaks around 3kHz. The resonances associated with higher eigenmodes are however not captured as well, although an increased response can be observed at around 10kHz, no sharp peaks are present. Whether the lack of sharps peaks for the higher order eigenfreqiencies is a problem of the microphone not sufficiently picking up the amplitude at the higher frequencies, or that the resolution of the signal is simply not sufficient is not known but will be investigated in Chapter 5 and Chapter 6.

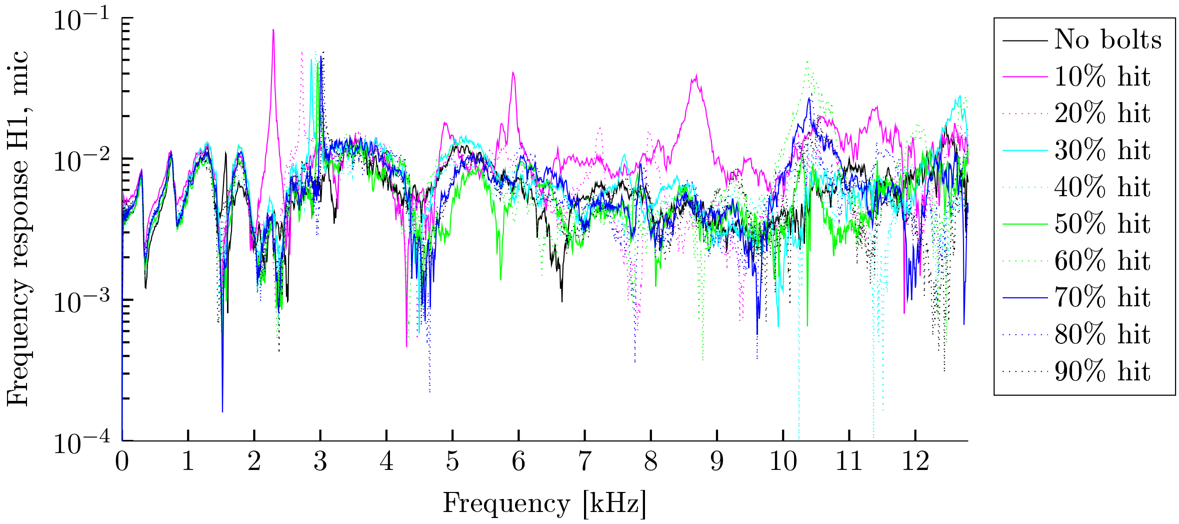

Figure 2.22 Response obtained with the microphone for the steel structure.

In Table 2.2 the resonances found with the different measurement equipment can be seen. As seen the measurements on the steel structure are very similar, with acc3 measurements showing slightly higher resonant frequencies. For the aluminum structure the measurements for pretension below 50% varies significantly but is steady for pretension above 50%. This difference in measurements for the aluminum structure at pretension below 50%, along with the steady increase of frequencies above this level indicates that only measurements for pretension above 50% should be trusted. This can be expanded to include the steel structure, stating that only measurements at above 30% pretension should be trusted.

Measurement	**10%**	**20%**	**30%**	**40%**	**50%**	**60%**	**70%**	**80%**	**90%**
Steel structure resonances(Hz)									
Microphone	2288	2720	2864	2928	2960	2984	3008	3032	3048
Accelerometer 2	2288	2720	2864	2928	2960	2984	3008	3024	3040
Accelerometer 3	2288	2800	2864	2968	2992	3008	3016	3040	3048
Aluminum structure resonances(Hz)									
Microphone	3224	3416	3328	3464	3704	3816	3856	3896	3904
Accelerometer 2	3144	3432	3384	3480	3704	3816	3856	3896	3896
Accelerometer 3	3440	3744	3672	3768	3704	3816	3856	4128	4128

Table 2.2 Resonances found with the different equipment.

As it can be seen, there is a difference in the resonant frequencies obtained with acc2 and acc3, which is unexpected, as they are placed orthogonally and the structure is symmetric. Due to the symmetry of the structure, it is expected to have two modes with identical shape and resonant frequency, but angled 90 deg to each other. Imperfections in the structure materials and setup, could though affect these so that they are not longer identical, but only very close, which is thought to be the cause of this difference between acc2 and acc3. It should be noted that, the microphone is positioned so that it faces in the same direction towards the structure as acc2, and so it makes sense that it measures the same resonances as acc2. Positioning the microphone in the same direction as acc3, will likely produce microphone readings with resonances similar to those obtained with acc3.

What can be seen from the results is that there is a trend of the resonant frequencies to increase around 200Hz. A change in the frequency response would be expected with increased tension, as a result of increased stiffness, however the required increase in stiffness is too large to be feasible, which is explained more in depth in Chapter 3. Another explanation for the increase in resonant frequencies could be a change of the boundary conditions at the interface between the structure and the bolt. This hypothesis will be explored more thoroughly in Chapter 3.

2.3 Damping determination

Besides determining the resonant frequencies, it is also investigated whether the damping in the structure is influenced by the change in pretension. The reason for investigating the damping, is that the sound emitted by the structure seems to change from a flat to a more ringing sound, which could be caused by a change in damping.

To determine the damping of the structure the half power bandwidth method is used. With this method the damping can be calculated from the peaks and peak widths (bandwidth) in the FRF, for lightly damped structures $\zeta < 5\%$ [Rao, 2011]. While this method is not the most precise and is highly dependent on the resolution of the FFT, it can give a fast indication of the damping in the system. This is also the method used in Pulse to determine the damping in the FRF. Going into Pulse to extract each damping would take a lot of time, so instead the exported FRF data is used in a MATLAB program that automatically calculates the damping for each peak. The MATLAB script can be found on the Appendix CD[2].

2.3.1 Automating the half power bandwidth method

As stated, the half power bandwidth method can be used to find damping from FRF's. The idea is to take the amplitude at the resonant frequency, called the quality factor Q_r, and find the amplitude where the power of the signal is halved, as given by Equation (2.1).

$$Q_{hp} = \frac{Q_r}{\sqrt{2}} \tag{2.1}$$

where:

Q_r	Quality factor at resonance, [-]
Q_{hp}	Half power of the quality factor at resonance, [-]

From the value of Q_{hp} the frequencies, having this amplitude, ω_{R1} and ω_{R2}, located on either side of the peak can be found. From these points the damping ratio can be determined using Equation (2.2) .

$$\frac{1}{2\zeta} = \frac{\omega_r}{\omega_{R2} - \omega_{R1}} \tag{2.2}$$

where: [Rao, 2011]

ζ	Damping ratio, [-]
ω_r	Resonant frequency, $\left[\frac{rad}{s}\right]$
ω_{R1}	First half power point, [Hz]
ω_{R2}	Second half power point, [Hz]

To automatically calculate the damping from the results obtained, the points of the exported FRF are imported into MATLAB. The resonant frequency is then found by finding the maximum amplitude in a

---

[2] Appendix CD\MATLAB\Experimental postprocessing\FRF_main

given interval, 0 to 5000Hz for the first frequencies, from the amplitude at resonance, Q_{hp} is calculated. To be able to calculate the damping, the values of ω_{R1} and ω_{R2} needs to be determined. As the obtained FRF is a series of points it is unlikely that ω_{R1} and ω_{R2} corresponds to these points, so it is necessary to calculate their values from the surrounding points.

As shown on Figure 2.23 the value of Q_{hp}, marked by the red line, can lie between measurement points, marked by black dots. To find the point ω_{R2} where the FRF has the value of Q_{hp}, marked by a blue dot, the point before and after is located. As seen in Figure 2.23 two triangles can be obtained from the three points, sharing the same angle α, and thus the following equations can be written.

$$tan(\alpha) = \frac{\omega_{R2} - \omega_{i-1}}{Q_{hp} - A_{i-1}} \qquad tan(\alpha) = \frac{\omega_{i-1} - \omega_i}{A_{i-1} - A_i} \tag{2.3}$$

$$\omega_{R2} = \frac{\omega_{i-1} - \omega_i \cdot Q_{hp} - A_{i-1}}{A_{i-1} - A_i} + \omega_{i-1} \tag{2.4}$$

where:

ω_i	Frequency at point i, $[\frac{rad}{s}]$
A_i	Amplitude at point i, [-]

As both the frequencies and amplitudes at the points are readily available, from the FRF data, ω_{R2} can be calculated from Equation (2.4). The process is then repeated to find ω_{R1}.

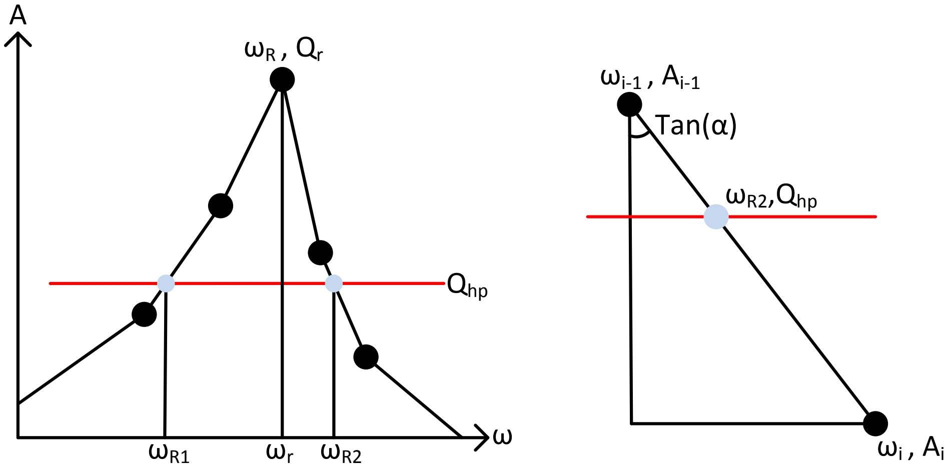

Figure 2.23 Illustration of the geometric principle used to determine the values of ω_{R1} and ω_{R2}

When both ω_{R1} and ω_{R2} have been obtained, the damping ratio can be calculated from Equation (2.2).

2.3.2 Results

In Table 2.3 the damping ratios obtained with the presented procedure can be seen. If the results for pretension below 20% and 50% for steel and aluminum respectively are excluded, it is seen that the damping ratio remains stable for the steel structure while there is a decrease for the aluminum structure. From the results obtained in this chapter it seems unlikely that the damping change, in relation to pretension, causes a audible difference in the acoustical response above the thresholds of 20% and 50%. However if the damping ratios for the aluminum structure are observed over the entire range of 10% to 90% it is very likely that the change in damping can cause the difference in the ringing sound initially observed.

Measurement	**10%**	**20%**	**30%**	**40%**	**50%**	**60%**	**70%**	**80%**	**90%**
Steel structure damping(%)									
Microphone	0.57	0.43	0.38	0.37	0.35	0.33	0.35	0.38	0.35
Accelerometer 2	0.56	0.46	0.39	0.37	0.37	0.35	0.35	0.38	0.37
Accelerometer 3	0.56	0.47	0.46	0.41	0.38	0.53	0.40	0.34	0.32
Aluminum structure damping(%)									
Microphone	4.39	1.28	7.44	1.46	0.74	0.51	0.46	0.47	0.38
Accelerometer 2	5.65	1.11	2.07	1.01	0.71	0.52	0.49	0.49	0.39
Accelerometer 3	1.04	0.62	0.69	0.68	0.67	0.50	0.46	0.40	0.41

Table 2.3 Calculated dampening from experimental data.

2.4 Washer influence

To determine if the size of the washers has an influence on the structural response, experiments have been performed for both the steel and aluminum structure, for three sizes of washers, which can be seen in Figure 2.24. The size of the middle sized washer is based on the size of a standard M12 washer, the small and large size are 50% smaller and larger, in outer diameter respectively. Working drawings for the washers can be found in Appendix B.

Figure 2.24 The different washer sizes tested.

Figure 2.25 Indents and abrasions caused by bolt tightening

The tests did however not show any clear differences on the response when changing the washers. By inspecting the different washers after the testing, it was observed that the area of contact between the bolts and the washers were approximately the same for all three sizes, as indicated by the indented and abraded areas shown on Figure 2.25. This indicates that there is little change in the interface between the bolt and the structure, for different washer sizes. Thus the influence of washer sizes will not be investigated further.

2.5 Investigating higher order resonances

As can be seen from Figure 2.19 and Figure 2.20 there is a second group of peaks at around 10kHz and 8kHz for steel and aluminum respectively. The exact values of these peaks can be seen in Table 2.4.

Measurement	**10%**	**20%**	**30%**	**40%**	**50%**	**60%**	**70%**	**80%**	**90%**
Acc2 steel	8672	7668	9824	10200	10312	10368	10408	10424	10432
Acc2 aluminum	7504	8208	8424	8496	8536	8576	8600	8608	8616

Table 2.4 Location of the first resonance peak for a given level of pretension, from acc2 measurements

As seen from the table, the same behavior can be observed as in the first frequencies, with higher frequencies at higher tension. Looking over the entire range of pretension, the eigenfrequency gap between 10% and 90% is increased compared to the results for the lower order modes. Looking at only the range from 20% and 50% and up, for steel and aluminum respectively, the gap is increased for steel and decreased for the aluminum. The reason for the decrease in resonant frequency from 10% to 20% pretension is not clear, but supports the statement that only measurements from 30% pretension and up should be accepted for the steel stucture, as stated in Section 2.2.

2.6 Summary

Summing up on what has been found during the initial work, it was found that a clear shift in the eigenfrequencies, increasing with higher levels of pretension. This increase in frequencies is so significant that it can not be explained purely by a change in stiffness, and is thought to be caused by a change in the boundary conditions instead. It was also found that the microphone could only pick up the first set of natural frequencies, due to the duration of the signal generated by the impact hammer. The influence of the washers was also examined and was found to be negligible, and so will not be treated further.

In relation to the damping of the structure, it was found that there is a clear difference between a tightened and an untightened bolt, which could be the reason for the audible difference in the "ringing" of the structural response, with damping decreasing with increased pretension. A difference in the damping of bolts tightened above 20% and 50%, for steel and aluminum respectively, can however not be seen clearly, although the tendency for decreasing damping is present.

The information obtained in this chapter will be used as the foundation for the further work, where the transmission mechanism between the bolt and the cylinder will be examined in Chapter 6. The hypothesis of the boundary conditions being the cause of the main part of the rise in eigenfrequencies is treated in Chapter 3. Furthermore, as the results obtained with the steel structure are more consistent, with regards to both the resonance response and damping, than the aluminum structure, the steel structure will be the basis of the further work of the project.

3 Investigation of response change

In Chapter 2 it was found that when a bolt is tensioned, the eigenfrequencies related to the bolt increase with increased tension. The purpose of this chapter is to examine the cause of this change, which is initiated by simple calculations followed by Finite Element (FE) modelling.

In the experiments described in Chapter 2 the frequencies were found to vary from 2864Hz to 3040Hz, for pretensions of 30% and 90% respectively, measured by acc2 on the steel structure. This gives a difference of 176Hz, thus the frequency increases by 6.1% when the bolt is tightened. The cause of the difference in the excited frequencies is yet to be explained.

To explain the increase in the measured frequencies, it is necessary to consider the system of the test setup. As the bolt is what vibrates, it is only the bolt that is simplified. The bolt is linear elastic, thus it is reasonable to simplify the bolt to a linear system. By evaluating each mode of the bolt separately, it is possible to model each mode by a one degree of freedom system. Each mode of the bolt can then be represented by equivalent spring constants and a fixed mass. The single degree of freedom system is shown on Figure 3.1. The system in Figure 3.1 is only used for illustrating the test setup, and to find the root cause of the increase in excited frequencies.

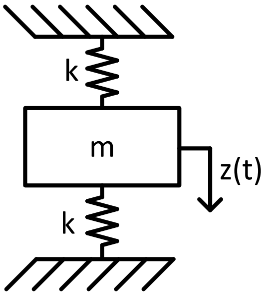

Figure 3.1 The spring/mass system used for illustrating the system.

The eigenfrequency of a spring/mass system is found by Equation (3.1). As the eigenfrequencies are already known, and the mass does not change at any point, the equation can be used for finding the change in stiffness of the system.

$$\omega_n = \sqrt{\frac{k_{eq}}{m}} \tag{3.1}$$

where:

k_{eq}	Equavalent stiffness, $\left[\frac{N}{m}\right]$
m	Mass, [kg]
ω_n	Undamped Eigenfrequency, $\left[\frac{rad}{s}\right]$

To find the change in stiffness Equation (3.1) is utilized in Equation (3.2).

$$\frac{3040Hz}{2864Hz} = 1.061 = \frac{\sqrt{\frac{k_{eq1}}{m}}}{\sqrt{\frac{k_{eq2}}{m}}} = \sqrt{\frac{k_{eq1}}{k_{eq2}}} \tag{3.2}$$

$$\frac{k_{eq1}}{k_{eq2}} = 1.127 \tag{3.3}$$

The result from Equation (3.3) shows that a change in stiffness of 12.7% is required in order to change the frequencies sufficiently. This is unlikely for a steel bolt, as it is pretensioned according to its proof strength and thus is loaded in the linear elastic zone. It is therefore concluded that a stiffness change of the bolt is not the primary cause of the frequencies.

As briefly discussed in Section 2.2, another hypothesis is that the change could be induced by the change of boundary conditions when the bolt is tightened. The bolt is expected to move more freely when the bolt is less tightened and the bolt is more fixated when it is tightened more. To investigate if the change of boundaries can yield a difference of 6.1% in frequencies a Finite Element (FE) model is created. The boundary conditions in the FE model is changed between hinged and clamped. The model, boundary conditions and mesh is discussed in the following section.

3.1 FE model establishment

During this section the FE model, that is used to investigate the effect of boundary conditions, is created. The model is based on the M12 bolt used in the test rig and there is no pretension applied to the bolt as the pretension is simulated by the change of boundary conditions. The geometry for the FE model based on standard dimensions for a M12 bolt. The finished model is seen on Figure 3.2.

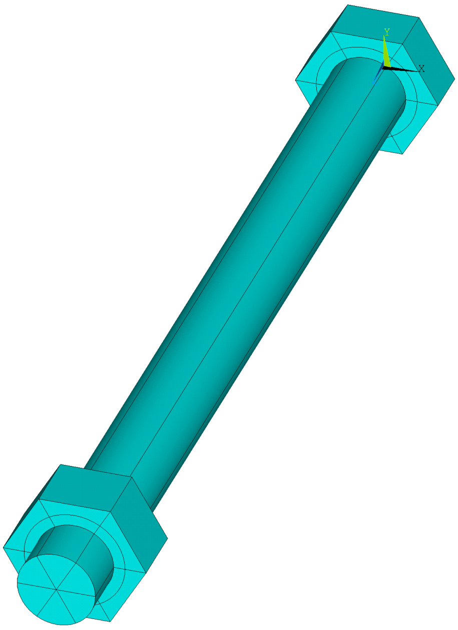

Figure 3.2 The model of the bolt used to find the eigenfrequency.

On Figure 3.2 it is seen that the bolt head and nut is divided into 12 seperate volumes, because the circle separating the volumes is used for boundary conditions as explained in Section 3.1.2.

3.1.1 Meshing the model

The mesh is created as a mapped mesh with SOLID186 elements in ANSYS Classic. SOLID186 elements are a second order quadrilateral element. The quadrilateral element shape is chosen because it allows a much smoother mesh than with tetrahedral elements. The converged mesh with an element size of 1.75mm is seen on Figure 3.3, the mesh convergence study is described in Section 3.1.3.

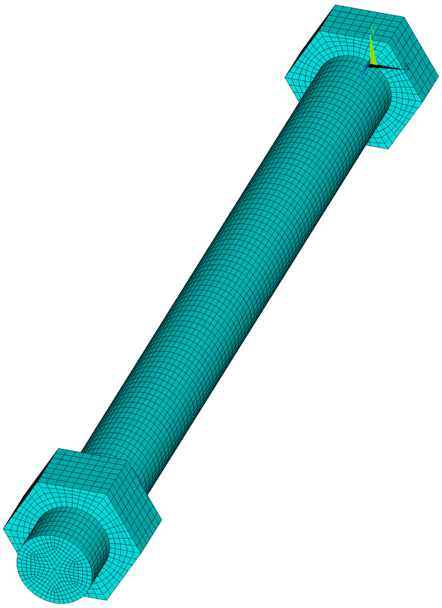

Figure 3.3 The mesh used on the bolt vibration study.

The SOLID186 element used can be configured according to the analysis carried out. During this analysis of the eigenfrequencies of the bolt the configurations used are stated in Table 3.1.

SOLID186 element options	
Element technology	Full integration
Layer construction	Structural solid
Element formulation	Pure displacement

Table 3.1 Element configuration used for the bolt frequency analysis.

The full integration option is selected as this option uses more Gauss points when integrating and thus a higher accuracy is obtained but the calculation time is slower compared to the reduced integration option. The pure displacement option is selected as frequency and modes.

3.1.2 Boundary conditions

Two different boundary conditions are applied to the model, where the first boundary condition is hinged, as seen on Figure 3.4. The boundary condition is applied to a circle of nodes placed between the hex head and bolt shaft, the circle used for the hinged boundary is seen on Figure 3.2. The fixed boundary condition is a total fixation of the bolt head and nut as shown on Figure 3.5. Both boundary conditions are applied to the bolt head and the nut on the surfaces pointing towards each other.

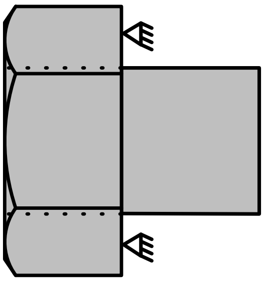

Figure 3.4 Hinged boundary condition for the bolt FE model.

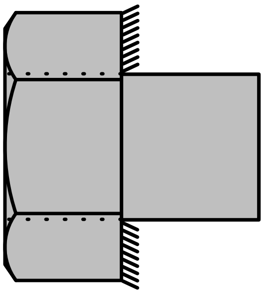

Figure 3.5 Fixed boundary condition for the bolt FE model.

The boundary conditions is applied directly to nodal points in the model by selecting the appropriate areas or lines and afterwards selecting nodes attached to the selected areas or lines.

3.1.3 convergency study

To ensure the accuracy of the FE model, it is necessary to make a mesh convergence study. The convergence study is only shown here for the fixed boundary condition, as it tends to converge slower than the hinged boundary condition. When the eigenfrequency is changing less than ±0.25% the model is considered as converged. The mesh is refined from 10mm to a mesh size of 1.25mm with a step size of 0.25mm. The mesh is not refined more than a mesh size of 1.25mm due to computational limitations. The scripts for the performing the convergence study is found on the Appendix CD [1].

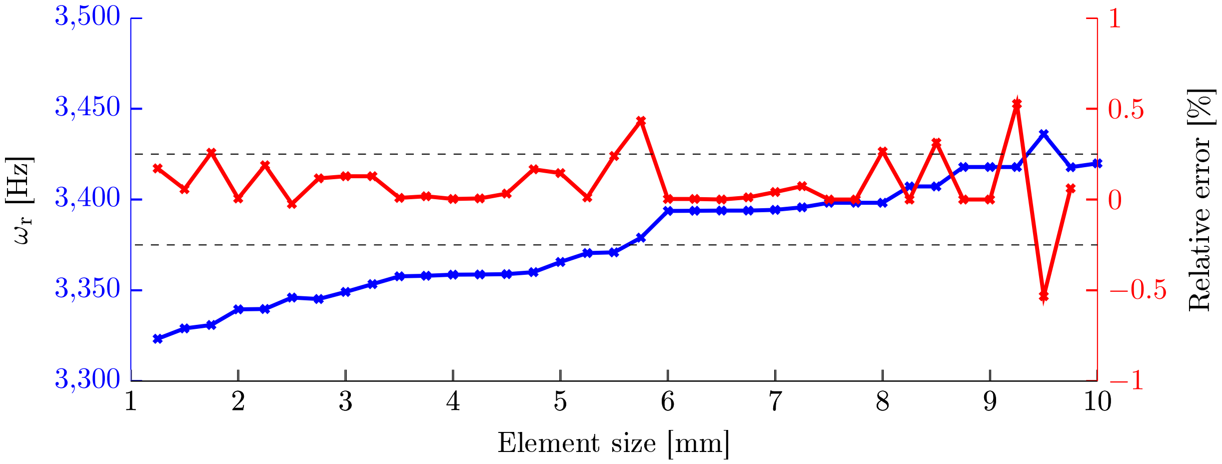

Figure 3.6 Convergence study of the FE bolt model.

As seen on the Figure 3.6 the mesh seems to converge when the relative error is considered. However the frequency seems to decrease steadily and the model do not seem to be converging towards a steady value. Thus a more thorough study of the model is carried out. The new study is initiated by considering a clamped-clamped cylinder, that represents the bolt shaft. The detailed analysis is set up to see if the simplified structure converges. The same mesh tool, solver and MATLAB script from the convergence of the bolt study is used for the cylinder. The meshed cylinder is shown in Figure 3.7.

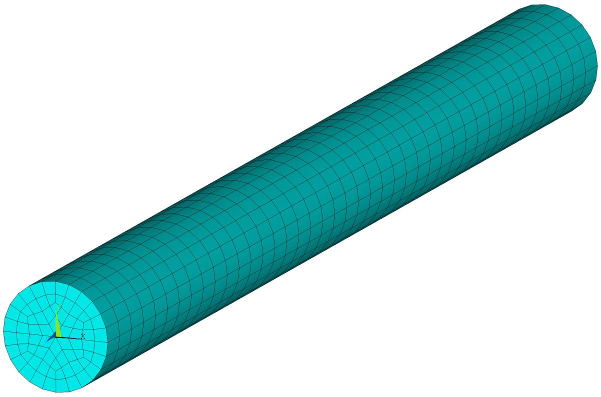

Figure 3.7 The meshed model of the cylinder with a mesh size of 3mm.

The result of the convergence study of the cylinder is seen in Figure 3.8.

---

[1] Appendix CD \FE \Scripts \Convergence bolt

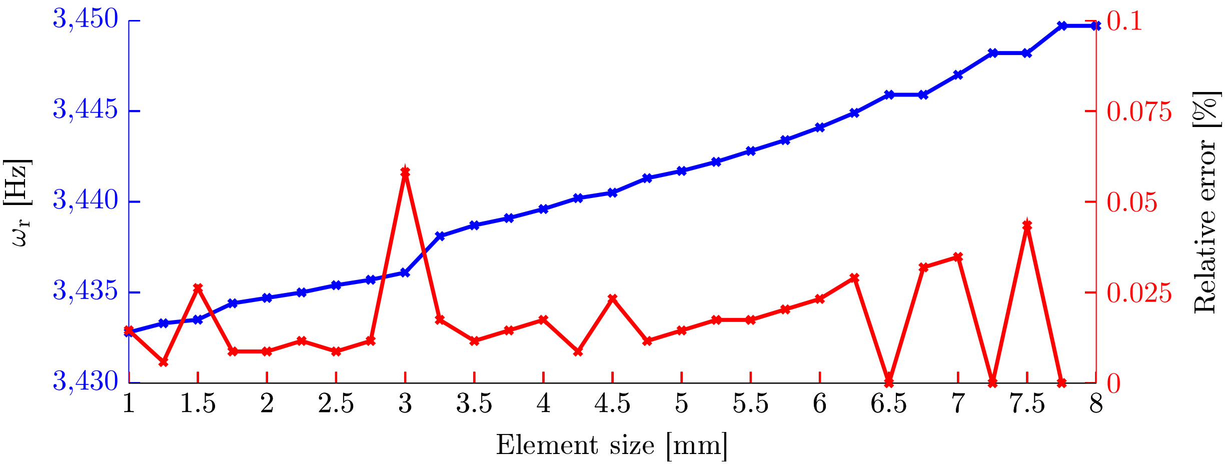

Figure 3.8 Convergence study of the FE bolt model.

From the convergence study in Figure 3.8, it is seen that the cylinder, that is clamped in each end, converges and the last six mesh sizes is within 2Hz. Thus it is concluded that it is not the bolt shaft that prevents the bolt model from converging. The mode shape of the cylinder is seen on the animation attached on the Appendix CD [2]. The scripts for the convergence study of the cylinder can be found Appendix CD[3].

A detailed model of the bolt head is then made, to investigate if it is the bolt head that does not converge. The bolt head is constrained in the same way as the full bolt model but the bolt shaft, nut etc. are neglected. The bolt head model is seen on Figure 3.9.

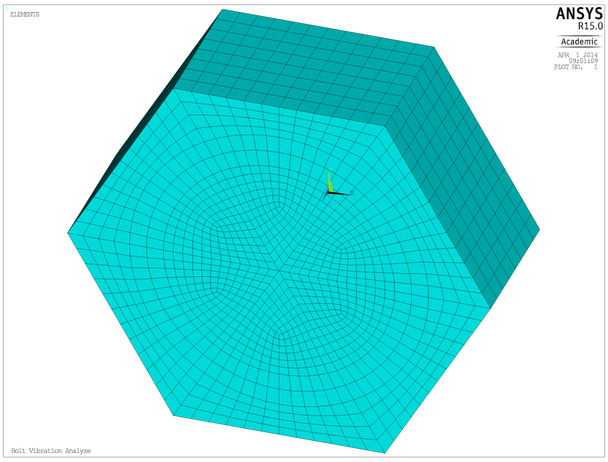

Figure 3.9 The meshed model of the bolt head with a mesh size of 1mm.

The convergence study of the bolt head is seen on Figure 3.10, and it is seen that the bolt head also converges near a frequency of 83880Hz and the relative error is for the last four mesh sizes less than 0.05%. The mesh size of the head is required to be much finer in the bolt head before the model converges than the bolt shaft. The mode shape is seen on the animation attached on the Appendix CD [4]. The scripts for the convergence study of the bolt head can be found Appendix CD[5].

Since both submodels converge, it is expected that the full bolt model also converges, but is limited by the available computational power. Hence a mesh size of 1.75mm for the full model is used.

---

[2] Appendix CD \FE \Animations \Cylinder Vibration Analysis.avi

[3] Appendix CD \FE \Scripts \Cylinder

[4] Appendix CD \FE \Animations \Bolt Head Vibration Analysis.avi

[5] Appendix CD \FE \Scripts \Bolt Head

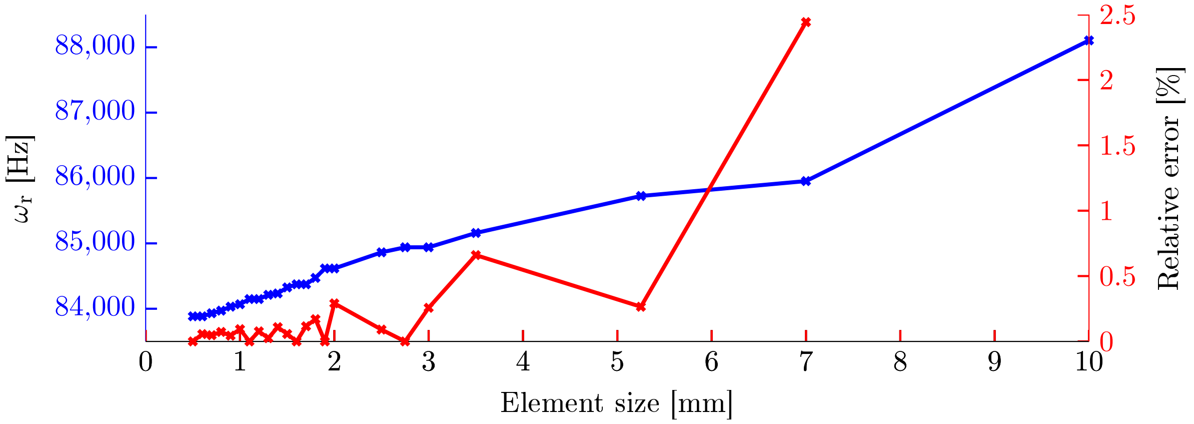

Figure 3.10 Convergence study of the FE bolt model.

3.2 FE results

In this section the FE model, is used to evaluate the eigenfrequency of the bolt for both the hinged and clamped boundary condition. The results of the the structural vibration study for the two different boundary conditions are listed in Table 3.2. The modes of the two boundary conditions is attached as an animation on the Appendix CD both for hinged BC[6] and clamped BC[7]. The scripts for the FE model, that can variate between the two boundary conditions, can be found Appendix CD[8].

	Hinged	Clamped
f_1 [Hz]	3141.3(Transeverse)	3345.5(Transeverse)
f_2 [Hz]	3141.3(Transeverse)	3345.5(Transeverse)
f_3 [Hz]	8284.8(Transeverse)	8790(Transeverse)
f_4 [Hz]	8284.8(Transeverse)	8790(Transeverse)
f_5 [Hz]	12474(Breathing)	12725(Breathing)

Table 3.2 Eigenfrequencies found by the FE model of the bolt.

The first two modal frequencies in Table 3.2 is at the same frequnecy and display the same first transverse mode of the bolt. The two frequencies indicate that the bolt can exhibit resonance for excitation in two different directions. From Table 3.2 it is also seen that there is a difference of 204.2Hz between the first eigenfrequencis of the two boundary conditions. The difference between the two boundary conditions is found to be 6.5%. Which is similar to the difference of 176Hz found during tests with a difference of 6.1%. So the change in boundary conditions is believed to be the root cause of the jump in frequencies.

3.3 Boundary condition sensitivity study

During this chapter the hinged boundary condition is assumed to be placed in the center between the bolt shaft and edge of the hexagonal bolt head, which implies a diameter of 15.4mm. This section will investigate if the location of hinged boundary condition will affect the response of the bolt by variating the location of the hinged boundary condition. It is important to evaluate the influence of the location of the hinged boundary condition, as this is an approximation to the actual behavior of the system.

The boundary condition diameter is tested for ±0.5mm and ±1mm in order to estimate the validity of the obtained results in Section 3.2. The results from variation of the BC diameter is stated in Table 3.3.

---

[6] Appendix CD \FE \Animations \Bolt Vibration Analysis BC1
[7] Appendix CD \FE \Animations \Bolt Vibration Analysis BC2
[8] Appendix CD \FE \Scripts \BC Bolt

	14.4mm	**14.9mm**	**15.4mm**	**15.9mm**	**16.4mm**
f_1 [Hz]	3142.7	3136.9	3132.2	3120.8	3116.2
f_2 [Hz]	3142.7	3136.9	3132.2	3120.8	3116.2
f_3 [Hz]	8293.3	8276.1	8261.7	8233.8	8219.5
f_4 [Hz]	8293.3	8276.1	8261.7	8233.8	8219.5
f_5 [Hz]	12471	12466	12464	12460	12458

Table 3.3 Eigenfrequencies found changing the diameter of the hinged BC.

As seen from Table 3.3 the variation for the first mode is 26.5Hz, which is less than 1% and the same applies for the second mode where results variate 73.8Hz which is also less than 1%. Thus the influence of the location of the BC diameter is not considered as very important if it is located in the examined region.

The scripts for the FE model, that can variate between the different radius', can be found Appendix CD[9].

3.4 summary

In this chapter, the hypothesis that changes in boundary conditions, cause the increase in resonant frequencies, seen in chapter 2, has been examined. Initially the required increase in bolt stiffness, to cause the resonant peak movement, has been calculated. This was found to be unfeasible as it required an increase in stiffness of 12.7% . Subsequently a FE model was established, and used to examine if changing boundary conditions could be the cause of the peak movement.

The results from test and FE is seen in Table 3.4 and Table 3.5 for the hinged and clamped boundary conditions respectively. From the tables it is seen that the FE results and test results are not exactly the same, but what is worth noticing is that the frequencies is in the same region and the difference between the 30% pretentions and the 90% pretension from tests and the difference of the FE results is almost the same.

	FE Hinged	**Test 30%**
f_1 [Hz]	3141	2864
f_3 [Hz]	8285	9824

Table 3.4 Eigenfrequencies found by the FE model and test results of the bolt.

	FE Clamped	**Test 90%**
f_1 [Hz]	3346	3040
f_3 [Hz]	8790	10432

Table 3.5 Eigenfrequencies found by the FE model and test results of the bolt.

The difference between FE and tests is elaborated more in Chapter 3. The difference between results for both FE and tests is stated in Table 3.6.

	FE	**Test**
Δf_1 [Hz]	204	176
Δf_3 [Hz]	505	608

Table 3.6 Difference in the eigenfrequencies found by the FE model and test results of the bolt.

Based on these results, it is believed that the change in boundary conditions, is the main cause of the change in response for changing pretension. In order to investigate this hypothesis more thoroughly, more tests on different bolt sizes are carried out and more detailed modeling is performed.

---

[9] Appendix CD \FE \Scripts \Hinged Study

Further experimental investigation

4

The purpose of this chapter is to investigate the results from Chapter 2 and 3 in greater detail. In those chapters, the feature that causes the change in response under pretension, was determined to be the change in boundary conditions for the bolt. In this chapter the robustness of this feature is examined by testing different sizes of bolts to see whether the phenomenon is consistent in its behavior.

In Chapter 2 and 3 the mechanism causing the change in response was identified as a change in boundary conditions. This change will occur when increased tension in the bolt causes the surfaces of the bolt head, washer and structure to be pressed harder together, thus restricting the motion of the bolt head. The purpose of this section is to examine this phenomenon for different sizes of bolts. The bolts examined in this section are M18 and M24 bolts, the setup used is identical to the one described in Section 2.1, except for the structure itself where the hole for the bolt need to be made to fit the larger bolts. Working drawings for the test structure for M18 and M24 bolts can be found in Appendix B.

4.1 Parametric study of bolts

To get an idea of what to expect from the response of the structures, the first five natural frequencies for the bolts have been calculated using a FEM model similar to the one described in Chapter 3. The results of the FEM analysis can be seen in Table 4.1 and 4.2, the values under hinged are what is expected to be the lower bound of the frequencies corresponding to a loose bolt, while the values under clamped are the upper bound of the frequencies and is what is expected for a highly pretensioned bolt. It should be noted that the frequencies of the FE model is not expected to correlate completely with the experimentally found values, as the geometry and material parameters are idealized, but will be used as an indication of where to expect resonant frequencies as well as how large a gap to be expected between a loose and a completely tightened bolt.

	Hinged	**Clamped**
f_1 [Hz]	4373.2(Transverse)	4767.7(Transverse)
f_2 [Hz]	4373.2(Transverse)	4767.7(Transverse)
f_3 [Hz]	11061(Transverse)	11958(Transverse)
f_4 [Hz]	11061(Transverse)	11958(Transverse)
f_5 [Hz]	12253(Breathing)	12625(Breathing)

Table 4.1 Eigenfrequencies found by the FE model for the M18 bolt.

	Hinged	**Clamped**
f_1 [Hz]	5310.1(Transverse)	5913.1(Transverse)
f_2 [Hz]	5310.1(Transverse)	5913.1(Transverse)
f_3 [Hz]	12021(Breathing)	12522(Breathing)
f_4 [Hz]	12843(Transverse)	14151(Transverse)
f_5 [Hz]	12843(Transverse)	14151(Transverse)

Table 4.2 Eigenfrequencies found by the FE model for the M24 bolt.

On Figure 4.1 and 4.2 the response obtained with acc2 can be seen for the M18 and M24 systems respectively. For the response of the M18 system three peaks are observable, although at somewhat lower frequencies than expected, and showing a movement of the peaks with changed pretension as expected. However when looking at the peak at approximately 4kHz, it can be seen that when the pretension is increased to 90% the peak disappears. Looking at Figure 4.2 it can be seen that the resonances expected at around 6kHz are not captured by the accelerometer and that the response of the system simply follows that of the structure surrounding the bolt. The reason for this cannot be readily explained, but an explanation might be that the compressive force exerted by the bolt will cause the bolt and structure to move as one and not two joined systems. A way to get more insight into the mechanics of the system, could be an expanded FE model that models the entire system. This expanded model will be treated in detail in Chapter 5.

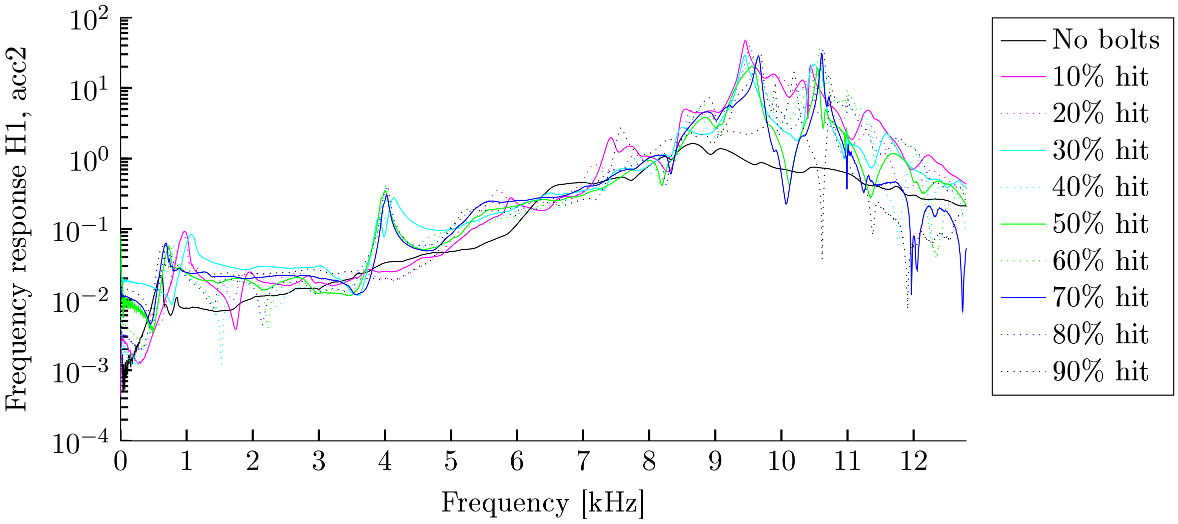

Figure 4.1 Frequency response H1, obtained with acc2, for M18 bolt.

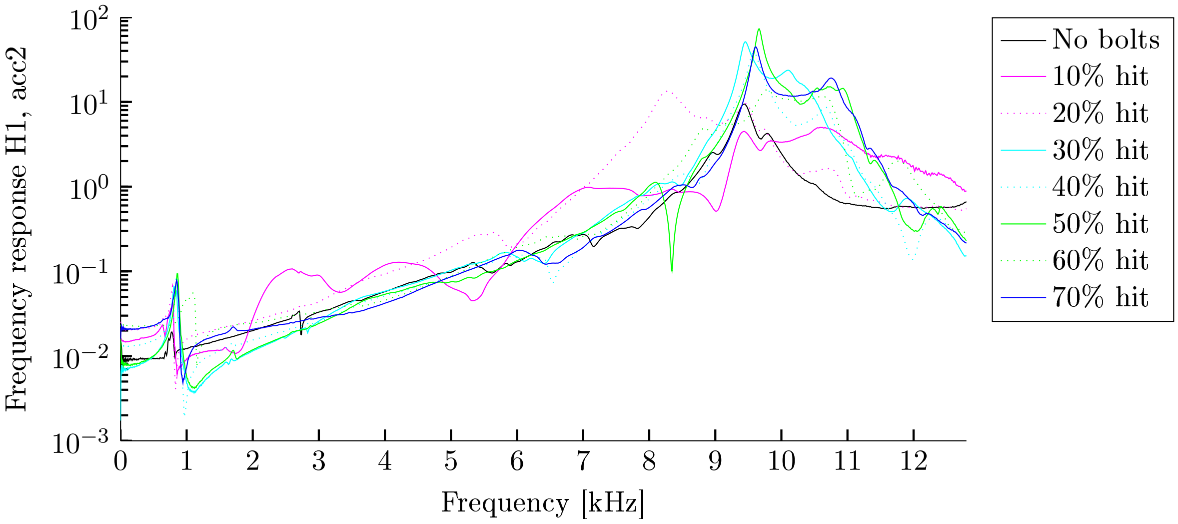

Figure 4.2 Frequency response H1, obtained with acc2, for M24 bolt.

In Figure 4.3 and 4.4 the response obtained with the microphone for the two bolt sizes can be seen. Here only the higher order modes are captured, this is expected for the structure with the M24 bolt as the accelerometers do not capture the resonances expected at 6kHz. For the M18 bolt however, some indication of the resonances would be expected. To check if the response can be obtained with the microphone, an alternate method is used to visualize the response. In Figure 4.5 a plot of the Short Time Fourier Transform (STFT) for the M18 response to a single hit under 80% pretension. As it can be seen, the peak at 4kHz is visible due to the slower decay of the frequency response.

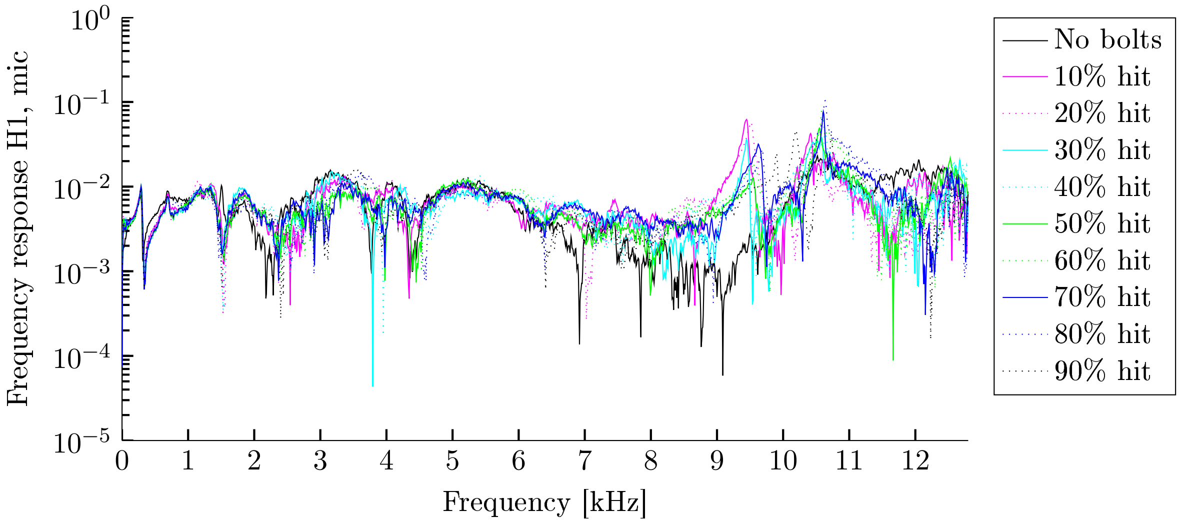

Figure 4.3 Frequency response H1, obtained with mic, for M18 bolt.

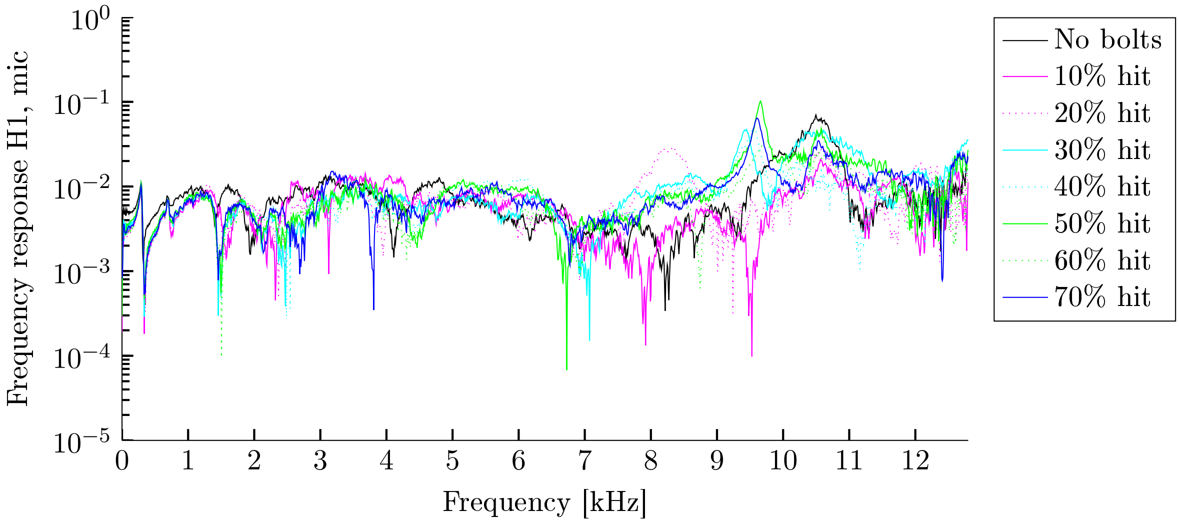

Figure 4.4 Frequency response H1, obtained with mic, for M24 bolt.

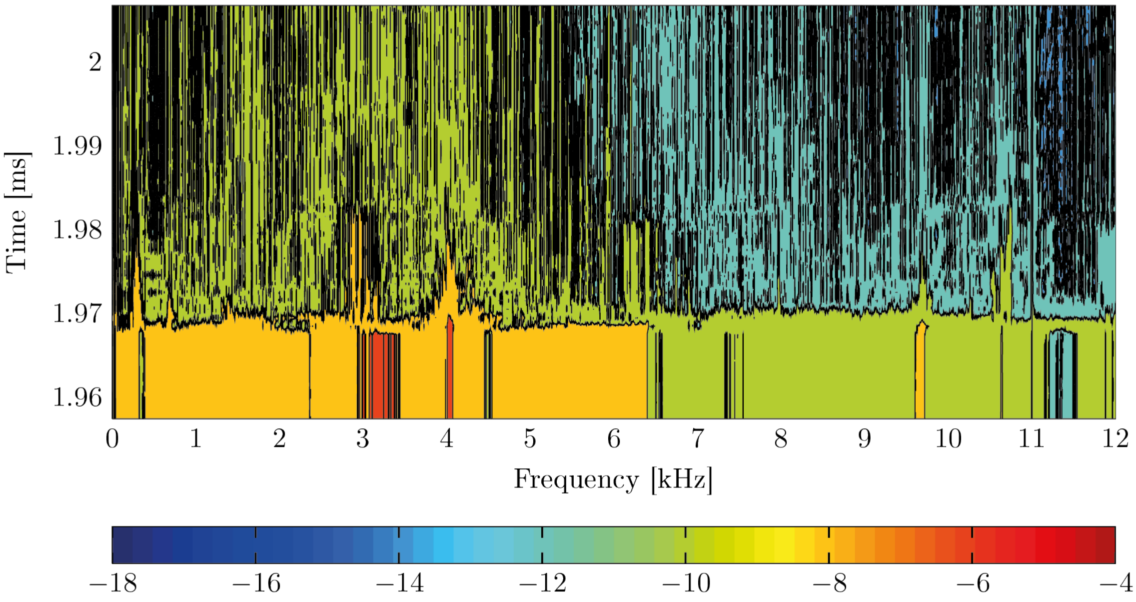

Figure 4.5 STFT for the response obtained with the microphone at 80% pretension for the M18 bolt.

Thus it is possible to obtain the resonant frequencies using the microphone, even if these are not immediately obtainable using FRF's. Furthermore the acc2 measurements for the M24 bolts were investigated via STFT's to determine if the resonances expected at around 6kHz can be seen with this method, however no additional information was obtained from this.

4.2 Results comparison

In this section the results from the M18 and M24 structure tests are compared to those obtained for the M12 structure, as well as the expected resonance peak locations, obtained with the FE model. The location of the peaks found for each bolt size and mode, can be seen in Table 4.3. The approximate location where peaks would be expected, based on the FE analysis, can be seen in Table 4.4. In the tables, double resonances have been joined as one, so that only three modes are evaluated.

Measurement		**10%**	**20%**	**30%**	**40%**	**50%**	**60%**	**70%**	**80%**	**90%**
M12	f_1 [Hz]	2288	2720	2864	2928	2960	2984	3008	3024	3040
	f_2 [Hz]	8672	7668	9824	10200	10312	10368	10408	10424	10432
M18	f_1 [Hz]	-	-	3912	3944	4000	4008	4024	4032	-
	f_2 [Hz]	9456	9528	9448	9480	9552	9592	9656	9680	9904
	f_3 [Hz]	10440	10440	10488	10504	10552	10584	10608	10632	10744
M24	f_1 [Hz]	9440	9472	9456	9584	9664	9776	9608	N/A	N/A

Table 4.3 Peak locations for the tested bolt sizes.

Expected peak location			
	M12	**M18**	**M24**
f_1 [Hz]	3kHz	8-9kHz	12kHz
f_2 [Hz]	4-5kHz	11-12kHz	12kHz
f_3 [Hz]	5-6kHz	12kHz	13-14kHz

Table 4.4 Approximate peak location, expectation based on FE analysis of bolt.

As it can be seen from the tables, only in the experiments for the M18 bolt, three modes were found. These were however lower than predicted by the FE model of the bolt, suggesting that a more complex model might be needed to accurately predict the system behavior. Furthermore, the lower than expected resonant frequencies of the M18 system, implies that the response of the other systems could also be expected to be lower than predicted. This suggests that the second mode found for the M12 bolt could actually be related to the third mode instead, and that the second mode is simply not captured well by the accelerometer. Looking at the response for the M24 system, the same can be said for the resonance that is captured, which might be related to the second mode of the system, rather than the first. Whether this is the case, and why these modes are not captured by the accelerometer, will be treated in Chapter 5, where an expanded FE model of the system is treated.

Looking at the movement of the peaks, it can be seen that the same kind of movement observed for the M12 structure is seen for the M18 structure, where higher pretension causes a steady increase in eigenfrequencies. With somewhat similar magnitudes of change, if the second group of eigenfrequencies of the M12 structure is seen as the third group, as described above. The same cannot be seen for the M24 structure, as the resonance for 70% pretension drops down in frequencies, except for this the behavior is the same however.

4.3 Summary

In this chapter the behavior of a system containing a M18 bolt and a system containing a M24 bolt, have been examined. For these tests, the same behavior as previously seen, where the resonant frequencies increase with higher levels of pretension, was observed. It was also found that above a certain threshold of clamping force, some of the expected resonance peaks disappeared, the reason for this is not known but an explanation will be sought in Chapter 5. Furthermore, it was found that even if the response of a certain mode could not be seen in an FRF, it might be possible to obtain it by displaying the response with an STFT.

Expanded finite element model

5

Based on the work described in Chapter 2 and 3 it was established that increasing the pretension of a M12 bolt, would cause an increase in the resonant frequencies observable in an FRF. In Chapter 4 larger sizes of bolts were examined, and it was found that the change of frequencies observed for the M12 structure were also present here. More importantly it was found that when the clamping force, caused by the pretension, reaches a certain threshold, the peaks associated with the first eigenfrequencies completely disappear, and only the response of the structure can be observed. The reason for this is unknown, and it is the purpose of this chapter to investigate this phenomenon.

To investigate the phenomenon a full FE model of the system is created. The first step in doing this is to establish a model for the structure, and determining its eigenfrequencies through a modal analysis. Once the model of the structure has been established, it is used together with the model for the bolt to create a model of the full system. A modal analysis is then performed on this full model to establish whether the model is valid when compared to the physical system. Finally a harmonic analysis is performed to investigate details of the system that would be difficult to examine in practical tests.

5.1 Structure model

To get started with the full system model, a model of the structure around the bolt is modeled to obtain the response of the structure itself, and to get an idea of the mesh quality required to get accurate results for the structure. This is done using the procedure described in Chapter 3, using the same element type and settings. The geometry and mesh for the M12 structure can be seen in Figure 5.1 and 5.2 respectively.

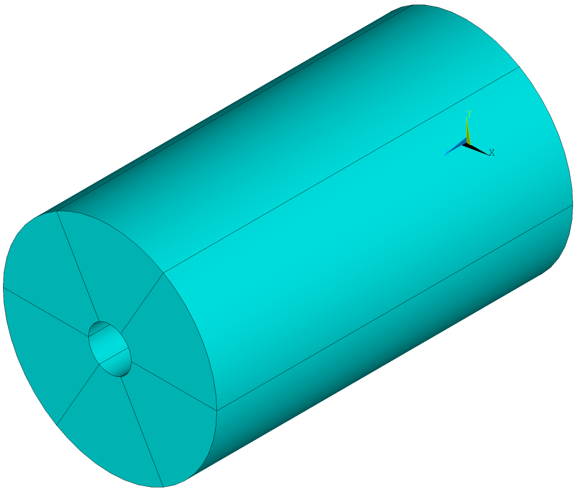

Figure 5.1 Geometry of the M12 structure.

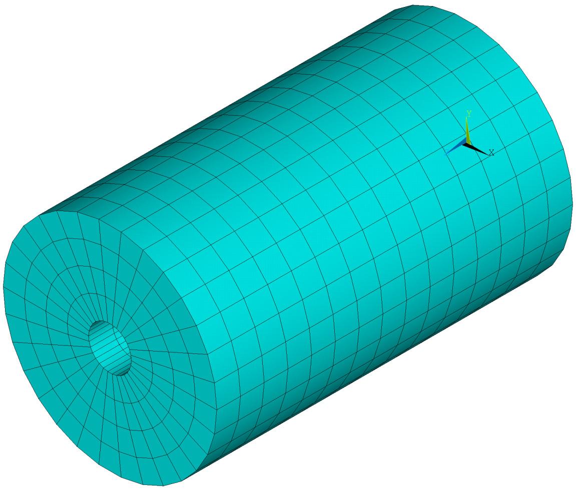

Figure 5.2 Meshed model of the M12 structure.

As the structure is suspended by four compliant strings, it is assumed that the structure can vibrate freely. Therefore the structure is modeled without any boundary conditions, this also means that the first six modes found for the structure is at 0Hz and is rigid body motions, and are thus excluded when the results are presented.

In Figure 5.3 the convergence of the first eigenfrequency for the M12 structure is seen. The model is completely converged at an element size of $7mm$, which is also the case for the M18 and M24 structures.

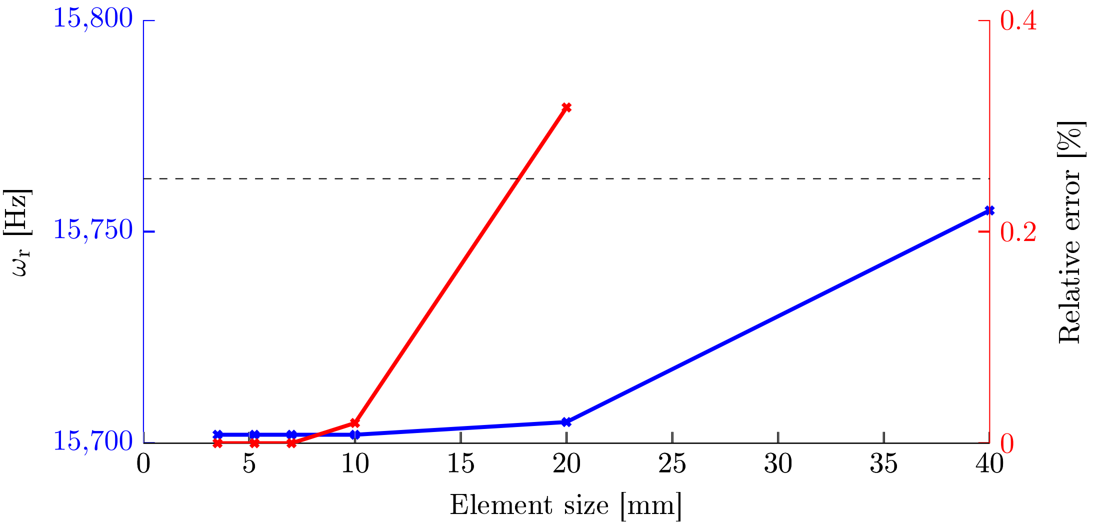

Figure 5.3 Convergence for the M12 structure

The results of the analysis for the three structures can be seen in Table 5.1. As it can be seen, the response of the structure gives much higher resonant frequencies, compared to those of the bolts found in Chapter 3 and 4.

	M12	**M18**	**M24**
f_1 [Hz]	15755(Torsional)	15747(Torsional)	15740(Torsional)
f_2 [Hz]	17095(Transverse)	17085(Transverse)	17063(Transverse)
f_3 [Hz]	17095(Transverse)	17085(Transverse)	17063(Transverse)
f_4 [Hz]	24711(Longitudinal)	24640(Longitudinal)	23362(Breathing)
f_5 [Hz]	27050(Transverse)	25633(Transverse)	23362(Breathing)

Table 5.1 Eigenfrequencies found by the FE model for the different structures.

The fact that the first modes are torsional was found to be suspicious, so to verify the results of the FE analysis, the eigenfrequencies are calculated analytically. This is possible as the structure in itself is simple enough to be covered by analytical solutions for beams.

The torsional eigenfrequency is calculated from Equation (5.1), giving the n^{th} eigenfrequency for a free-free rod. The parameters used for the calculation can be seen in Table 5.2.

$$\omega_1 = \frac{\pi}{L}\sqrt{\frac{G}{\rho}} \tag{5.1}$$

where: [Rao, 2011]

L	Length, [m]
ρ	Density, $[\frac{kg}{m^3}]$

Model test parameters	
G	$77GPa$
ρ	$7800\frac{kg}{m^3}$
L	$0.1m$

Table 5.2 Parameters for calculating torsional frequencies.

The first torsional eigenfrequency is thus:

$$\omega_1 = 98658\frac{rad}{s} \tag{5.2}$$

$$f_1 = 15702Hz \tag{5.3}$$

This supports the result for the torsional mode found by the FE model, but to assure that it is actually the first eigenfrequency, the lowest transverse eigenfrequency has also been calculated. This has been done using Timoshenko beam theory and the procedure can be seen in Section 6.6, where it is found that the first transverse eigenfrequency is 16818Hz, verifying the results obtained with the FE model. The scripts for the FE model of the structure are found on the Appendix CD[1].

5.2 Complete structure modal analysis

To determine the eigenfrequencies for the entire system, a modal analysis is performed. This is done to examine if it is possible to accurately model the entire system, and thus predict the eigenfrequencies for a given system. Furthermore it is done to examine whether the expected peaks at around 6kHz for the M24 should be present in the experimental results.

As both models for the bolt and the surrounding structure have been created, making the full model is a question of piecing the two models together and adding details like the washer and transducer. The washer and transducer is modeled using the dimensions given in the working drawings in Appendix B. All components are then connected in the model, by gluing surfaces together, assuring that nodes at the glued surfaces are connected. The glue procedure is where the difference in the hinged and clamped model is implemented. In the clamped model, all surfaces in contact with each other is glued together. In the hinged model, all surfaces except the surface between the bolt head and washer, as well as the nut and transducer, are glued. The surfaces between the bolt/nut and washer/transducer, are connected at a single line around the center of the bolt, thus constraining it in a similar way to that used in Chapter 3. The scripts for the FE model of the full model are found on the Appendix CD[2].

The model is then meshed using the mesh size that was found to be converged for the bolt and structure. The washer and transducer are meshed with the same mesh size as the bolt. In Figure 5.4 and 5.5 the geometry and meshed model are seen.

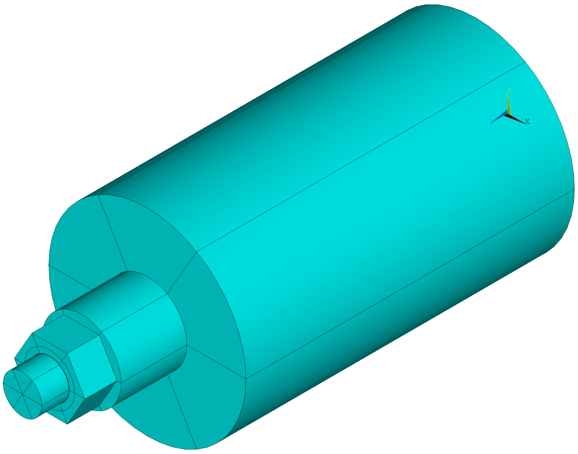

Figure 5.4 Geometry of the complete M12 structure.

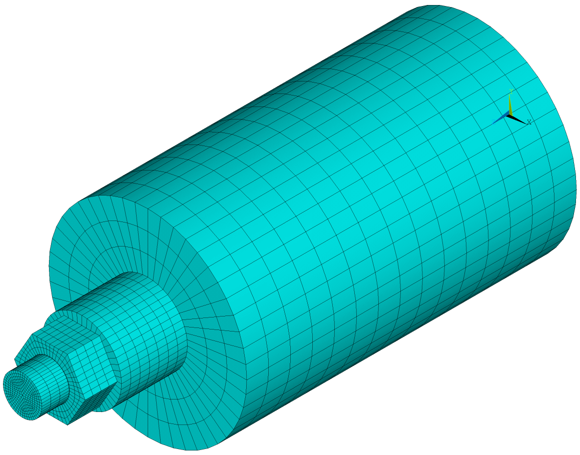

Figure 5.5 Meshed model of the complete M12 structure.

---

[1] Appendix CD\FE\Scripts\Structure \

[2] Appendix CD\FE\Scripts\Full Model \

As for the structure in itself, the modal analysis is performed without constraining the structure, for the complete system. Thus the first six eigenmodes are rigid body motions, and are removed from the presented results. The results from the analysis can be seen in Table 5.3. The scripts for the FE model of the structure are found on the Appendix CD[3].

	M12		**M18**		**M24**	
	Hinged	**Clamped**	**Hinged**	**Clamped**	**Hinged**	**Clamped**
f_1	3015Hz	3144Hz	4167Hz	4415Hz	5066Hz	5449Hz
f_2	3015Hz	3144Hz	4168Hz	4416Hz	5066Hz	5449Hz
f_3	7897Hz	8178Hz	9984Hz	10299Hz	9359Hz	9762Hz
f_4	7897Hz	8178Hz	9985Hz	10300Hz	9360Hz	9762Hz
f_5	10200Hz	10497Hz	10611Hz	11151Hz	11426Hz	12007Hz

Table 5.3 Eigenfrequencies found by the FE model for the structure with an M12, M18 and M24 bolt respectively. All modes are transverse, except M24 f_5 which is torsional.

Compared to the results for the bolt alone, it can be seen that the eigenfrequencies for the full model are slightly lower, with larger reduction for higher order modes. Looking at the results for the found eigenfrequencies, they are seen to correlate even better with the experiments than the model for the bolt alone, indicating that the model accurately depicts the behavior of the system. There are two exceptions to this, the second mode for the M12 and the first Mode for the M24. Initially the peaks at 10kHz found with the M12 bolt experiments, were thought to be the second mode as described in Chapter 2, however with the information from the modal analysis the results can be reevaluated. Based on the modal analysis it is clear that the small peaks around 8kHz, seen in Figure 2.19 are related to the second mode and that the group at 10kHz actually represents the third mode. The reason for the reduced response at 8kHz is not known but is expected to be caused by a difference in the mode shapes of the bolt, which will be examined in the following section. The first mode of the M24 bolt, which would be expected at around 5kHz, does not show up or give any indication that it could be there in the experimental results, this is also thought to be caused by a difference in the mode shape of the bolt, and will also be examined. The idea of the mode shape causing the reduction in response is shown on Figure 5.6, on the left hand side the mode shape of the bolt causes the surface of the cylinder to deflect in the same manner as the bolt, while the case shown on the right hand side, shows a transverse mode of the bolt to cause shearing motion in the cylinder.

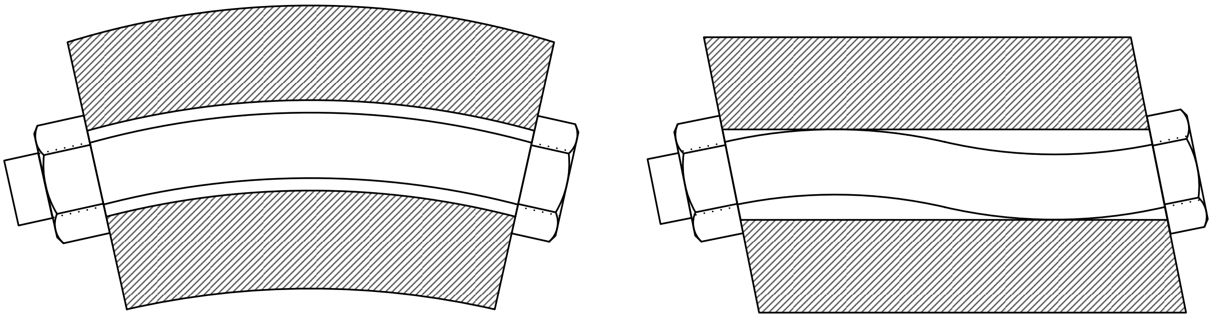

Figure 5.6 Difference in cylinder shape for different bolt modes.

It is not possible to determine whether this is the case accurately by simply observing the modeshapes of the entire structure. So get a clear view of what happens at different point in the structure, a harmonic analysis is necessary.

---

[3] Appendix CD\FE\Scripts\Structure \

5.3 Harmonic analysis

The purpose of doing a harmonic analysis is to gain a better understanding of what happens, at specific points of the structure at given frequencies. This will be used to determine whether it is possible to model the behavior of the structure surface accurately. As well as to determine whether the mode shapes of the bolt are causing the disappearance of eigenfrequencies in the experiments.

5.3.1 Modeling

To be able to perform a harmonic analysis, it is necessary to have a fully constrained model, thus the model used up until this point is not suitable. To constrain the model, in a way similar to that of the experiments, a series of springs are included in the model. Except for these springs, the model is identical to the one used to find the eigenfrequencies for the complete structure structure.

To include springs in the model, unidirectional COMBIN14 elements are used. These elements provide a specified amount of stiffness along its length, making it possible to imitate the effects of the strings used in the experiments. The strings are attached to the model at four points similar to the way the structure is suspended in the experiments. As these spring elements are unidirectional, three are needed at each location to properly constrain the structure in the x, y, and z-directions. The meshed model with boundary conditions can be seen in Figure 5.7, and the meshed model with the off centered force can be seen in Figure 5.8.

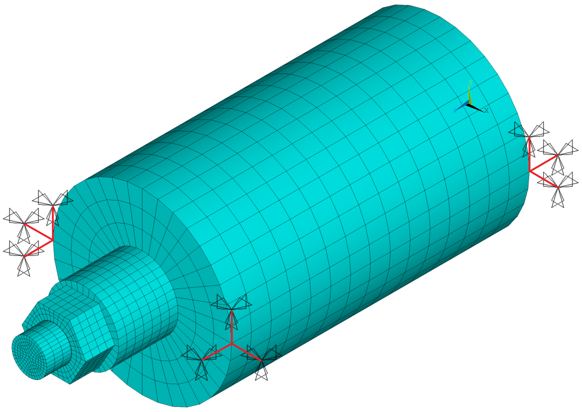

Figure 5.7 Meshed model for the harmonic analysis with the applied boundary conditions.

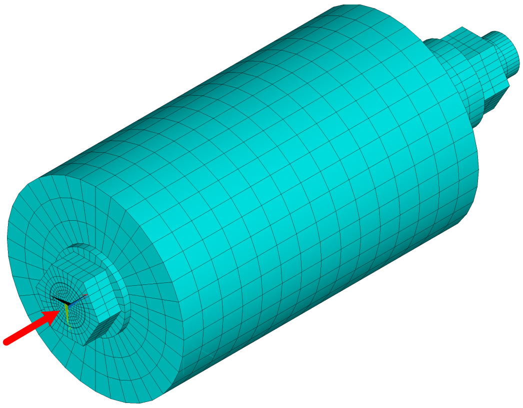

Figure 5.8 Meshed model for the harmonic analysis with the applied force.

In order to get a response in the system, a load has to be applied. This load is applied slightly off center at the bolt head, for the analysis a load of 100N is applied in the z direction. Although the used force is negligible as it will only scale the amplitude of the response, the level used is based on the force measured by the impact hammer in the experiments.

Determining string stiffness

To determine what stiffness should be for the springs, to best imitate the experimental conditions, a series of modal analysis are performed. The analysis is performed for the M12 model, for three different levels of string stiffness, the results can be seen in Table 5.4.

	String stiffness		
	100Pa	1MPa	1GPa
f_1	3015Hz	3015Hz	4057Hz
f_2	3015Hz	3015Hz	4126Hz
f_3	7897Hz	7897Hz	7932Hz
f_4	7897Hz	7897Hz	7950Hz
f_5	10200Hz	10200Hz	10329Hz

Table 5.4 Response for different levels of spring stiffness.

As it can be seen, a stiffness of 100Pa og 1MPa gives the same results as the results of the modal analysis of the unconstrained model, only differing in the first six modes, related to rigid body motion and thus excluded from the results. For a stiffness of 1GPa, a rise in frequencies are seen, these do not correlate well with the experimental results. For the stiffness of the springs a value of 1MPa is used, as 100Pa is seen as unlikely low. The scripts for the FE model of the full model are found on the Appendix CD[4].

5.3.2 Model verification

To determine whether the results obtained with the harmonic analysis are valid, a sweep of the frequency range used for the experiments has been performed. The sweep was performed for the system with the M12 bolt, with a resolution of 8Hz as this is the resolution of the experimental data. The response is taken at the same point as where acc2 is mounted, and in the same direction. The results of the sweep can be seen in Figure 5.9, and as it can be seen, they have a good correlation with the response from the experiments seen in Figure 2.19.

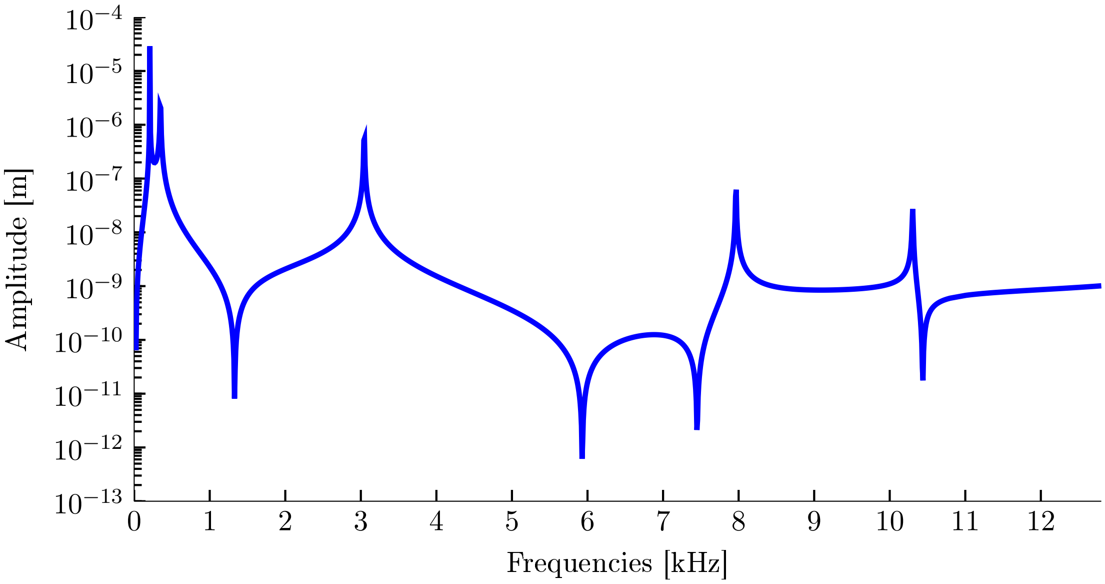

Figure 5.9 Harmonic response sweep for the complete M12 structure.

The response at the peaks for the complete structure, for both the M18 and M24 bolt size, has also been obtained, showing results comparable to those found during the experiments. The only exception is the prescense of the first resonance for the M24 bolt, but this will be investigated in the following.

As the results obtained with the harmonic analysis coincides with the experiments, the model is seen as valid and can thus be used to investigate parts of the structure, that are otherwise not possible to examine.

---

[4] Appendix CD\FE\Scripts\Full Model Harmonic \

5.3.3 Motion shape

To examine whether there is a difference in the movement of the bolt and cylinder surface, causing some of the expected resonant peaks to disappear, the motion of five points along each surface are examined. In Figure 5.10 the points at the cylinder, where the response is measured, can be seen. Each point is evaluated with regards to the magnitude of displacement in the x-direction, which is the same direction as acc2 is mounted, in the experiments.

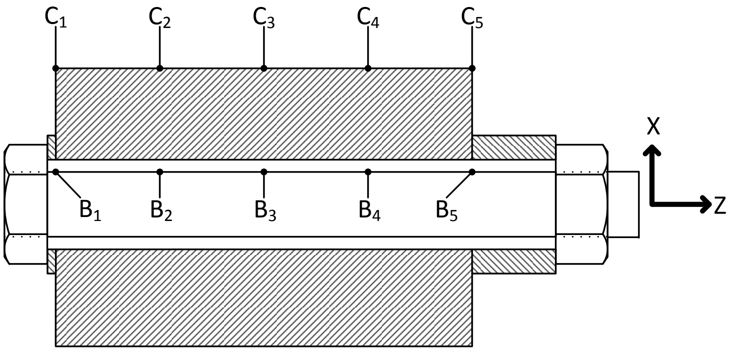

Figure 5.10 Measurement points for evaluating the motion of the bolt and cylinder.

The deflection of each point is then obtained at the resonant frequency. In Figure 5.11, to 5.19, the points are plotted for the first three modes of the three bolt sizes. Where the blue line in the figures represents the deflection of the structure surface and the red line represents the bolt surface, with displacement in meters plotted along the y-axis and the point number plotted along the x-axis.

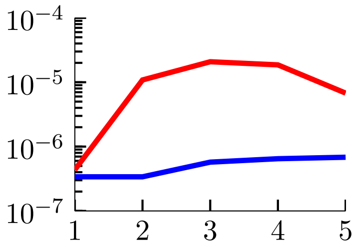

Figure 5.11 M12 mode 1.

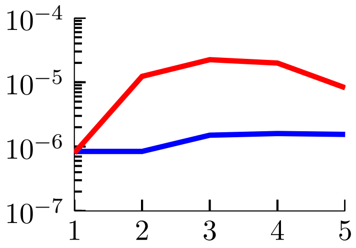

Figure 5.12 M18 mode 1.

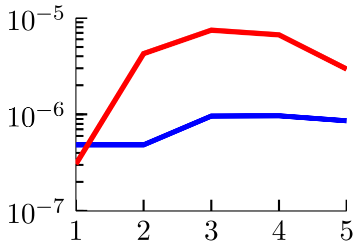

Figure 5.13 M24 mode 1.

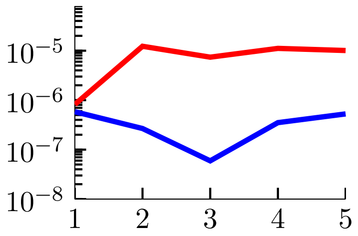

Figure 5.14 M12 mode 2.

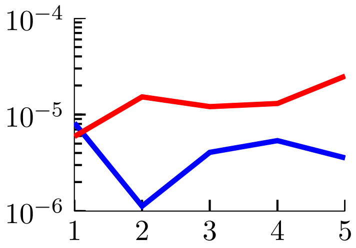

Figure 5.15 M18 mode 2.

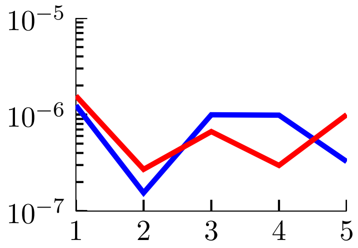

Figure 5.16 M24 mode 2.

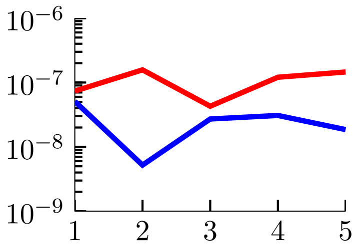

Figure 5.17 M12 mode 3.

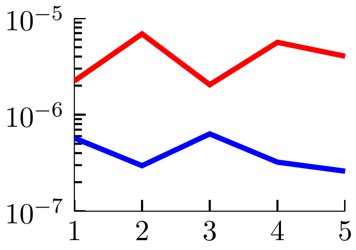

Figure 5.18 M18 mode 3.

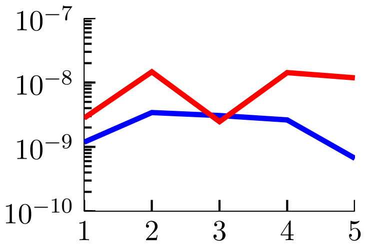

Figure 5.19 M24 mode 3.

As it can be seen from the shape outlined by the movement of the points, the first mode of the bolt and the structure exhibits the same motion, while the higher modes differ in movement. It can be seen that in the second mode for the M12 bolt, the point with the least movement is the point in the cylinder where the accelerometer is placed. which might explain the reduced response obtained from the second resonance in the experiments. The shape of the first mode for the M24 bolt does however not give any explanation of why this response is not seen in the experiments.

Another thing that can be seen from the figures is that there is a significant difference in the displacement amplitude between the bolt and the surface. Thus the larger displacement of the bolt, indicates that most of the energy that is put into the system goes to the bolt, and is not transferred to the surface of the cylinder, making it harder to obtain useful results with both the accelerometer and microphone. As examining the transmission between the motion of the bolt and the structure, might clarify why some resonances are not visible in the experiments, this is done in the following section.

5.3.4 Motion transmission

As previously described, there is a significant difference between the displacement amplitude for the bolt and structure. The purpose of this section is to examine this characteristic of the system, and the influence it has on the experimental results.

To examine the transmission between the bolt and the structure, the response for the bolt and structure at point B3 and C3 respectively is obtained. In Figure 5.20, 5.22, and 5.24 the response of the M12 bolt can be seen, for mode 1, 2, and 3 respectively. In Figure 5.21, 5.23, and 5.25 the ratio between the bolt and structure response can be seen for each mode.

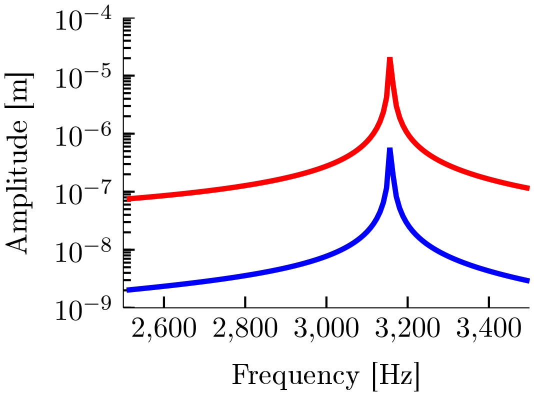

Figure 5.20 Mode 1 response.

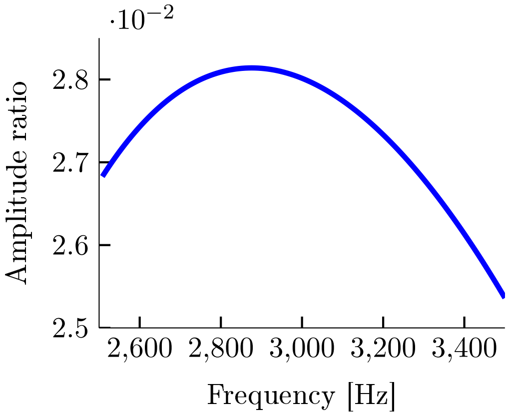

Figure 5.21 Mode 1 ratio.

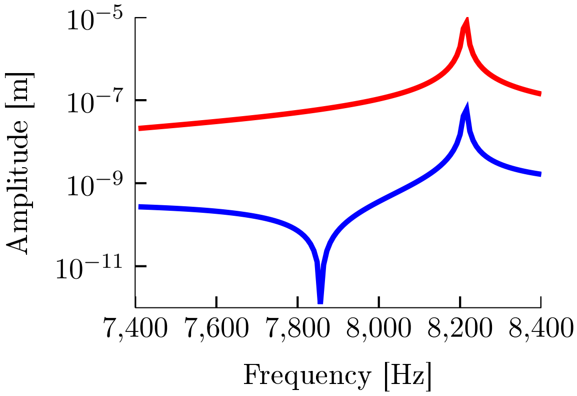

Figure 5.22 Mode 2 response.

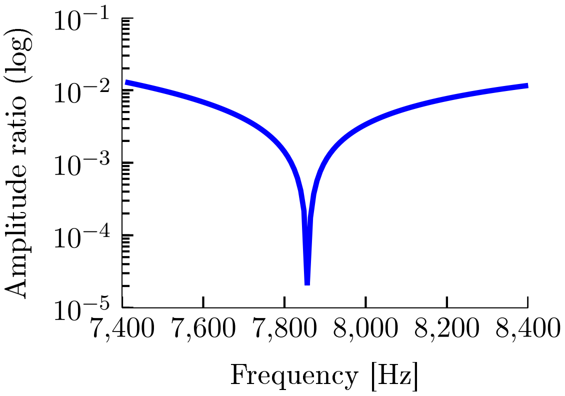

Figure 5.23 Mode 2 ratio.

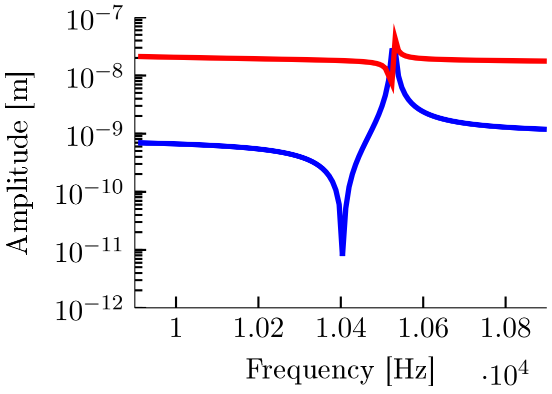

Figure 5.24 Mode 3 response.

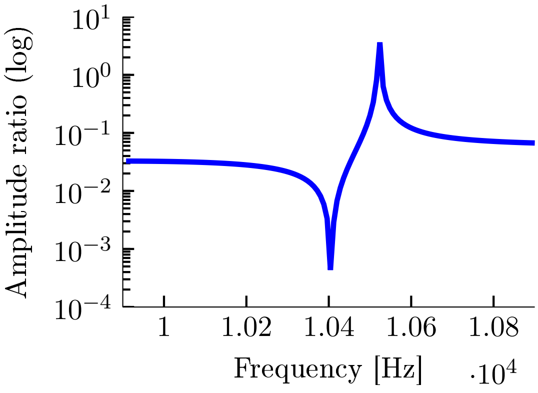

Figure 5.25 Mode 3 ratio.

As it can be seen from the figures, the ratio of the displacements is relatively stable, remaining in approximately the same magnitude, mainly diverging in the presence of resonances or anti resonances. To get a clearer picture of the behavior, some characteristics are displayed in Table 5.5, for the different bolt sizes and related modes. In the table the maximum amplitude for the bolt and structure, the average ratio, as well as the ratio between the peak amplitudes, is displayed. The average ratio is calculated as the average value of the ratios plotted in Figure 5.21, 5.23, and 5.25 for the M12 system, and the similarly the larger bolt sizes. The peak ratio is calculated as the ratio of the amplitudes at resonance for the bolt and structure. As for the plots presented above, the information in the table is based on data for point B3 and C3. With regards to the modes investigated, all are transverse, except for the third mode of the M24 bolt, which is torsional, as was found in Section 5.2.

Looking at the information in the table, it is seen that the ratio is generally increasing for higher bolt modes and larger bolt sizes. This means that even though, for example the first mode for the M12 bolt, gives a larger response than the first mode for the M24 bolt, the structural response is of the same magnitude. In relation to this it should be noted that, for the harmonic analysis the force applied is the same at all frequencies, while the force applied in the experiments decays with increasing frequency. This does however not explain how the second, but not the third mode, of the M12 test gives a reduced response, as the second mode has a twice as high amplitude under a constant force, and the higher frequency of the third does not increase the acceleration enough to account for a larger response. The same is the case for the first and second mode of the M24 bolt. One explanation of this could be that the modal participation factor for the location of the force in the experiments, does not coincide with the calculated response in the harmonic analysis.

Response amplitude (m)					
Bolt size	Mode	Bolt	Structure	Average ratio	Peak ratio
M12	1	$2.082 \cdot 10^{-5}$	$5.731 \cdot 10^{-7}$	0.027	0.027
	2	$7.405 \cdot 10^{-6}$	$5.932 \cdot 10^{-8}$	0.006	0.008
	3	$4.281 \cdot 10^{-8}$	$2.712 \cdot 10^{-8}$	0.099	0.633
M18	1	$2.241 \cdot 10^{-5}$	$1.503 \cdot 10^{-6}$	0.067	0.067
	2	$1.208 \cdot 10^{-5}$	$4.059 \cdot 10^{-6}$	1.049	0.336
	3	$2.044 \cdot 10^{-6}$	$6.327 \cdot 10^{-7}$	0.940	0.310
M24	1	$7.458 \cdot 10^{-6}$	$9.614 \cdot 10^{-7}$	0.132	0.129
	2	$6.662 \cdot 10^{-7}$	$9.945 \cdot 10^{-7}$	1.554	1.493
	3	$2.467 \cdot 10^{-9}$	$3.068 \cdot 10^{-9}$	1.696	1.244

Table 5.5 Characteristics of the motion transmission between the bolt and structure.

In order to test whether the modal participation factor, is the reason for the difference between the harmonic analysis and the experimental results, the FE model has been altered to apply the force differently. Instead of applying the force in a single direction. The force is applied in both the x, y and z direction, which will show how the structure is affected by changing the forcing conditions. In Figure 5.26 a full sweep of the entire frequency range can be seen. Here it is seen that under the changed forcing conditions, the second mode has the smallest response, while mode three has the largest. Thus the response for the new forcing condition a better correlation with the experiments can be observed compared to those shown on Figure 5.9.

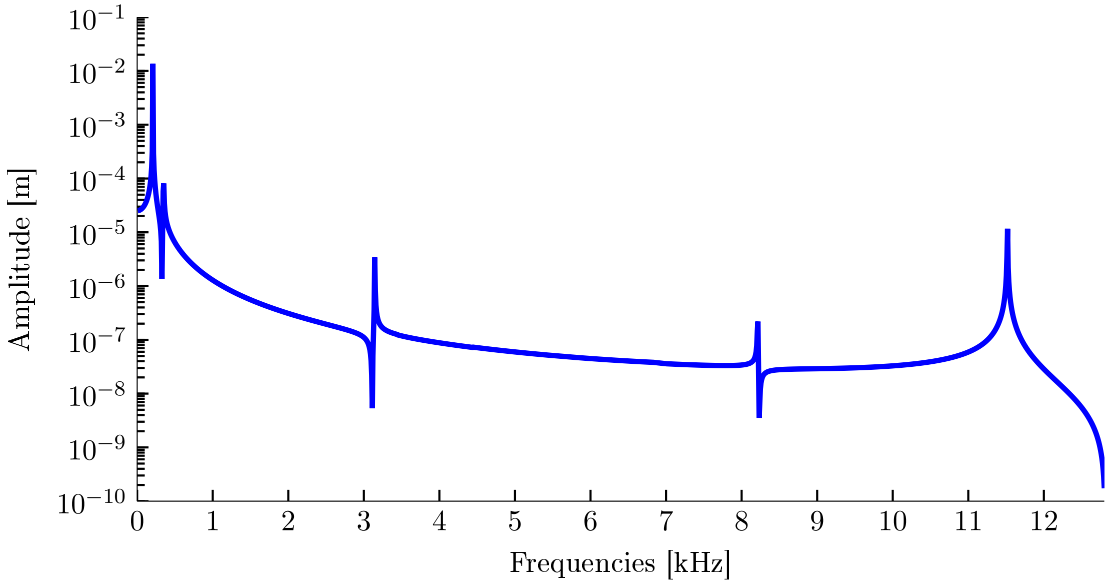

Figure 5.26 Harmonic response sweep for the complete M12 structure, with an altered force application.

To determine whether this is also the case for the M24 bolt, a sweep of a 1000Hz around the first and second mode has been performed, the response can be seen in Figure 5.27. From this it can be seen that the response of the second mode is larger than the first, confirming that the application of the force gives a significant change in the response.

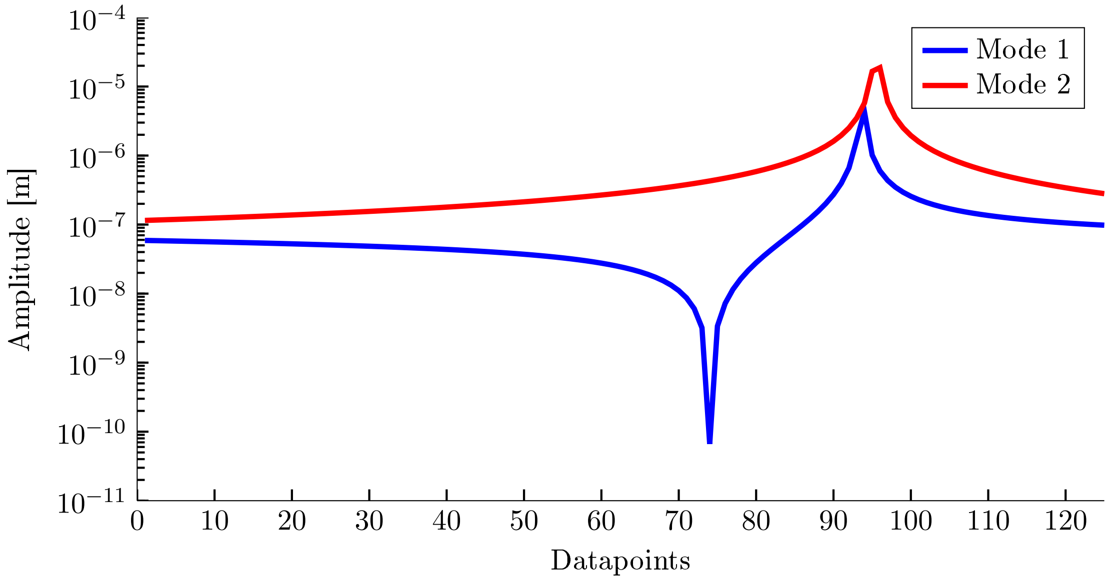

Figure 5.27 Difference in amplitude of mode 1 and 2 for the M24 system.

Another important thing is that looking at the experimental results for individual bolt sizes, the mode with the largest ratio seems to be associated with the largest response, both with regards to accelerations and acoustic emissions. Thus in order to better understand the transfer mechanism further investigation is required. This will be done in Chapter 6 where damping effects will also be included.

5.4 Summary

In this chapter, the complete system used for the experiments has been modeled, and used for investigating both the precision of the modeling method, and features of the system behavior that are not feasible to examine experimentally.

Initially the structure was modeled without the bolt to obtain its eigenfrequencies, which were verified by analytical solutions. It was found that the eigenfrequencies were significantly higher than those of the bolts, implying that especially the lower bolt modes are weakly coupled to the structure modes.

The models of the bolt and structure where then combined, and missing features were added. The eigenfrequencies of the complete system were then determined, and it was found that the frequencies for the complete model were somewhat lower than those of the bolt alone. This drop causes the frequencies of the system to coincide very well with the experimental results, thus verifying the model with respect to the real physical behavior of the system.

Lastly a harmonic analysis was performed for the complete system, allowing otherwise inaccessible details about the system to be determined. From this analysis it was found that there was a significant difference in the amplitudes of vibration between the bolt and the surrounding structure. The reason for this difference is not clear, so to better understand the mechanism, further investigation is necessary, which will be treated in Chapter 6. It was also found that the way that the forcing is applied to the system has a significant impact on the response.

6 Analytical model

In the FE analysis of the complete structure it was discovered, that the transmission of the vibrations from the bolt to the structure, variates according to the bolt type and the different modes. Thus it is necessary to investigate the transmission of vibrations, as this has a significant influence on the acoustic signal emitted. In order to investigate the transmission, an analytical model is created in this chapter. The analytical model is used to investigate the transmission of the signal and how the friction from the bolt head and the structure influences the transmission from the bolt to the structure.

To establish an analytical model, the complete system, shown in Figure 6.1, is decomposed. As the system has several components, each with their own set of resonant frequencies, these will influence each other in the complete system. Therefore the system can be decomposed into five subsystems, the structure, bolt, nut, washer, and transducer. However due to the geometry of the nut, washer, and transducer, their lowest eigenfrequencies are expected to be so much higher, than those of the structure and bolt, that their influence on the complete system's lowest resonant frequencies are negligible. These components are therefore not modeled individually in the analytical model, but are included in the subsystem of the bolt.

Thus the the complete system is decomposed into two parts, system A and system B. system A consists of a bolt, washer, and transducer and system B is the structure, the two systems are shown in Figure 6.2 and Figure 6.3 respectively. The analytical model needs to represent both system A and system B.

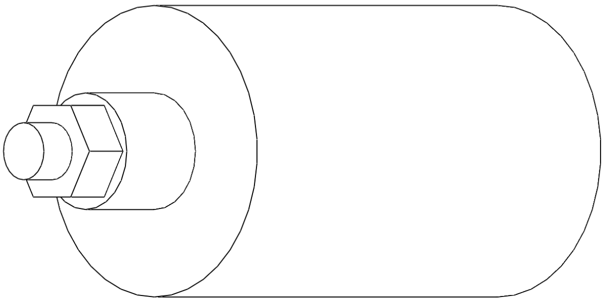

Figure 6.1 The complete system.

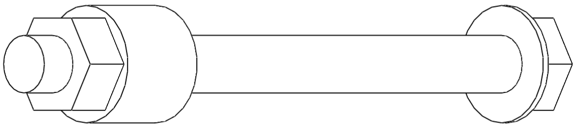

Figure 6.2 System A of the decomposed complete system.

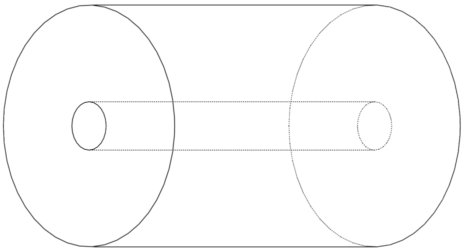

Figure 6.3 System B of the decomposed complete system.

When the two systems are combined, as the complete system, two different types of couplings can be observed. The first, is a weak coupling, where the first eigenfrequency of system A, is much lower than the first eigenfrequency of system B. The other, is a strong coupling, where the first eigenfrequency of system A and B is intermittent. The analytical model should be able to display both weak and strong coupling. During this report it is mostly the weak coupling that is investgated, but the M24 bolt tends to move away from the weak coupling towards the strong coupling. To complete the analysis of bolt vibration the strong coupling also needs to be investigated, as explained in Chapter 9.

System A can be further decomposed, as each mode can be represented, as a single d.o.f. system, by a stiffness and a mass. In order to include the friction between the bolt head and the structure a damper is included. System A is seen on Figure 6.4. System B is simplified to a cantilever beam, as this allows the structure to modeled as a continious system, enabling the transfer between bolt and structure to be examined.

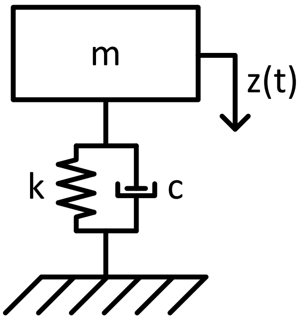

Figure 6.4 The analytical modeling for system A.

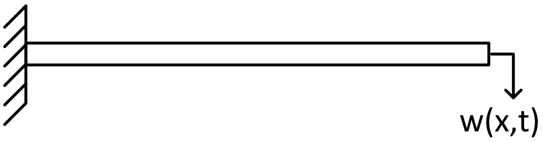

Figure 6.5 System B of the decomposed complete system.

The system A and B then have to be coupled to resemble the complete test system. By adding the spring/mass to the tip of the cantilever beam, the eigenfrequency of the spring/mass can be transferred to the beam. The experiments are performed by applying an impact force, thus the model is derived as a forced vibration system (harmonically excited structure). Hence the force is added to the mass and the response is connected to the beam by a spring and damper, that is able to vibrate both for the its own resonance frequencies and the vibrations transferred from the spring/mass.

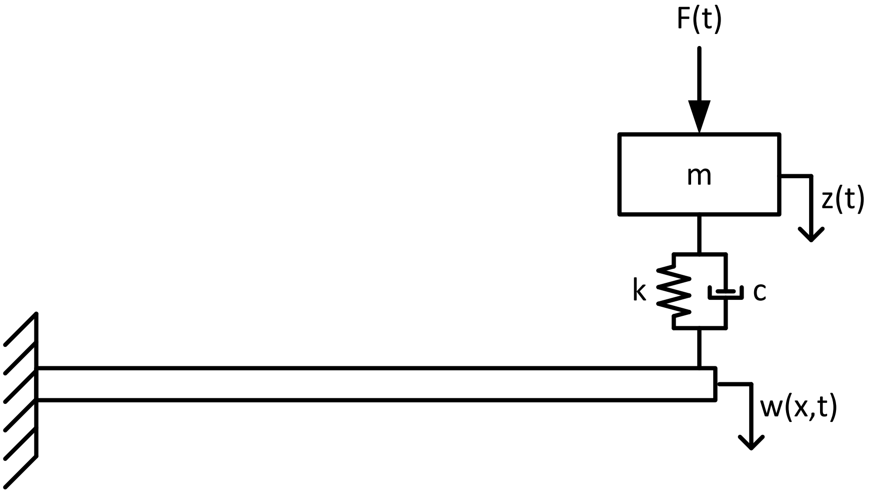

Figure 6.6 The spring, mass, and damper system used for analytical modeling.

The beam in the complete system is modeled as as continuous, to get the mode shape and structure behavior. The beam will initially be modeled with Bernoulli-Euler beam theory and later expanded to Timoshenko beam theory to investigate higher order modes. The spring/mass is modeled as a single degree of freedom system.

6.1 Deriving the governing equations

To model a vibrating system, several methods can be applied. To assure that most of the aspects of the system is covered, the most general principle, Hamilton's principle, is used. Which is the fundamental principle which several other methods, e.g. Rayleigh's method and Rayleigh-Ritz' method, is based on.

Hamilton's principle is based on D'Alembert principle, which is another way of expressing Newton's second law as $F - ma = 0$. Hamilton's principle is a variational method, where a solution is found by variation of a functional, to find the dynamics of a physical system. In this case the functional is the Lagrangian. The Lagrangian is the kinetic energy of a system subtracted by the potential energy in the system. Hamilton's principle is stated in Equation (6.1). [Shames and Cozzarelli, 1992]

$$\delta \int_{t_1}^{t_2} L_a \,\mathrm{d}t = \delta \int_{t_1}^{t_2} T - V \,\mathrm{d}t = 0 \tag{6.1}$$

where: [Shames and Cozzarelli, 1992]

δ	Variation, [-]
L_a	Lagrangian, [-]
t_1	Start time, [s]
t_2	end time, [s]
V	Potential energy, [J]
T	Kinetic energy, [J]

To model the system and find the eigenfrequencies it is necessary to consider the beam as a continuous system. If the beam is simplified to a spring, it is not possible to extract the modes of the beam from the model. Initially the known boundary conditions for the cantilever beam is stated in Equation (6.2) to Equation (6.4) as they are used several times throughout the derivation of the equations of motion for the system. For a cantilever beam the deflection and slope at the clamped end is equal to zero as stated in Equation (6.2) and Equation (6.3). The free end is subjected to a shear force by the spring and damper but no moment is present at the free end. Thus no curvature exists at the free end, as stated in Equation (6.4).

$$w(0,t) = 0 \tag{6.2}$$

$$\frac{\partial w(0,t)}{\partial x} = 0 \tag{6.3}$$

$$\frac{\partial^2 w(L,t)}{\partial x^2} = 0 \tag{6.4}$$

where:

$w(x,t)$	Deflection along the length of the beam, [m]

The kinetic energy is stated in Equation (6.5) and the potential energy is stated in Equation (6.6). The first part of each equation is for the beam and the last part is for the spring and mass. For the initial part of the derivation Hamilton's principle is used, and as it is only valid for systems that conserve energy, the damper and force is not included, but will be introduced later.

$$T = \frac{1}{2} \int_0^L \rho A_c \left(\frac{\partial\, w(x,t)}{\partial t} \right)^2 \mathrm{d}x + \frac{1}{2} m \left(\frac{\partial\, z(t)}{\partial t} \right)^2 \tag{6.5}$$

$$V = \frac{1}{2} \int_0^L EI \left(\frac{\partial^2 w(x,t)}{\partial x^2} \right)^2 \mathrm{d}x + \frac{1}{2} k \big(w(L,t) - z(t) \big)^2 \tag{6.6}$$

where:

L	Length, [m]
ρ	Density, $\left[\frac{kg}{m^3}\right]$
A_c	Cross sectional area, $\left[m^2\right]$
m	Mass, [kg]
E	Modulus of Elasticity, [GPa]
I	Area moment of inertia, $\left[m^4\right]$
k	Spring constant, $\left[\frac{N}{m}\right]$
$z(t)$	Mass deflection, [m]

For the compactness of the equations the time derivatives are denoted by a dot as $\frac{\partial\, z(t)}{\partial t} = \dot{z}$. The deflection derivatives are denoted by a prime as $\frac{\partial\, w(x,t)}{\partial x} = w'$. Furthermore $w(x,t)$ is referred to as w and when it is the deflection at a certain coordinate along the beam, fx. the deflection at the free is referred to as $w(L)$. $z(t)$ is also shortened and denoted as z.

By inserting the kinetic and potential energy from Equation (6.5) and Equation (6.6) into Hamilton's principle in Equation (6.1) the expression in Equation (6.7) is obtained.

$$\delta \int_{t_1}^{t_2} \left[\left(\frac{1}{2} \int_0^L \left(\rho A_c \dot{w}^2\right) \mathrm{d}x + \frac{1}{2} m \dot{z}^2 \right) - \left(\frac{1}{2} \int_0^L \left(E I w''^2\right) \mathrm{d}x + \frac{1}{2} k \big(w(L) - z\big)^2 \right) \right] \mathrm{d}t = 0 \tag{6.7}$$

Collecting the length integral terms from Equation (6.7) into one combined integral simplifies the expression as shown in Equation (6.8).

$$\delta \int_{t_1}^{t_2} \left[\frac{1}{2} \int_0^L \left(\rho A_c \dot{w}^2 - E I w''^2\right) \mathrm{d}x + \frac{1}{2} m \dot{z}^2 - \frac{1}{2} k \big(w(L) - z\big)^2 \right] \mathrm{d}t = 0 \tag{6.8}$$

As all terms of Equation (6.8) are multiplied by a half, this constant scaling is removed in Equation (6.9).

$$\delta \int_{t_1}^{t_2} \left[\int_0^L \left(\rho A_c \dot{w}^2 - E I w''^2\right) \mathrm{d}x + m \dot{z}^2 - k \big(w(L) - z\big)^2 \right] \mathrm{d}t = 0 \tag{6.9}$$

The delta operator is used to indicate the first variation. The variation of variables is carried out in Equation (6.10).

$$\int_{t_1}^{t_2} \left[\int_0^L \big(\rho A_c \dot{w}(\delta \dot{w}) - E I w''(\delta w'')\big) \mathrm{d}x + m \dot{z}\big(\delta \dot{z}\big) - k \big(w(L) - z\big)\big(\delta w(L) - \delta z\big) \right] \mathrm{d}t = 0 \tag{6.10}$$

To solve the variation of variables, integration by parts is utilized. Integration by parts is initially carried out for the length integral. To simplify Equation (6.10) when doing integration by parts, only the length integral is shown in Equation (6.11).

$$\int_0^L \left(\rho A_c \dot{w}\, \delta \dot{w} - E I w''\, \delta w''\right) \mathrm{d}x \tag{6.11}$$

The part in Equation (6.11) containing time derivatives is not affected by the integration of the length integral when doing integration by parts, thus Equation (6.12) is simplified even further.

$$\int_0^L \left(EIw''\,\delta w''\right)\mathrm{d}x \tag{6.12}$$

The general equation for integration by parts is stated in Equation (6.13), where u and dv is parts indside the integral from Equation (6.12).

$$\int_0^L u\,dv = [u\,v]_0^L - \int_0^L v\,du \tag{6.13}$$

Integrating and differentiating dv and u respectively yields v and du. If this is carried out for Equation (6.12) the results is stated in Equation (6.14) and Equation (6.15).

$$u = w'' \qquad dv = \delta w''\,\mathrm{d}x \tag{6.14}$$

$$du = w'''\,\mathrm{d}x \qquad v = \delta w' \tag{6.15}$$

Inserting Equation (6.14) and Equation (6.15) into Equation (6.13) yields the result of integration by parts which is stated in Equation (6.16).

$$\left[EIw''\,\delta w'\right]_0^L - \int_0^L \left(EI\delta w'\,w'''\right)\mathrm{d}x \tag{6.16}$$

It is seen that the part in Equation (6.16) that is outside the integral is equal to zero when applying the boundary conditions from Equation (6.3) and Equation (6.4). Equation (6.16) is integrated once more to find δw, still using integration by parts.

$$-\left[EIw'''\,\delta w\right]_0^L + \int_0^L \left(EIw''''\,\delta w\right)\mathrm{d}x \tag{6.17}$$

where:

$w'''(x,t)$	Third derivative of the beam deflection (change of curvature), $\left[\frac{1}{m^2}\right]$
$w''''(x,t)$	Fourth derivative of the beam deflection, $\left[\frac{1}{m^3}\right]$

Equation (6.17) is simplified to Equation (6.18) by applying the boundary condition stated in Equation (6.2).

$$-EIw'''(L)\,\delta w(L) + \int_0^L \left(EIw''''\,\delta w\right)\mathrm{d}x \tag{6.18}$$

In Equation (6.18) the variation of the length integral is found. Then integration by parts is carried out for the time integral but only on the part inside the double integral, as shown in Equation (6.19). The results of the integration by parts is shown in Equation (6.20).

$$\int_{t_1}^{t_2}\int_0^L \left(\rho A_c\dot{w}(\delta\dot{w}) - EIw''(\delta w'')\right)\mathrm{d}x\,\mathrm{d}t \tag{6.19}$$

$$\left[\rho A_c\dot{w}\delta w\right]_{t_1}^{t_2} - \int_{t_1}^{t_2} \rho A_c\ddot{w}\delta w\,\mathrm{d}t \tag{6.20}$$

The part in Equation (6.20) that is outside the integral still have definite boundaries, is neglected. As the virtual displacement field is zero at the time limits t_1 and t_2 [Shames and Cozzarelli, 1992]. Continuing to do integration by parts on the time integral outside the double integral leaves the the mass to be integrated, which is done in Equation (6.21).

$$\int_{t_1}^{t_2} m\dot{z}\delta\dot{z}\,\mathrm{d}t \tag{6.21}$$

$$[m\ddot{z}\delta z]_{t_1}^{t_2} - \int_{t_1}^{t_2} m\ddot{w}\delta w\,\mathrm{d}t \tag{6.22}$$

As the same assumption about time is used on Equation (6.22) as used on Equation (6.20) the part outside the integral vanishes. Then all the results from integration by parts is inserted back into Equation (6.10) and this yields Equation (6.23).

$$\begin{aligned}\int_{t_1}^{t_2}\Bigg\{\int_0^L \Big[-\rho A_c\ddot{w}\delta w - EIw''''\delta w\Big]\,\mathrm{d}x + EIw'''(L)\delta w(L) - m\ddot{z}\delta z \\ -k\big(w(L)-z\big)\delta w(L) + k\big(w(L)-z\big)\delta z\Bigg\}\,\mathrm{d}t = 0\end{aligned} \tag{6.23}$$

The terms in Equation (6.23) that contains common variational terms is grouped in Equation (6.24).

$$\begin{aligned}\int_{t_1}^{t_2}\Bigg\{\int_0^L \Big[\big(-\rho A_c\ddot{w} - EIw''''\big)\delta w\Big]\,\mathrm{d}x - \big(-EIw'''(L) + kw(L) - kz\big)\delta w(L) \\ -\big(m\ddot{z} - kw(L) + kz\big)\delta z\Bigg\}\,\mathrm{d}t = 0\end{aligned} \tag{6.24}$$

As Equation (6.24) has to be equal to zero and the three terms δw, $\delta w(L)$, and δz are arbitrary of value, the rest of the three terms must be equal to zero. Thus three equations can be derived and these are stated in Equation (6.25) to Equation (6.27).

$$-\rho A_c\ddot{w} - EIw'''' = 0 \tag{6.25}$$

$$-EIw'''(L) + kw(L) - kz = 0 \tag{6.26}$$

$$m\ddot{z} - kw(L) + kz = 0 \tag{6.27}$$

Since the applied force and the damper was excluded in the beginning, these are now added to the model. Equation (6.25) to Equation (6.27) is no longer terms of energy but is purely force equilibrium, thus the applied load can be added. The damper dissipates energy over time and is not included in Hamilton's principle and another method is used to find the energy dissipated, which is described in Section 6.4.1. The damping force can be added to Equation (6.26) and Equation (6.27), acting opposite to the direction of the relative movement of the mass and the beam. This is done by Rayleigh's dissipation. Rayleigh's dissipation function is added to the equations of motion. Rayleigh dissipation function is stated in Equation (6.28) and is used for fx viscous damping forces that are proportional to velocities. [Rao, 2011]

$$R_d = \frac{1}{2}[c]\dot{q}^{\,2} \tag{6.28}$$

where:

c	Damping constant, $[\frac{N\,s}{m}]$
R_d	Rayleighs dissipation, [N]
$\dot{q}$	Degrees of freedom, [-]

As the velocity applied to the damper is the relative velocity of the mass and beam tip, Equation (6.28) is rewritten to fit the analytical system and the relative velocity in Equation (6.29).

$$R_d = \frac{1}{2}c\big(\dot{z} - \dot{w}(L)\big)^2 \tag{6.29}$$

Rayliegh dissipation can not be inserted into the equations of motion directly, but using Lagrange Equation to derive the damper will yield a solution. Lagrange equation is stated in Equation (6.30). Since the kinetic and potential energy is found by using Hamilton's principle those parts are neglected and only the damper part is left.

$$\frac{\mathrm{d}}{\mathrm{d}t}\left(\frac{\partial T}{\partial \dot{q}}\right) + \frac{\partial V}{\partial \dot{q}} + \frac{\partial R_d}{\partial \dot{q}} = F \tag{6.30}$$

where:

F	Force, [N]

In Equation (6.31) and Equation (6.32) the expression for the damper is found for each degree of freedom.

$$\frac{\partial R_d}{\partial \dot{z}} = c\big(\dot{z} - \dot{w}(L)\big)^2 \tag{6.31}$$

$$\frac{\partial R_d}{\partial \dot{w}(L)} = -c\big(\dot{z} - \dot{w}(L)\big)^2 \tag{6.32}$$

A solution for the damper is now found and for a system that both contains forced motion and damping, the general equation of motion is stated in Equation (6.33). Where it is seen that the damping force is the damping coefficient times the velocity, exactly as the solution in Equation (6.31) and Equation (6.32).

$$[m]\ddot{\vec{z}} + [c]\dot{\vec{z}} + [k]\vec{z} = F \tag{6.33}$$

Equation (6.33) is used to to expand the terms stated in Equation (6.26) and Equation (6.27). Adding the applied force and damping force from Equation (6.31) to Equation (6.27) as this is the equation that describes motion of the mass and applying the damping force from Equation (6.32) to Equation (6.26), that describes the motion of the beam tip.

$$\rho A_c \ddot{w} + EIw'''' = 0 \tag{6.34}$$

$$-EIw'''(L) + c\big(\dot{w}(L) - \dot{z}\big) + k\big(w(L) - z\big) = 0 \tag{6.35}$$

$$m\ddot{z} + c\big(\dot{z} - \dot{w}(L)\big) + k\big(z - w(L)\big) = F \tag{6.36}$$

The applied force is a oscillating force that is time dependent as stated in Equation (6.37). As the problem is force dependent, the force oscillates in order to make it a vibrational problem.

$$F(t) = F_0\,\mathrm{e}^{i\omega t} \tag{6.37}$$

where:

F_0	The amplitude of the applied force, [N]

The deflection $w(x, t)$ in Equation (6.34), (6.35), and (6.36) is found by the method separation of variables as stated in Equation (6.38). The forced vibrations is a function of time and vibrates with the shape of $\mathrm{e}^{i\omega t}$, thus the response must follow and have the same shape.

$$w(x) = W(x)\,\mathrm{e}^{i\omega t} \tag{6.38}$$

where:

$W(x)$	Assumed solution for the beam deflection, [m]
ω	Frequency, $\left[\frac{rad}{s}\right]$

By substituting Equation (6.38) into the equation of the beam vibrations stated in Equation (6.34) and solving the problem when $W(x) = C\,\mathrm{e}^{\beta x}$ the solution is then found as stated in Equation (6.39).

$$W(x) = C_1\cos(\beta x) + C_2\sin(\beta x) + C_3\cosh(\beta x) + C_4\sinh(\beta x) \tag{6.39}$$

where: [Rao, 2011]

C_i	Constant, [-]

The constant β is a combination of beam parameters and the material of the beam from Equation (6.34). The constant is stated in Equation (6.40).

$$\beta^4 = \frac{\rho A_c \omega^2}{EI} \tag{6.40}$$

The deflection of the mass is also dependent on the time as stated in Equation (6.41).

$$z(t) = Z_0\,\mathrm{e}^{i\omega t} \tag{6.41}$$

where:

Z_0	The amplitude of motion of the mass, [m]

The displacement of the system can not yet be determined as there is five unknown constants to be determined. Utilizing Equation (6.35), Equation (6.36), Equation (6.2), Equation (6.3), and Equation (6.4) a system of five equations with five unknowns is obtained. Fortunately the system can be simplified by applying the boundary conditions for the clamped end, stated in Equation (6.2) and Equation (6.3). Applying the first boundary condition leads to $w(0) = W(0) = 0$. For $W(0) = 0$ to be valid the cosine and hyperbolic cosine parts of Equation (6.39) must be either equal to zero or have apposite operational signs as $C_1 + C_3 = 0$. The same applies for the boundary condition $W'(0) = 0$ where $C_2 + C_4 = 0$. Thus Equation (6.39) simplifies to Equation (6.42) and three equations with three unknowns.

$$W(x) = C_1\big(\cos(\beta x) - \cosh(\beta x)\big) + C_2\big(\sin(\beta x) - \sinh(\beta x)\big) \tag{6.42}$$

The system of equations to be solved is then three equations with three unknowns and they are stated in Equation (6.43) to Equation (6.45).

$$-EIw'''(L) + c\big(\dot{w}(L) - \dot{z}\big) + kz - kw(L) = 0 \tag{6.43}$$
$$m\ddot{z} + c\big(\dot{z} - \dot{w}(L)\big) + kz - kw(L) = F \tag{6.44}$$
$$w''(L) = 0 \tag{6.45}$$

The derivatives needed in the system of equations is found in Equation (6.46) to Equation (6.49).

$$\dot{z} = i\omega Z_0 \, \mathrm{e}^{i\omega t} \tag{6.46}$$
$$\ddot{z} = -\omega^2 Z_0 \, \mathrm{e}^{i\omega t} \tag{6.47}$$
$$\dot{w} = i\omega W(x) \, \mathrm{e}^{i\omega t} \tag{6.48}$$
$$w' = W'(x) \, \mathrm{e}^{i\omega t} \tag{6.49}$$

The derivatives is then inserted and it is seen that every part contains the exponential expression.

$$-EIW'''(L)\,\mathrm{e}^{i\omega t} + c\big(i\omega W(L)\,\mathrm{e}^{i\omega t} - i\omega Z_0\,\mathrm{e}^{i\omega t}\big) + kZ_0\,\mathrm{e}^{i\omega t} - kW(L)\,\mathrm{e}^{i\omega t} = 0 \tag{6.50}$$
$$-\omega^2 Z_0\,\mathrm{e}^{i\omega t} m + c\big(i\omega Z_0\,\mathrm{e}^{i\omega t} - i\omega W(L)\,\mathrm{e}^{i\omega t}\big) + kZ_0\,\mathrm{e}^{i\omega t} - kW(L)\,\mathrm{e}^{i\omega t} = F_0\,\mathrm{e}^{i\omega t} \tag{6.51}$$
$$W''(L)\,\mathrm{e}^{i\omega t} = 0 \tag{6.52}$$

The exponential expression is canceled out, which means that the equations of motion are written in the frequency domain. Furthermore, the frequency is changed from being expressed in $\frac{rad}{s}$ to Hz, so results are directly comparable to tests and FE results.

$$-EIW'''(L) + c\big(W(L) - Z_0\big)i\,(f2\pi) + k\big(Z_0 - W(L)\big) = 0 \tag{6.53}$$
$$-(f2\pi)^2\, Z_0 m + c\big(Z_0 - W(L)\big)i\,(f2\pi) + k\big(Z_0 - W(L)\big) = F_0 \tag{6.54}$$
$$W''(L) = 0 \tag{6.55}$$

where:

f	Frequency, [Hz]

From Equation (6.53) to Equation (6.55) it is seen that the derivatives of the deflection, stated in Equation (6.42) is used. The derivatives of the deflection are derived in Equation (6.56) to Equation (6.58).

$$W'(x) = -C_1\beta\big(\sin(\beta x) + \sinh(\beta x)\big) + C_2\beta\big(\cos(\beta x) - \cosh(\beta x)\big) \tag{6.56}$$
$$W''(x) = -C_1\beta^2\big(\cos(\beta x) + \cosh(\beta x)\big) - C_2\beta^2\big(\sin(\beta x) + \sinh(\beta x)\big) \tag{6.57}$$
$$W'''(x) = C_1\beta^3\big(\sin(\beta x) - \sinh(\beta x)\big) - C_2\beta^3\big(\cos(\beta x) + \cosh(\beta x)\big) \tag{6.58}$$

By inserting the derivatives into Equation (6.53) to Equation (6.55), the system can be solved for C_1, C_2, and Z_0 and the results of the constants is imaginary if there is a damping force and only real if no damping is present. The constants are then added to Equation (6.42) which is used to find the deflection along the length of the cantilever beam. Since the deflection solution is complex, the amplitude of the beam deflection is found by Equation (6.59) where the real and imaginary parts are added.

$$A_m = \sqrt{Re^2 + Im^2} \tag{6.59}$$

where:

A_m	Amplitude, [m]

The amplitude of the mass deflection z is also found by Equation (6.59), where the real and imaginary parts from the constant Z_0 are used. The MATLAB script, created to run the Bernoulli-Euler model, is attached on the Appendix CD[1]. The Bernoulli-Euler model is verified in Appendix D and is found trustworthy.

6.2 Timoshenko Beam

Based on the results of the performed experiments, and behavior observed from the FE model of the system, the possibility of investigating higher order modes, is desirable. Thus it is also necessary to expand the analytical model from Bernoulli-Euler beam theory into Timoshenko beam theory, as it more accurate at higher order modes, due to the inclusion of angular displacement. The derivation of the equation of motions from the kinetic and potential energy by using Hamilton's principle is not stated here but is seen in Appendix E, as the procedure is identical to the one shown in Section 6.1.

The final equations for the the Timoshenko beam theory is stated in Equation (6.60) to Equation (6.66) and it is seen that the system is stated by seven equations. Equation (6.60) and Equation (6.61) is used for derivation of the assumed solutions of the deflection and angular displacement. This leaves five equtions with five unknowns, thus Equation (6.62) to Equation (6.66) is used to solve the system. In the Bernoulli-Euler beam theory solution the system of equations and unknowns is reduced by introducing the boundary conditions, but this is not possible for the Timoshenko beam theory.

$$\kappa G A_c\big(W''(x) - \Psi'\big) - \rho A_c\,(f2\pi)^2\,W(x) = 0 \tag{6.60}$$

$$\kappa G A_c\big(W' - \Psi\big) - \rho I\,(f2\pi)^2\,\Psi(x) + EI\Psi''(x) = 0 \tag{6.61}$$

$$-\,m\,(f2\pi)^2\,Z_0 + c\big(Z_0 - W(L)\big)i\,(f2\pi) + k\big(Z_0 - W(L)\big) = F \tag{6.62}$$

$$-\,\kappa G A\big(W'(L) - \Psi(L)\big) + c\big(Z_0 - W(L)\big)i\,(f2\pi) + k\big(Z_0 - W(L)\big) = 0 \tag{6.63}$$

$$W(0) = 0 \tag{6.64}$$

$$\Psi(0) = 0 \tag{6.65}$$

$$\Psi'(L) = 0 \tag{6.66}$$

where:

$W(x)$	Assumed solution for the beam deflection, [m]
$\Psi(x)$	Assumed solution for the beam angular displacement, [-]

The assumed deflection and angular displacement is stated in Equation (6.67) and Equation (6.68), derived from Equation (6.60) and Equation (6.61).

$$W(x) = \Big(\beta_1\cos(\lambda_1 x) + \beta_2\sin(\lambda_1 x) + \beta_3\cosh(\lambda_2 x) + \beta_4\sinh(\lambda_2 x)\Big) \tag{6.67}$$

$$\begin{aligned}\Psi(x) = \Bigg(&\frac{\kappa G\beta_2\lambda_2^2 + \rho\beta_2\omega^2}{\kappa G\lambda_2}\cos(\lambda_1 x) + \frac{\kappa G\beta_1\lambda_2^2 + \rho\beta_1\omega^2}{\kappa G\lambda_2}\sin(\lambda_1 x)\\ &+\frac{\kappa G\beta_4\lambda_1^2 - \rho\beta_4\omega^2}{\kappa G\lambda_1}\cosh(\lambda_2 x) + \frac{\rho\beta_3\omega^2 - \kappa G\beta_3\lambda_1^2}{\kappa G\lambda_1}\sinh(\lambda_2 x)\Bigg)\end{aligned} \tag{6.68}$$

---

[1] Appendix CD\MATLAB \Analytical\BeamMass.m

This solution to the analytical model is verified by comparing the results to the Bernoulli-Euler solution. The Timoshenko model is considered as valid as spring/mass solutions and first beam eigenfrequency is identical to the Bernoulli-Euler theory. Higher order modes in the Timoshenko are lower than the Bernoulli-Euler solutions. Thus the Timoshenko model is used from now on and the MATLAB script for the Timoshenko model is attached on the Appendix CD[2].

6.3 System with damping

Until now the damper has not been included in the verification of the model. The damper influences the system especially oscillations over time as they will die out instead of the system conserving the energy applied. The damper is interesting to implement as it might give an indication of the influence of damping on the real test structure.

When the damper is initially inserted, the system has to be tested to ensure that the response of the analytical model is correct. The implementation of the damper is tested in Section 6.3.1. When the full system is trustworthy the model is updated to contain parameters reflecting the test setup and results is then compared with test results.

6.3.1 Verification of system with damper

Both the Bernoulli-Euler and Timoshenko model contains a damper, but the verification of the influence of the damper is only carried out on the Timoshenko model, as this model is used for the final comparison with test results. To test the structure where a damper is included it is necessary to compare it to a reference. Thus the beam is yet again decoupled to act as ground so the spring/mass/damper system can be compared to elementary results and the MATLAB script for the damped Timoshenko model is attached on the Appendix CD[3]. The resonant frequency of a spring/mass/damper system can be found by Equation (6.69), where the undamped resonant frequency can be found by Equation (D.3).

$$\omega_d = \omega_n \sqrt{1-\zeta^2} \tag{6.69}$$

where:

ω_d	Damped eigenfrequency, $\left[\frac{rad}{s}\right]$
ω_n	Undamped Eigenfrequency, $\left[\frac{rad}{s}\right]$
ζ	Damping ratio, [-]

The damping ratio is found in Equation (6.70) and is found on the current damping constant and the critical damping constant. The critical damping constant descibes when the system is critically damped which is when the system do no longer oscillate.

$$\zeta = \frac{c}{c_c} \tag{6.70}$$

where:

c	Damping constant, $\left[\frac{N\,s}{m}\right]$
c_c	Critical damping constant, $\left[\frac{N\,s}{m}\right]$

The critical damping constant is found in Equation (6.71).

---

[2] Appendix CD\MATLAB \Analytical\TimoshenkoModel.m

[3] Appendix CD\MATLAB \Analytical\DamperTimoshenko.m

$$c_c = 2\sqrt{km} \tag{6.71}$$

where:

k | Spring constant, $[\frac{N}{m}]$

m | Mass, [kg]

The damped eigenfrequency can now be found and it is can be seen from Equation (6.69) that the damped eigenfrequency is lower than the undamped. Initially the fitted parameters from Section 6.5 stated in Table 6.3 is utilized and damping constants from 2 to $8\frac{Ns}{m}$ with intervals of $2\frac{Ns}{m}$. For these small dampings, the model yields exact solutions but if damping constants from 50 to $200\frac{Ns}{m}$ with intervals of $50\frac{Ns}{m}$ the model do not yield exact solutions. The expected eigenfrequencies is calculated by Equation (6.69) to Equation (6.70) and is stated in the second column of Table 6.1.

Damping constant	Resonant frequency [Hz]	Model resonant frequency [Hz]
50	3039.94	3039.88
100	3039.75	3039.49
150	3039.43	3038.85
200	3038.98	18.01

Table 6.1 Damping constants and expected resonance frequencies for the spring/mass part of the Timoshenko model model.

The response of the decoupled system is calculated for a frequency range of 2900Hz to 3200Hz with intervals of 1Hz but refined at frequnecies of 3037.5 to 3040.5 with an interval of 0.01Hz. The calculated response of the the beam is seen in Figure 6.7.

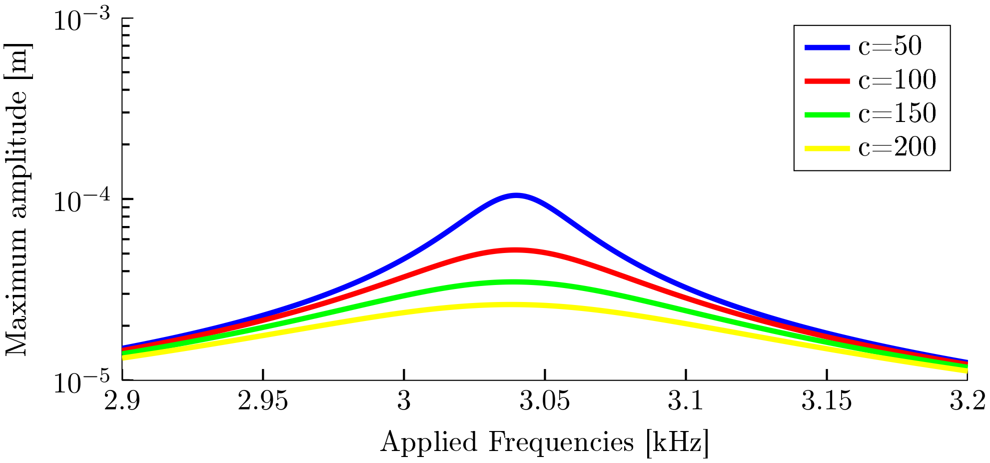

Figure 6.7 Response obtained of the spring/mass/damper system with various damping constants.

From Figure 6.7 it is seen that the response of the system with damping is not identical to what is expected from the second column of Table 6.1. The exact peaks is listed in the third column of Table 6.1. Each of the responses seen in Figure 6.7 are plotted individually and found in Section E.3 in Figure E.7 to Figure E.10.

Homogenous systems is unforced and contains a natural eigenfrequency that is determined only from the mass and the spring parameters. The eigenfrequency can be found by Equation (6.69). A harmonic excited system is a system that is forced. Thus the system is forced to vibrate at different frequencies and a resonant frequency is found when the amplitude of the deflection is at its maximum.

The analytical problem is a forced problem and hereby, Equation (6.69) can not be used as it is only valid for free vibrations. In order to calculate the damped response for a harmonic excited system, the damped harmonically excited resonant frequency is derived in Section E.5 and restated in Equation (6.72).

$$\omega_r = \omega_n \sqrt{1 - 2\zeta^2} \tag{6.72}$$

where:

ω_n	Undamped Eigenfrequency, $\left[\frac{rad}{s}\right]$
ω_r	Resonant frequency, $\left[\frac{rad}{s}\right]$

By evaluating Equation (6.69) and Equation (6.72), it is clear that the model yields identical solutions to what is estimated, for low damping. When the damping is larger the results deviate. Which was discovered by the results from the analytical model, stated in Table 6.1. Thus the influence of the damping is neglectible for small values but a difference is present when larger damping is applied. Using Equation (6.72), it is possible to estimate the harmonically excited resonance frequencies for the damping coefficients of 50 to 200 $\frac{Ns}{m}$. The harmonic results is stated in Table 6.2.

Damping constant	Harmonic [Hz]	Model [Hz]
50	3039.88	3039.88
100	3039.49	3039.49
150	3038.85	3038.85
200	3037.95	3037.94

Table 6.2 Damping constants and expected resonant frequencies for the spring/mass part of the Timoshenko model model.

The analytical model is considered to be valid as the results stated in Table 6.2 is almost identical.

6.4 Specific damping capacity

During this section the energy dissipated by the damper is found for a given frequency. It is necessary to prove that the damper dissipates energy but what is interesting is how much energy is dissipated at different frequencies. Furthermore the energy in the system for a given frequency is found. If the dissipated energy is divided by the energy in the system, the specific damping capacity can be found, as stated in Equation (6.73).

$$\Psi_d = \frac{\Delta W_d}{W_e} \tag{6.73}$$

where:

ΔW_d	Dissipated energy, [J]
W_e	Energy in the system, [J]
Ψ_d	Specific damping capacity ratio, [-]

By changing the damping constant in the analytical model, it is possible to obtain the response of the system and see how the damping influences the response and how the specific damping capacity of the system changes. To do so it is necessary to derive the energy dissipated by the damper and the energy in the system descibed in Section 6.4.1 and Section 6.4.2 respectively.

6.4.1 Energy dissipated by the damper

A damper in an analytical model dissipates energy and ensures that a system does not oscillate forever. It is relevant for this system to see how much energy that is dissipated at different damping ratios and frequencies. Furthermore the energy dissipated can not be included in Hamilton's principle, thus another method is required to prove that the damper dissipates energy.

The dissipated energy is the force times velocity and the force from a damper is damping constant times velocity and the dissipated energy is described as stated in Equation (6.74). This equation is also valid for a system with a spring in parallel with the damper even if the spring is neglected [Rao, 2011].

$$\dot{W} = F\,v = c\,v^2 \tag{6.74}$$

where:

v	Velocity, $\left[\frac{m}{s}\right]$
F	Force, [N]
$\dot{W}$	Change of energy over time, [-]
c	Damping constant, $\left[\frac{N\,s}{m}\right]$

There is no specific velocity applied to the damper in the system described, instead a relative velocity is applied. The velocity is described in Equation (6.75) where the relative velocity is found.

$$v = \big(\dot{z} - \dot{w}(L)\big) \tag{6.75}$$

By remembering the velocity of the beam and mass stated in Equation (6.46) and Equation (6.48) respectively, Equation (6.75) can be expanded as shown in Equation (6.76).

$$v = \big(i\omega Z_0\,\mathrm{e}^{i\omega t} - i\omega W(L)\,\mathrm{e}^{i\omega t}\big) \tag{6.76}$$

Only the real part of the velocity is to be used as it is a real system that is evaluated. Thus the exponential term is expanded to a real and imaginary part as $\mathrm{e}^{i\omega t} = \cos(\omega t) + i\sin(\omega t)$. Which is inserted into Equation (6.76) and is shown in Equation (6.77).

$$v = \Big(i\omega Z_0\big(\cos(\omega t) + i\sin(\omega t)\big) - i\omega W(L)\big(\cos(\omega t) + i\sin(\omega t)\big)\Big) \tag{6.77}$$

From the solution of the analytical model with a damper it is known that both Z_0 and $W(L)$ contains imaginary parts. Thus the values from Equation (6.77) are split into a real and imaginary part as well as shown in Equation (6.78) and Equation (6.79).

$$Z_0 = Z_{re} + iZ_{im} \tag{6.78}$$

$$W(L) = W_{re} + iW_{im} \tag{6.79}$$

Inserting Equation (6.78) and Equation (6.79) into Equation (6.77) yields the expression stated in Equation (6.80).

$$v = \Big(i\omega\big(Z_{re} + iZ_{im}\big)\big(\cos(\omega t) + i\sin(\omega t)\big) - i\omega\big(W_{re} + iW_{im}\big)\big(\cos(\omega t) + i\sin(\omega t)\big)\Big) \tag{6.80}$$

Equation (6.80) is expanded so the real part of the velocity can be found.

$$\begin{aligned} v =& \Big(i\omega Z_{re}\cos(\omega t) + i^2\omega Z_{im}\cos(\omega t) + i^2\omega Z_{re}\sin(\omega t) + i^3\omega Z_{im}\sin(\omega t) \Big) \\ &- \Big(i\omega W_{re}\cos(\omega t) + i^2\omega W_{im}\cos(\omega t) + i^2\omega W_{re}\sin(\omega t) + i^3\omega W_{im}\sin(\omega t) \Big) \end{aligned} \tag{6.81}$$

The real part of Equation (6.81) is stated in Equation (6.82).

$$v = \omega W_{im}\cos(\omega t) + \omega W_{re}\sin(\omega t) - \omega Z_{im}\cos(\omega t) - \omega Z_{re}\sin(\omega t) \tag{6.82}$$

To get the energy dissipated, Equation (6.74) is integrated on both sides of the equal sign and the velocity stated in Equation (6.82) is inserted as well. This yields Equation (6.83).

$$W_d = \int_0^{\frac{2\pi}{\omega}} c\Big(\omega W_{im}\cos(\omega t) + \omega W_{re}\sin(\omega t) - \omega Z_{im}\cos(\omega t) - \omega Z_{re}\sin(\omega t)\Big)^2 \,\mathrm{d}t \tag{6.83}$$

where:

ΔW_d | Dissipated energy, [J]

The constants inside the integral in Equation (6.83) is moved outside to simplify the expression.

$$W_d = c\omega^2 \int_0^{\frac{2\pi}{\omega}} \Big(W_{im}\cos(\omega t) + W_{re}\sin(\omega t) - Z_{im}\cos(\omega t) - Z_{re}\sin(\omega t)\Big)^2 \,\mathrm{d}t \tag{6.84}$$

Solving the integral leads to Equation (6.84).

$$W_d = c\omega\pi\big(W_{im}^2 + W_{re}^2 + Z_{im}^2 + Z_{re}^2 - 2W_{im}Z_{im} - 2W_{re}Z_{re}\big) \tag{6.85}$$

Equation (6.85) can be simplified to Equation (6.86) and ω is rewritten to be expressed in Hz.

$$W_d = c\,(f2\pi)\,\pi\Big(\big(W_{im} - Z_{im}\big)^2 + \big(Z_{re} - W_{re}\big)^2\Big) \tag{6.86}$$

From Equation (6.86) it is seen that the term in the parenthesis' is always positive because of the terms are squared. This ensures that the system only dissipate energy and do not add energy to the system. Why it is expected to be a valid solution of the energy dissipated.

6.4.2 Kinetic energy in the system

During this section the energy in the system is derived. The total energy in the system can be found from the maximum potential or the maximum kinetic energy as they are approximately equal for small damping coefficients [Rao, 2011], in this project the energy is found from the kinetic energy. The kinetic energy for the Timoshenko beam is stated in Equation (E.4), but is restated in Equation (6.87).

$$T = \frac{1}{2}\int_0^L \rho A_c \dot{w}^2 \,\mathrm{d}x + \frac{1}{2}\int_0^L \rho I \dot{\psi}^2 \,\mathrm{d}x + \frac{1}{2}m\dot{z}^2 \tag{6.87}$$

The expression for the displacement and angle displacement is stated in Equation (E.20) and Equation (E.21) respectively but the shortened version is inserted in to (6.87), as shown in Equation (6.88).

$$T = \frac{1}{2}\int_0^L \rho A_c \left|i\omega W(x)\,\mathrm{e}^{i\omega t}\right|^2 \,\mathrm{d}x + \frac{1}{2}\int_0^L \rho I \left|i\omega \Psi(x)\,\mathrm{e}^{i\omega t}\right|^2 \,\mathrm{d}x + \frac{1}{2}m\left|i\omega Z_0\,\mathrm{e}^{i\omega t}\right|^2 \tag{6.88}$$

The expression in Equation (6.89) is found inside the first integral of Equation (6.88).

$$\left|i\omega W(x)\,\mathrm{e}^{i\omega t}\right|^2 \tag{6.89}$$

Equation (6.89) is solved using complex conjugates, as stated in Equation (6.90).

$$\left(i\omega W(x)\,\mathrm{e}^{i\omega t}\right)\left((-i\omega)W^*(x)\,\mathrm{e}^{-i\omega t}\right) \tag{6.90}$$

The term of the deflection, $W(x)$, is also found to be complex when a damper is added to the analytical model. Thus $W(x)$ and $W^*(x)$ is expanded to contain a real and a complex part, as seen in Equation (6.91) and Equation (6.92).

$$W(x) = W_{re} + i\,W_{im} \tag{6.91}$$
$$W^*(x) = W_{re} - i\,W_{im} \tag{6.92}$$

By inserting Equation (6.91) and Equation (6.92) into Equation (6.90), it is possible to simplify the expression by using complex conjugates. The results is stated in Equation (6.93).

$$\left(W_{re}^2 + W_{im}^2\right)\omega^2 \tag{6.93}$$

The same procedure is carried out for the two other complex terms of Equation (6.88) and the results is stated in Equation (6.94) and Equation (6.95).

$$\left(\Psi_{re}^2 + \Psi_{im}^2\right)\omega^2 \tag{6.94}$$
$$\left(Z_{re}^2 + Z_{im}^2\right)\omega^2 \tag{6.95}$$

By inserting Equation (6.93) to Equation (6.95) into Equation (6.88) yields Equation (6.96) and ω is rewritten to be expressed in Hz.

$$\begin{aligned} T = \frac{1}{2}\int_0^L \rho A_c \left(W_{re}^2 + W_{im}^2\right)(f2\pi)^2 \,\mathrm{d}x + \frac{1}{2}\int_0^L \rho I \left(\Psi_{re}^2 + \Psi_{im}^2\right)(f2\pi)^2 \,\mathrm{d}x \\ + \frac{1}{2}m\left(Z_{re}^2 + Z_{im}^2\right)(f2\pi)^2 \end{aligned} \tag{6.96}$$

As W_{re} is the real part of Equation (6.67) and W_{im} is the complex part of Equation (6.67), the first integral in Equation (6.96) expands to a very long expression, thus it is not stated here, but can be seen by running the MATLAB script attached on the Appendix CD[4].

---

[4] Appendix CD\MATLAB \Analytical\KineticEnergy.m

6.5 Analytical model solutions

The analytical model established and verified in the previous sections is utillized during this section and the Timoshenko model is solved for two different purposes. The first is with the intention of finding how much energy is transferred from the bolt to the structure and in the case of the analytical model it is from the mass to the beam. The second purpose is to find the ratio of the amplitude between the bolt and the surface of the structure as investigated in Section 5.3. In this case of the analytical model its the amplitude at the beam tip and the mass. The two investigations is carried out in Section 6.5.1 and Section 6.5.2.

In Section 5.1 the resonant frequency of the test rig structure is found by FE modeling. The results showed that the first transverse resonant frequency was at a frequency of 17095Hz for the M12 structure. Hence it is necessary to increase the stiffness of the beam in the analytical model to approximately the same transverse response, to avoid the behavior observed in Appendix D.3 where two close frequencies push each other away. The stiffness of a beam, that is 0.2m long and have a circular cross section with a diameter of 0.06m, is found to 50000GPa in order to reach a transverse resonantfrequency of 16422Hz.

The stiffness of the spring in the analytical model is found based on solving Equation (D.3) with respect to k and is stated in Equation (6.97). As the frequency is known from test and FE results, and the mass is found by weighing the bolt with transducer and washer. The M12 bolt, washer, and transducer is found to weigh $0.201kg$ and the bolts first transverse resonant frequency is 3040Hz.

$$k = 4\pi^2\omega^2 m \tag{6.97}$$

The first transverse mode of the bolt is found by using Equation (6.97) and the stiffness of the bolt is found to be $73.34\frac{GN}{m}$. All the parameters used is stated in Table 6.3

Model parameters			
E	$50000GPa$	ρ	$7800\frac{kg}{m^3}$
L	$0.2m$	d	$0.06m$
m	$0.5kg$	k	$73.34\frac{GN}{m}$
ν	0.3	G	$\frac{E}{(2(1+\nu))}$
κ	$\frac{6(1+\nu)}{7+6\nu} = 0.9$	F_0	$100N$

Table 6.3 Input parameters for the analytical model for verifying the spring/mass part of the model.

6.5.1 Transmission of energy

During this section the analytical model is evaluated to find how much energy is transferred from the mass to the beam. The analytical model is solved for frequencies from 0 to 6400Hz with a step size of 8Hz. The model is solved, and the dissipated energy is found, and the total energy in the system is calculated for each frequency in order to see how much influence the damper has on the system at different frequencies. The damping constants used during evaluation of the transmission of energy is 20 to $100\frac{Ns}{m}$ with intervals of $20\frac{Ns}{m}$. If the damping constants is used in Equation (6.70) and Equation (6.71), the damping ratio is found to be between 0.26% to 1.3%. As the real test structure is damped by friction forces it is necessary to add small values of viscous damping. Thus it is considered acceptable to have a damping ratio of 1.3%. The MATLAB script for the Timoshenko model, used for transmission of energy, is attached on the Appendix CD[5]

---

[5] Appendix CD\MATLAB \Analytical\TimoshenkoModel.m

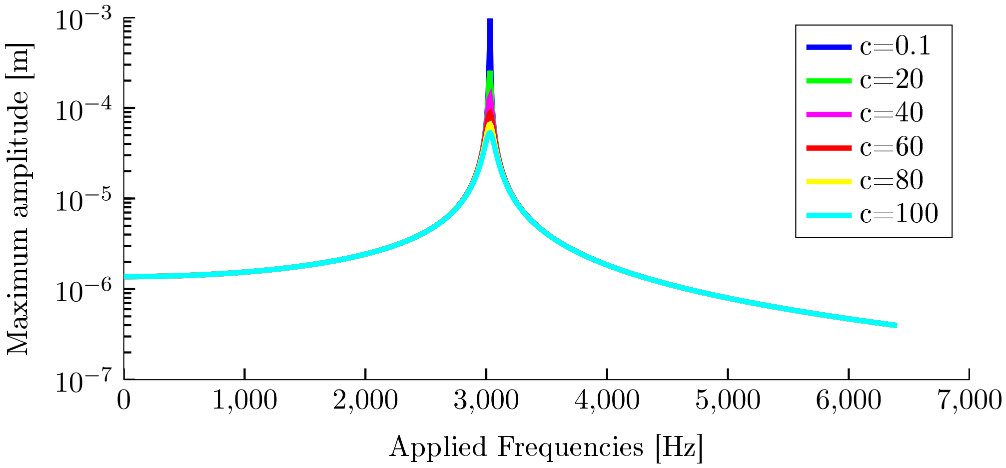

Figure 6.8 Response of the analytcal model for various damping.

In order to see the response on Figure 6.8 more clearly the figure is plotted again where the x-axis is scaled from 2950Hz to 3100Hz as shown in Figure 6.9.

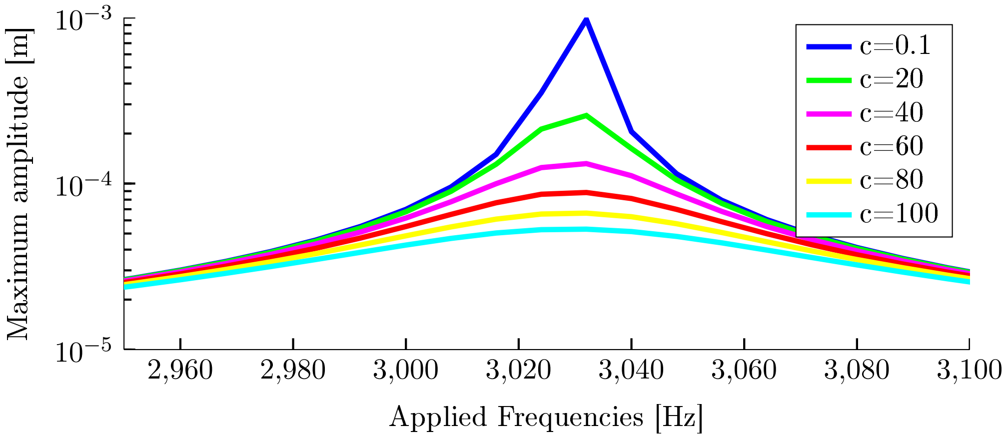

Figure 6.9 Close up of the resonance peak to clearly see the influence of the damping.

In Figure 6.9 it is clearly seen how the damping influences the peak of the of the resonant frequency. Thus it is interesting to see how the specific damping capacity changes, in order to investigate if there is any abnormalities due to the damper. The specific damping capacity is shown in Figure 6.10.

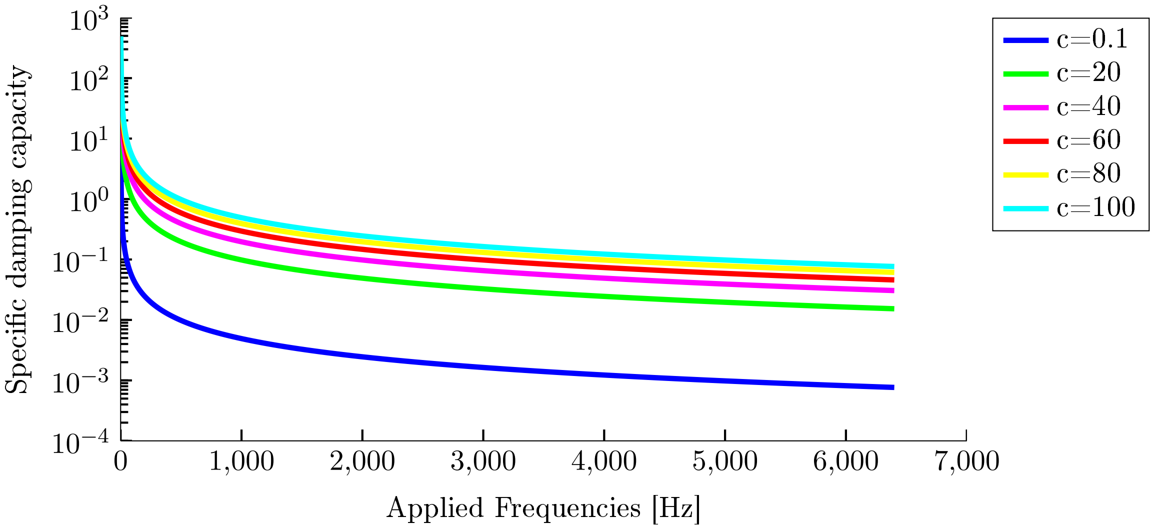

Figure 6.10 Specific damping capacity for the analytical model.

From Figure 6.10 it is seen that the specific damping capacity increases along with increased damping constant, which is to be expected. As the numerator of Equation (6.73) increases and the denominator decreases. In order to tell how much energy is transferred from the mass to the beam. In order to do so the total energy of the system used in Equation (6.73) is reduced to the kinetic energy of the beam. The result is stated in Figure 6.11.

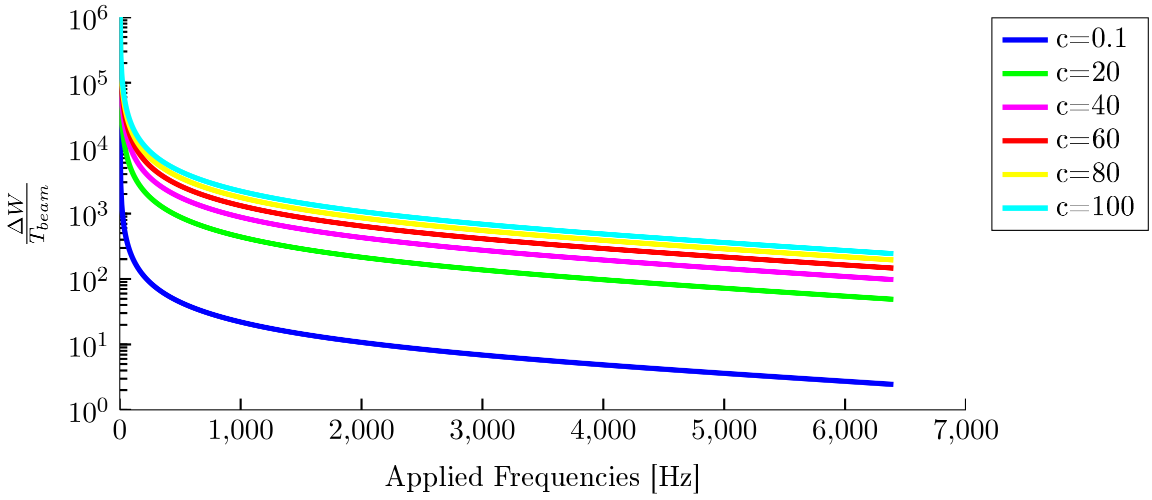

Figure 6.11 Dissipated energy by the damper divided by the kinetic energy of the beam.

By comparing Figure 6.11 to Figure 6.10, the shape looks the same, but by comparing the scale of the y-axis on the figures it is clearly seen that they are not identical. Hence it can be concluded that the most of the kinetic energy is located in the mass and that there is not much energy transferred to the beam. Thus it is assumed that a lot of energy is lost in the real test structure due to friction between the bolt and test structure.

6.5.2 Amplitude ratio

During the FE study it is discovered, that the motion of the bolt and structure are in sync but the amplitude is very different. Thus it is investigated if the same behavior can be observed in the analytical model. For the initial response the paramters in Table 6.3 is used and the model is solved for the same frequency range as the FE study, which is from 2500Hz to 3500Hz with a interval of 8Hz. The response of the beam and mass without any damping is seen in Figure 6.12. From which it is seen that the peaks of the beam and mass are identical as discovered in the FE study. The MATLAB script for the Timoshenko model, used for the amplitude ratio, is attached on the Appendix CD[6]

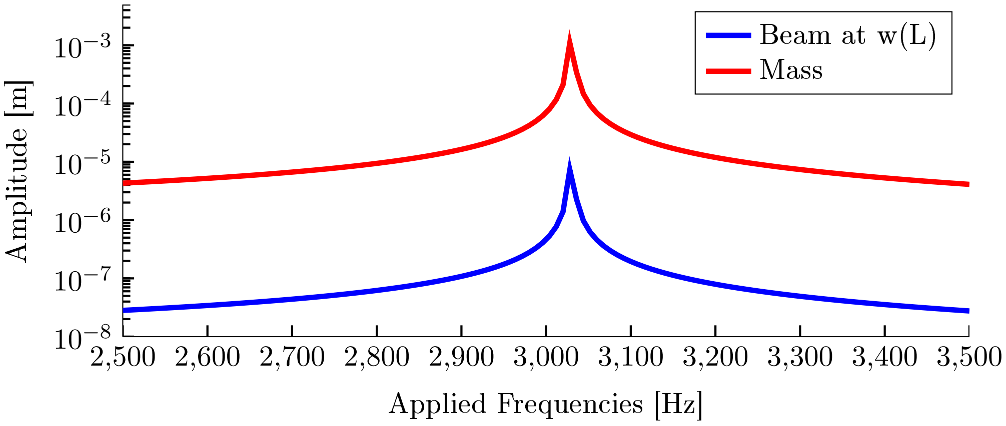

Figure 6.12 Response of the beam and mass.

---

[6] Appendix CD\MATLAB \Analytical\TimoshenkoAmp.m

In order to obtain the amplitude ratio, the beam deflection is divided by the mass deflection and the amplitude ratio is displayed in Figure 6.13.

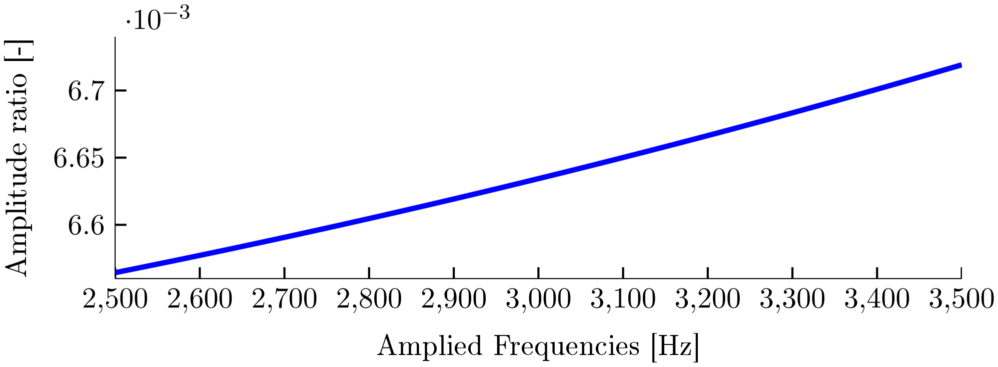

Figure 6.13 Amplitude ratio found by the analytical model, with the parameters from Table 6.3.

By comparing Figure 6.13 to Figure 5.21, it is obvious that the shape of the analytical amplitude ratio is not identical to the one found be the harmonic FE study. The ratio in the analytical model is also five times smaller than the harmonic study. The ratio from the analytical model being so low indicates that the beam is too stiff.

In order to study the influence of the damper on the amplitude ratio, the analytical model is fitted to have the same amplitude ratio as the FE model. This can be done in multiple ways and to get the best result and optimization should be made. In order to simplify the fitting of the model it is chosen to change the stiffness of the beam and spring. Other options could be changing the length of the beam or the cross sectional area of the beam.

The model yields comparable results when the beam stiffness is 14GPa and the spring constant is increased to $80\frac{GN}{m}$. All other parameters that is not dependent on the modulus of elasticity is kept the same. The response obtained from the new parameters is stated in Figure 6.14 when no damping is added to the model.

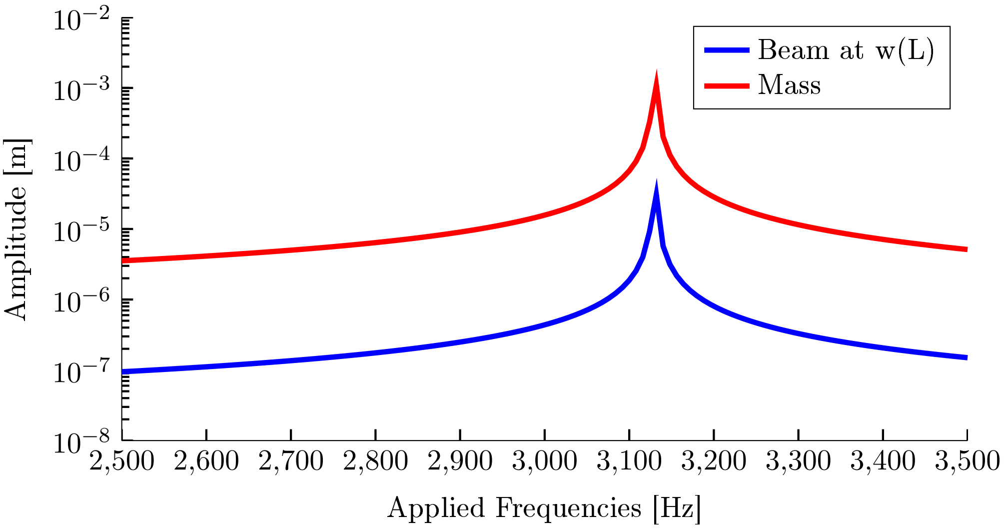

Figure 6.14 The fitted response of the beam and mass.

The repsonse of the analytical model is now similar to the FE model and the amplitude ratio is stated in Figure 6.15. Where it is seen that the shape from the FE model can not be reproduced but the level of the amplitude ratio is matched.

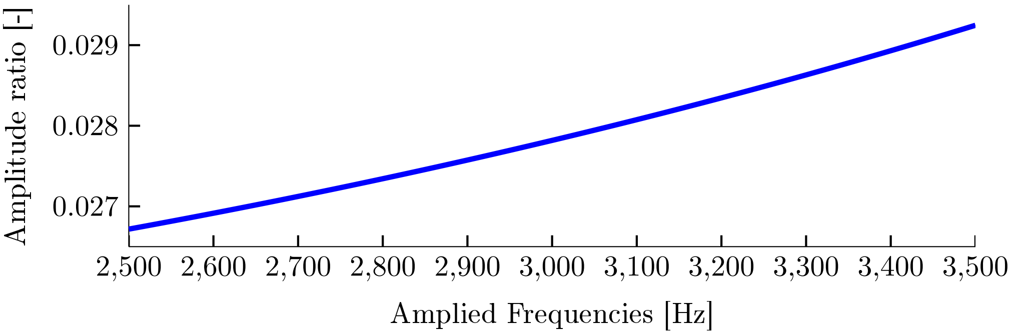

Figure 6.15 Amplitude ratio found by the analytical model, with the fitted parameters.

By adding a damper to the system to se how the amplitude ratio shown in Figure 6.15 is affected, the response is changed but the amount is not known. Thus the model is calculated for different damping levels from 0.1 to 100$\frac{Ns}{m}$ with a step size of 20$\frac{Ns}{m}$. The results is stated in Figure 6.16. Where it is seen that the amplitude ratio is affected very little by the damping as the curves in Figure 6.16 are practically on top of each other.

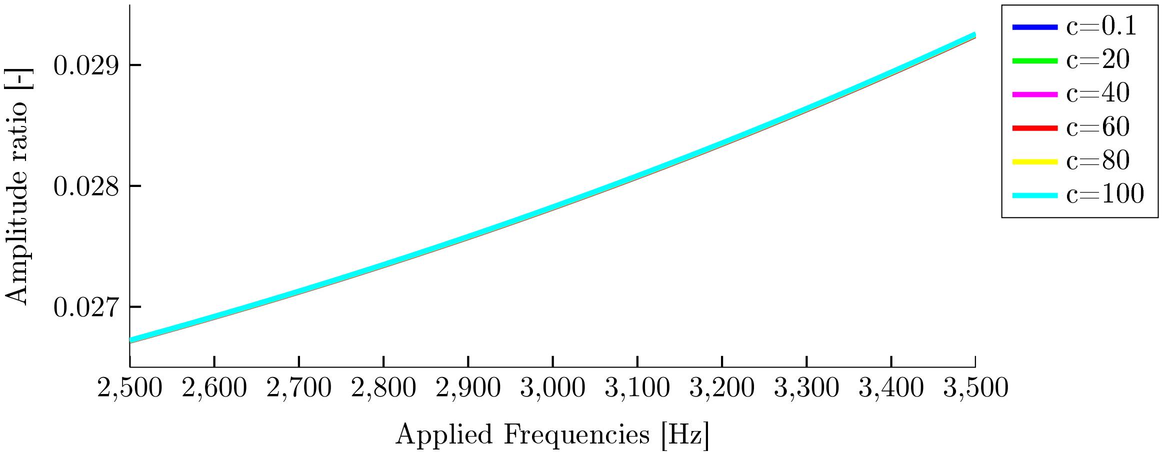

Figure 6.16 Amplitude ratio when damping is added.

The damping do not contribute to the amplitude ratio and it is concluded that the FE models created without damping is sufficient accurate as the damping do not influence the response significantly.

6.6 Eigenfrequency of the test structure

The analytical model is made as comparison to the FE model and test results. In order to verify the FE model of the test rig stated in Section 5.1, where FE results state that the first mode of the structure is torsional, an analytical solution is sought both for the torsional eigenfrequency and the transverse eigenfreqyency. This section will only explain how the transverse solutions is found.

The elastic bands supporting the test rig is considered so compliant that the support is very close to a beam applied with no support, thus a free-free boundary condition, as indicated by the results in Section 5.3. During this section the modal response of the test rig is found when the test rig when applied to the free-free boundary conditions. The parameters of the beam are given in Table 6.4.

Model parameters			
E	$200GPa$	ρ	$7800\frac{kg}{m^3}$
L	$0.1m$	d	$0.06m$
ν	0.3	G	$\frac{E}{(2(1+\nu))}$
κ	$\frac{6(1+\nu)}{7+6\nu}=0.9$		

Table 6.4 Parameters of the test rig.

The eigenfrequencies are found by stating the boundary conditions in a matrix form. Thus the boundary conditions of a free-free Timoshenko beam is stated in Equation (6.98) to Equation (6.101).

$$\Psi'(0)=0 \tag{6.98}$$

$$\Psi'(L)=0 \tag{6.99}$$

$$W'(0)-\Psi(0)=0 \tag{6.100}$$

$$W'(L)-\Psi(L)=0 \tag{6.101}$$

The moment and shear force at each end must be zero ind order to allow the beam to move freely. The expression for the deflection and angular displacement are found in Equation (6.67) and Equation (6.68) respectively. By inserting Equation (6.67) and Equation (6.68) into Equation (6.98) to Equation (6.101) whereby the boundary conditions can be stated in a matrix form sorted by the unknown constants A_i for $i = 1..4$. The matrix is from now on called the BC-matrix. The BC-matrix is stated in Equation (E.70). The transverse eigenfrequencies are found as the eigenvalue problem of the BC-matrix.

When using Timoshenko beam theory to calculate the eigenfrequency it is important to know the limitation of the method. In this case the limitation is a cut-on value of the frequency, where upon a solution is no longer sufficiently accurate [Stephen and Puchegger, 2006]. The cut-on value can be calculated by Equation (6.102), which is found by letting $\lambda = 0$ in Equation (E.29) and solving for ω.

When the calculation of the determinant of the BC-matrix reaches the cut-on value, the values of λ_i for $i = 1, 2$, that is included in the equations of displacement and angle displacement, changes. Fx. λ_2 stated in Equation (E.32) goes from only containing a real part to only be imaginary, thus the expressions of displacement and angle displacement is no longer valid.

$$f_{co}=\frac{\sqrt{\frac{\kappa AG}{\rho I}}}{2\pi} \tag{6.102}$$

where: [Stephen and Puchegger, 2006]

f_{co} | Cut on frequency for Timoshenko beam, [Hz]

For the steel test rig the cut-on frequency is calculated to be $31370.1Hz$ by using Equation (6.102). This is verified by calculating the determinant of the BC-matrix where no solution above $31370Hz$ can be obtained. Thus the cut-on value is found and the non-trivial solutions are found for discretized frequencies from 0Hz to 30kHz with intervals of 5Hz. The results from 0Hz to 28kHz is shown in Figure 6.17 as values above 28kHz only disturbs the visualization. Where the blue line is the determinant of the BC-matrix and the black indicating zero.

From Figure 6.17 it is seen that it is possible to obtain the two first transeverse eigenfrequencies as the determinant of the BC-matrix crosses zero two times. The eigenfrequencies are found to $16818Hz$ and $27721Hz$. The MATLAB script for the eigenfrequency of the test rig is attached on the Appendix CD[7].

---

[7] Appendix CD\MATLAB \Analytical\EigenfrequencyFreeFree.m

As the eigenfrequencies of the test rig is significantly larger compared to those found from the bolts the test rig is considered not to influence the response obtained during test and thus it is not expected to have any effect on the bolts as seen in Section E.2.3 when the frequencies of the beam and mass are located close to each other.

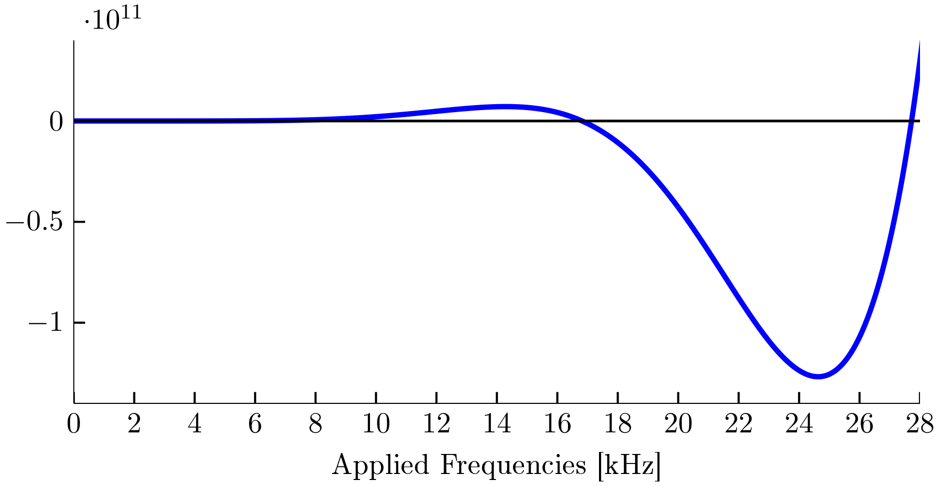

Figure 6.17 Non-Trivial solutions is found when the plot crosses the x-axis.

6.7 Summary

During this chapter, the analytical model is evaluated and results are compared to the FE results obtained in Chapter 5. Initially the model is stated by Bernoulli-Euler theory but is later expanded to Timoshenko beam theory. The FE model results states that the first resonant frequency is a torsional mode and the second mode is transverse, in order to verify the results, an analytical result is found. Hence the expansion to Timoshenko beam theory. The Timoshenko model is also used in all the results obtained during this chapter, as the beam is short to be comparable to the test rig.

The analytical model is used to estimate how much dampening influences the structure. From the investigation of the amplitude ratio in Section 6.5.2, it is proved that the dampening of the structure has very little influence on the response. Thus the results obtained by FEM is considered as valid.

The energy in the system is evaluated aswell and it is discovered that very little of the energy applied to the mass or bolt is transferred to the structure surface or the beam. This explains why it is necessary to use the most sensitive accelerometers during experiments. Furthermore it is also proved by the analytical model that most of the energy is located in the mass, as stated in Section 6.5.1.

From the verification of the combined model, stated in Appendix Section D.3, it was discovered that when two systems, with resonant frequencies of similar magnitude, are combined, the resonance frequencies are pushed away from each other. In contrast nothing happens when the resonance frequencies of the spring/mass and the beam is far away from each other. Thus it is believed that it is possible to learn more from the analytical model if the resonance frequencies is closer to each other. As the spring/mass and beam will interact more as more energy is transferred to the beam.

The model is considered to be too simple to predict the response of the test rig and is only created to imitate the response to get knowledge about the damping and acoustical response. It would be impossible to predict the response of fx. a M36 bolt in a structure with out support from any FE model or test results. Even if data is available it is seen that the model does only reveal useful data about the transmission of energy. So to obtain better results the model should be expanded so the beam has a fully elastic support along the length of the beam or even to calculate the problem as a Rayleigh surface wave.

Results summary and discussion 7

In this chapter, the results of the work carried out in the project, are evaluated and the perspectives of using acoustical measurements for determining bolt pretension are discussed. Initially the results of the project are presented and important conclusions are discussed. Then as most of the project is based on vibrations, some considerations regarding acoustic emission and measurements are presented. Subsequently the shortcomings of the project are presented, to give an overview of some of the more important aspects that still need to be covered, in order to have sufficiently covered the topic, with respect to using it for practical applications. These are covered very briefly as they will be elaborated upon in Chapter 9. Finally a suggestion as to how the work done in this project, can be used in practice is presented.

7.1 Results

In this project it has been sought to determine, whether it is possible to use acoustical measurements, based on excitation by an impact hammer, to determine the degree of pretension in bolts in a structure. The reason for investigating this, is that when comparing the response of a correctly pretensioned bolt, to that of a loosely tightened bolt, excited by an impact hammer, an audible difference can be observed. This has led Brüel & Kjær to suggest, that it might be possible to develop a practical method for determining whether a bolt is correctly tensioned, using acoustical measurements. To examine whether this is possible, the underlying mechanism that controls the acoustical response has been investigated. The goal of this investigation was to determine, what aspects of the response are usable with regards to determining the degree of pretension, and if it would be feasible to use any of these features in practice.

The investigation has been performed with focus on three sizes of pretensioned bolts, M12, M18, and M24, all with a length of 140mm. Each bolt size has been examined for different levels of pretension, in a simple structure containing only a single bolt. This setup has been tested experimentally, and subsequently modeled with both FEM and an analytical model, to investigate the transmission from the impact to acoustical emission. Most of the experiments have been performed, and all modeling has been carried out, for a steel structure. For the initial experiments on the M12 bolts however, an aluminum structure was also tested. Here the same behavior was seen, but the response was not as clear as for the steel structure, which is why the aluminum structure has not been evaluated further.

Through the performed experiments, it was found that a clear movement of the resonant frequencies could be observed, when the tension in the bolt was increased. The frequency increase observed was so substantial, that an increase in stiffness of 12.7% would be required to explain this rise, solely by the stiffness of the system. This is seen as unlikely and instead, the hypothesis that changing boundary conditions cause resonances to shift, was examined. It was found that by modeling the system with FEM, and implementing a hinged and a clamped boundary between the bolt and the surrounding structure, the same response as seen in the experiments was obtained. In Table 7.1 the maximum and minimum frequency of each mode is seen, as well as the corresponding hinged, and clamped solution from the FE model. Missing numbers indicate that no or limited response was found in the expected region of resonances.

		Experiments			**Full FE model**		
Bolt	Mode	Min	Max	Δ	Hinged	Clamped	Δ
M12	f_1 [Hz]	2928	3040	112	3015	3144	129
	f_2 [Hz]	-	-	-	7897	8178	281
	f_3 [Hz]	10200	10432	232	10200	10487	287
M18	f_1 [Hz]	3912	4032	120	4167	4415	248
	f_2 [Hz]	9456	9904	448	9984	10300	316
	f_3 [Hz]	10440	10744	304	10611	11151	540
M24	f_1 [Hz]	-	-	-	5066	5449	383
	f_2 [Hz]	9440	9608	168	9359	9762	403
	f_3 [Hz]	-	-	-	11426	12007	581

Table 7.1 Responses found experimentally compared to those found with the FE model.

As it can be seen from Table 7.1, the response obtained in the experiments and from the FE model are very similar, although the experimental results are are slightly lower. This verifies the hypothesis that the change in boundary conditions are the cause of the change in resonant frequencies of the structure. Furthermore, it can be seen that the gap in frequencies, between the two boundary conditions, increases for larger sizes of bolts, although the modeled gap seems to increase more. This indicates that in the physical system, the loose connection is more than hinged, and that the tightened connection is less than clamped, which seems reasonable. The only mode that does not seem to follow this behavior, is the second mode for the M18 system, here the experiments show a larger gap. Looking at the results for the peak movement under changing pretension, as given in Table 4.3, it can be seen that going from 80% pretension to 90% pretension, gives a large increase in resonant frequency of the mode, which is inconsistent with the movement seen for the rest of the pretension range. Looking at the third mode for the M18 system, a large jump is also seen at 90% pretension, and for the first mode there i no obtained response at this level of pretension, which indicates that there could be an error with the 90% measurement of the M18 system. If the response under 80% pretension is chosen as the maximum resonant frequency, the gap for the second mode of the M18 system matches in the rest of Table 7.1.

In relation to the table, it should be noted that the minimum value used for the M12 results, are not for 10% pretension, but rather 40% as it seem that lower pretension does not provide enough clamping force for the bolt to be considered hinged. In relation to this, it is generally seen from the results that for larger clamping force, that is either higher pretension or larger bolts, the increase between the different levels of pretension is more consistent. This implies that it could be easier to accurately determine the level of pretension, for higher levels pretension, which is an important feature of the behavior. This implies that it would be easier to distinguish whether a bolt is tightened to 85% or 90%, than if it is 20% or 25%, which is desirable as bolts that needs to be checked for correct pretension, typically are in the 70% to 90% pretension range.

The missing signals for the second mode for the M12 system, as well as the two missing mode responses for the M24 system, has been investigated. For the third mode of the M24 system, the reason for the missing signal is simply that the mode is torsional, and thus does not produce any measurable response in the direction of the accelerometer. To investigate the two other modes, a Harmonic FE analysis has been performed. From this analysis the response of the system under a constant load at the location of the accelerometer was obtained, and movement of the bolt and structure surface was compared. Based on this it could be seen that, the second mode of the M12 system had the least surface movement at the point where the accelerometer was placed, but did however not explain the missing signal as the amplitude for the third mode was approximately the same. To explain this it was examined whether a change in the forcing conditions, makes a significant change in the response. It was found that by changing the load application, the response of the structure at each mode was changed differently, which is likely due to the modal participation factor of the system. This was also found to explain the missing response at the first mode for the M24 system.

Another thing that was found through the harmonic analysis, was that there is a significant difference in the amplitude of vibration between the bolt and the structure, which implies that much of the energy that is put into the system is not transferred to the structure, but remains in the bolt where it is dissipated. To examine this, an analytical model has been established, based on a beam and a simple spring mass damper model, where the beam describes the motion of the structure surface, the mass describes the bolt, and the spring and damper describes the transmission between the two. Using this model it was found that most of the energy that is put into the system, remains at the mass, which is consistent with the results of the harmonic FE analysis, which indicates poor transmission of energy between the two components. It should be noted that this has only been investigated for the M12 system, for the M18 and M24 the results of the harmonic analysis suggests, that with increased bolt size the transmission improves. However, as the way the harmonic analysis is evaluated with respect with transmission, is by the movement of the two components with respect to each other, and not by the amount of energy transferred, its reliability as an indication of transmission is limited. Especially due to the fact that an increase in bolt diameter leads to a decrease in the thickness of the cylinder wall in the structure, thus making the bolt stiffer and the structure more compliant. In relation to the transfer between the bolt and structure, it should also be noted that a series of experiments were performed, to determine whether the size of the washer between the bolt and structure, had any influence on the obtained response. It was found that there was no significant change in the response, and by inspecting the washers used for the experiments, it was found that the area of the washer which is in contact with the bolt and structure, was unchanged for different washer sizes.

Through the results obtained in the analytical model, it was also found that the damping present in the system has a limited influence, especially with regards to the transfer between the two parts of the system. Furthermore, in the experiments on the M12 structure, the damping was found to be quite low, and relatively stable, when a certain level of pretension is reached. Thus the considerations with regard to damping are seen as negligible en relation to determining pretension in bolts.

Summing up on the results of the project, the mechanism that controls the change in resonant frequencies for different levels of pretension, has been identified as a change in boundary conditions. The change is so significant that it should be possible to use it for determining whether a bolt is tightened correctly. To do so however it is important that the bolt is excited in such a way that sufficient acoustical emission can be attained.

7.2 Acoustical considerations

Even though the scope of this project is to establish, if is possible to acoustically determine bolt pretension, most of the work is based on vibrations. However, as acoustic emissions are based on the vibration of surfaces, the results obtained for vibrational response should be applicable to microphone measurements. The main problem will be, to get a response that is large enough to avoid background noise interfering with the measurements. This will require that, the bolt is hit in such a way that brings out the largest amplitude possible for the desired mode, and that the microphone is positioned near the surface having the largest amplitude of vibration. This of course requires that the response, of the bolt and the structure is placed in, as well as the optimum hitting point, is known. This limits the use of the technique to testing well known structures, likely ones that are produced in larger numbers or ones that require regular inspection. A wind turbine foundation would be a good example, requiring both regular maintenance and being built in large numbers for a given model.

7.3 Shortcomings

The goal of this project is, to determine whether it is feasible to use acoustical measurements, to determine the pretension of bolts in a structure. While it seem possible, based on the work done in the project, it is still necessary to investigate some aspects of the problem, to be able to say for certain, if it is practically applicable. These will be briefly described here, but are treated more thoroughly in Chapter 9.

Most importantly, it is necessary to determine if an untightened bolt, can be identified in a structure containing several bolts. From the results obtained in Chapter 2, with regards to the structure containing four bolts, it should be possible to distinguish the bolts in a structure where several are present. In relation to this, it should also be examined how precisely it is possible to determine the degree of pretension. It is also necessary to test whether the response found for the simple structure, can be seen for more advanced structures, as well as for larger sizes of bolts. This also includes looking at what happens when the system is coupled more strongly, e.g. the resonant frequencies of the bolts being close to those of the structure, as discussed briefly in Chapter 6. Furthermore, the influence of changing the length of bolts should be investigated.

Given that an investigation of these aspects, yields the results expected based on the work of this project, it should be possible to establish a practical method of acoustically determining the level of pretension in bolts, for a well known structure.

7.4 Practical application

In this section the practical application of measuring pretension acoustically, is treated. It is assumed that the shortcomings described previously, have been treated and that they yielded similar results, to those obtained for the response of the simple structure used in the project.

In Figure 7.1 an example of how the bolts in an arbitrary flange, are expected to respond, when each bolt is hit one by one. The idea is that, by measuring the acoustic emission at the marked points, it is possible to pinpoint the bolt which is not tightened sufficiently. Going from left to right on the bolts in the figure, it is seen that initially only the response of the 90% tensioned bolts are measurable acoustically. Then the closer the bolt being hit, is to the less tightened bolt, the more the FRF is influenced by the resonances of the less tightened bolt. Thus the response is expected to be larger at the frequency of the less tightened bolt's mode, compared to that of the correctly tightened bolts, when it is being hit.

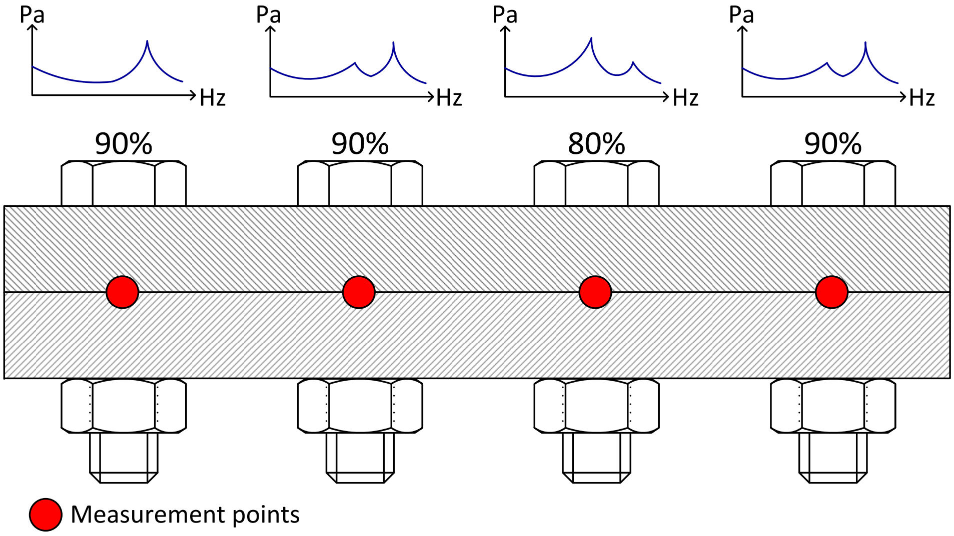

Figure 7.1 Illustration of measurements of bolts on an arbitrary flange

By setting up a frequency span of acceptable peak frequencies, it is possible to determine which bolts need to be tightened, by observing where the frequencies, outside this span are the largest. In order to be able to set up this kind of test, it is thus necessary to perform baseline measurements of the structure, when it is known to have correct pretension. Which also means that only certain kinds of structures are relevant to this type of test.

As it has been found that the movement of resonance peaks, happens at all the investigated modes, this might be utilized to make a more robust test system. By setting up an acceptable peak span, and measuring the response of the structure at several modes, the significance of the uncertainties related to these measurements can be reduced.

To be able to perform these measurements, it is of course necessary to be able to obtain a sufficiently powerful acoustical signal. As seen during the project, this requires that the bolt is excited correctly, but it might also be possible to magnify the acoustic emission of the surface of the structure in other ways. One possibility is that the investigation of strongly coupled systems, indicate that by having structural resonances close to those of the bolts, a larger movement of the structure surface will occur thus yielding larger acoustic emissions, while still exhibiting the movement of peaks with increased pretension. This would suggest that by tailoring the resonances of the structure surfaces close to the bolts, it is possible to get a better acoustic response. Another possibility is that by shaping the surface to concentrate its emissions towards a specific point, it is possible to gain a much clearer response by measuring at this point. These suggestions does of course require significant work to be put into the design of the bolted connections that are to be measured, but might be worthwhile for structures such as wind turbine towers.

Based on these suggestions it should be possible to create a system, for determining whether bolts are pretensioned correctly. It will however only be possible to do so for structures where the desired response is know, making it possible to detect deviations.

Thus suggest that it might be a good idea, to base a practical solution on some kind of database system, where each structure is tested and its response logged, when the structure is initially assembled and the pretension is known to be correct. Then on inspections, the response obtained can be compared to that which has been recorded previously, whereby it can be seen if any bolts have gotten to loose. Furthermore, to obtain the best possible results it does require that the measurement method is taken into consideration when creating the bolted connection. Once the system is up and running though, it should help save significant time on inspections, compared to the currently used methods in for example wind turbine tower foundations.

Conclusion 8

Throughout this project is has been investigated whether it is possible, ***to acoustically determine the degree of pretension of bolts***, in a bolted connection. This has been done by experiments on bolted structure, as well as FE and analytical modeling.

In Chapter 2, the response of a simple structure containing an M12 bolt was tested under different levels of pretension. It was found that ***by increasing the pretension in the bolt, the resonant frequencies of the system increases***, while the damping remains relatively constant. This was the case for both steel and aluminum structures, and independent of the size of the washer used. The increase in frequencies is quite significant, and would require an unlikely increase in the stiffness of the structure, so the hypothesis that ***a change in boundary conditions*** causes the increase was stated.

This hypothesis was examined in Chapter 3, using a FE model of an M12 bolt. To model the change in boundary conditions the bolt was fixed by a ***hinged-hinged boundary*** to model conditions of low pretension, and as a ***clamped-clamped boundary*** to model high pretension. From this model it was found that, the ***difference between the eigenfrequencies*** of the hinged and the clamped models, were very similar to the increase seen in the ***experiments on the M12 bolt system***. Based on this, the change in boundary conditions were concluded to be the cause, of the increase in the resonant frequencies observed in the experiments.

As the reason for the rise in resonant frequencies for the M12 bolt was determined, it was investigated whether this was also the case for ***other bolts***. To this end ***M18 and M24*** bolts were tested in Chapter 4, where similar results was found, indicating that this is a general tendency for bolted structures. Also from looking at all the experimental data, it was observed that ***the increase resonant frequencies, is generally stable*** in relation to increases in pretension, especially for higher pretension.

In Chapter 5, a ***FE model of the full structure***, for each bolt size, was established, in order to gain more insight into the mechanics of the tested systems. With this full system model, an even ***better correlation between the experimental and FE results was obtained***, and it was found that the rise in resonant frequencies, as a result of higher pretension, increases for larger bolt sizes. With the full model, it was also investigated how ***the bolt and structure surface moves in relation to each other***. Here it was found that there is a significant difference in the movement in the two, but that this difference was very different for different modes and bolt sizes, It was also found that the response at a given point on the structure, is highly dependent on how the forcing is applied.

In order to examine the difference of movement between the bolt and structure, ***an analytical model*** describing ***the transfer of energy from the bolt to the structure***, was established in Chapter 6. From this it was found that for a weakly coupled system, as those examined, had ***very little transfer of energy*** between the bolt and structure, and that ***damping had very little influence on this transfer***.

In conclusion it can be said that, based on the results of the project, ***it should be possible to use acoustics to determine the degree of pretension***, in the bolts of a bolted joint, or rather that it is possible to determine, whether the bolts are tightened correctly. However before it is possible to do so in practice, it is necessary to examine; bolted structures containing several bolts, structures with more complex geometry, the response for strongly coupled systems, as well as the response of relevant bolt sizes and lengths.

Future work 9

In this chapter, work that is considered to be useful, with respect to implementations of the results of the project in practice. Some of these aspects have been briefly discussed in Chapter 7, and will be elaborated upon.

Number of bolts

To determine whether it is possible to actually distinguish individual bolts in a structure, it is necessary to perform experiments on a structure containing several bolts. This could for example be on a simple flange similar to the one shown on Figure 7.1, which would determine whether the acoustical measurements can provide the desired response.

Structural complexity

The structures tested in this project are greatly simplified, compared to bolted joints in real life applications, and so the complexity should be increased, in order to determine whether similar response can be obtained from real life bolted joints. First step in increasing the complexity, is to simply split the test rig structure, tested in this project, in to two parts. This will make the structure go from being one solid structure with a bolt, to actually being a joint consisting of two parts clamped together by the bolt. If results obtained for the joined structure are comparable to those obtained in the project, then the complexity should be increased to a simple real life joint, and so on, until a sufficient level of complexity is reached for the desired application.

Bolt behavior

As only three types of bolts are tested, all with a length of 140mm, it is necessary to look at how the response changes with regards to both size and length. But more importantly it is necessary to determine what happens when the eigenfrequencies of the structure and bolt are close to each other, and can be considered a strongly coupled system, as this is expected to have a larger influence on the system response, than the response of a bolt of a particular type and length. Furthermore, in order to determine the accuracy of the acoustical measurements, it should also be tested how small a change in the response is detectable for the relevant bolts and structures.

Modeling

The analytical model that has been established in this project, is only sufficient to treat the simple system used for the project, and can only describe the energy transfer between the bolt and structure, and how the damping influences the transmission of energy. In order to improve the analytical model, it needs to describe a surface wave of the structure even better. This is done by introducing an elastic support of the beam along its entire length. Another possibility is to use the model of a Rayleigh surface wave. This should improve the usability of the model but has to be investigated further.

Bibliography

Hoffmann, 1989. Karl Hoffmann. *An Introduction to Measurements using Strain Gages*, 1989

Knudsen, 2013. Jonas Syders Knudsen. *Vibration-based Testing of Bolt Tightening*. Technical University of Denmark (DTU), 2013

Mouritsen, 2010. Ole Mouritsen. *Grundlaeggen usikkerhedsvurdering ved maaling med strain gages*. Department of Mechanical and Manufacturing Engineering, Aalborg University, 2010

Norton, 2006. Robert L. Norton. *Machine Design - An integrated approach*, 3rd edition, 2006

Rao, 2011. Singiresu S. Rao. *Mechanical Vibrations*, 5th edition, 2011

Rust Bullet, 2014. Rust Bullet. *Turbine projects*. Rust Bullet, 2014. http://www.rustbullet.com/Uploads/Turbine%20Project/BoltsRB.jpg (Accessed 2010-10-10)

Shames and Cozzarelli, 1992. Irving H. Shames and Francis A. Cozzarelli. *Elastic and inelastic stress analysis*, 1992

Stephen and Puchegger, 2006. N. G. Stephen and S. Puchegger. *On the valid frequency range of Timoshenko beam theory*. University of Southampton, 2006

Tokyo Sokki Kenkyujo Co., Ltd., 2012. Tokyo Sokki Kenkyujo Co., Ltd. *Precise & flexible strain gauges*, 2012. Datasheet for strain gauges http://www.tml.jp/e/download/catalogdownload.html (Accessed 2014-02-10)

Pretensioning bolts

A

In the project the pretension of bolts is of a major importance, therefore this appendix is included to describe how the pretension of the bolts is calculated, achieved and controlled.

The pretension of a bolt, is the tension in the bolt compared to its proof strength, given as a percentage. From the tension in the bolt the clamping force exerted by the bolt can be calculated by Equation (A.1).

$$F_{pt} = S_p \cdot P_t \cdot A_b \tag{A.1}$$

where:

F_{pt}	Clamping force exerted by the pretension, [N]
S_p	Proof strength of bolt, [MPa]
P_t	Prestress in the bolt in percent, [-]
A_b	Cross sectional area of the bolt, $\left[mm^2\right]$

The proof strength of a class 8.8 bolt is 600MPa, in Table A.1 the clamping force at different levels of pretension can be seen for M12, M18, and M26 bolts of class 8.8.

	10%	20%	30%	40%	50%	60%	70%	80%	90%
M12	6.8kN	13.6kN	20.4kN	27.1kN	33.9kN	40.7kN	47.5kN	54.3kN	61.1kN
M18	15.3kN	30.5kN	45.8kN	61.1kN	76.3kN	91.6kN	106.9kN	122.1kN	137.4kN
M24	27.1kN	54.3kN	81.4kN	108.6kN	135.7kN	162.9kN	190kN	217.1kN	244.3kN

Table A.1 Clamping force for pretensioned M10 and M12 bolts.

From the clamping force it is possible to calculate the torque required required to achieve the corresponding level of pretension, by Equation (A.2). The equation is only valid for lubricated bolts with standard threads. [Norton, 2006]

$$T_{cf} = 0.21 \cdot F_{pt} \cdot d_b \tag{A.2}$$

where: [Norton, 2006]

T_{cf}	Torque required for the desired clamping force, [Nm]
d_b	Diameter of bolt, [mm]

In Table A.2 the required torque for different levels of pretension can be seen.

	10%	20%	30%	40%	50%	60%	70%	80%	90%
M12	17Nm	34Nm	51Nm	68Nm	86Nm	103Nm	120Nm	137Nm	154Nm
M18	58Nm	115Nm	173Nm	231Nm	289Nm	346Nm	404Nm	462Nm	519Nm
M24	137Nm	274Nm	410Nm	547Nm	684Nm	821Nm	958Nm	1094Nm	1231Nm

Table A.2 Required force for different level of pretension.

The torque applied by a torque wrench, which is what is available in the workshop, is however not that precise, having a variation of ±30% [Norton, 2006]. Therefore a method of verifying the pretension is desired, to accomplish this a force transducer is used to measure the clamping force.

A.1 Transducer

This appendix describes how a load transducer is made and which components are used during the manufacturing and lastly the load transducers accuracy is estimated followed by a calibration. A load transducer is manufactured as there are no suitable load transducers available at institute of Mechanical and Manufacturing Engineering. Furthermore it is cheaper and faster to manufacture a transducer than to purchase the required type. As strain gauges are available at the institute laboratory.

A.1.1 Transducer manufacturing

The transducers are made to determine the pretension of the bolts more accurately than with a torque wrench. The basic idea is to extrude a washer to an appropriate height and then mount strain gauges on the extruded washer. A total of four strain gauges are mounted on each transducer. Where two angled gauges are used each containing a gauge oriented in 0° and 90° as shown on Figure A.1.

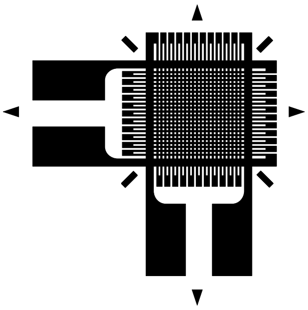

Figure A.1 Angled gauge used for the transducer

The strain gauges used are manufactured by TML and the strain gauges used are temperature compensated for mild steel. The strain gauges used is listed in Table A.3.

Strain gauge:	**Gauge factor:**	**Batch/Lot no.**	**Resistance:**	**Transeverse sensitivity**
FCA-3-11	$2.12 \pm 1\%$	GB17K/A601522	$120 \pm 0.5\Omega$	0.2%
FCA-3-11	$2.12 \pm 1\%$	MK11K/A60152A	$120 \pm 0.5\Omega$	0.2%

Table A.3 Specifications for strain gauges used for testing, made by TML.

By placing the angled gauges on opposite sides of the transducer, two gauges are in compression and two are in tension, making it possible to implement a Wheatstone full bridge. To achieve the correct measurements it is important to couple the strain gauges correct as shown on Figure A.2.

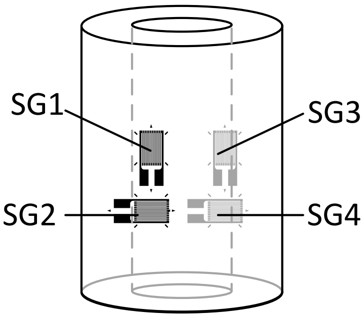

Figure A.2 Angled gauge used for the transducer

The Wheatstone bridge is a setup of resistors that amplifies the signal from strain gauge measurements. The Wheatstone bridge can be configured as a quarter bridge, half bridge, or full bridge. The full bridge configuration is the only one used during this project, thus it is the only one explained in the following. The Wheatstone full bridge is seen on Figure A.3.

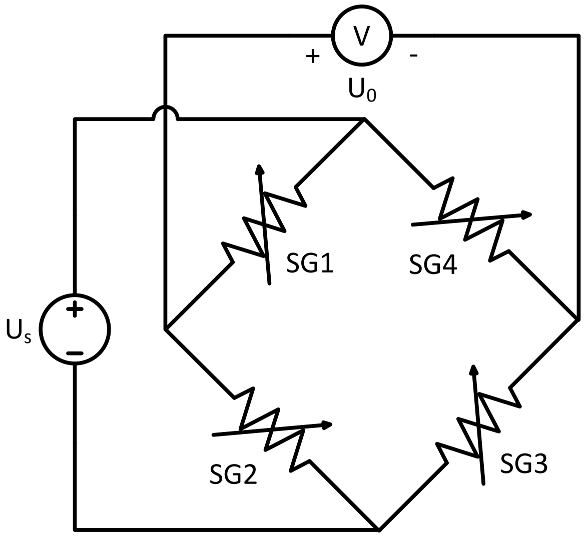

Figure A.3 The Wheatstone full bridge used for the force transducer

The Wheatstone bridge is describe by Equation (A.3), where the change of each resistor influence the measured voltage. The Wheatstone bridge acts as a signal amplifier as the change in resistance of a strain gauge is so small that it is impossible to measure.

$$V_0 = \frac{1}{4}\left(\frac{\Delta R_1}{R_1} - \frac{\Delta R_2}{R_2} + \frac{\Delta R_3}{R_3} - \frac{\Delta R_4}{R_4}\right) V_s \tag{A.3}$$

where:

V_0	Measured voltage to the wheatstone bridge, [V]
V_s	Applied voltage to the wheatstone bridge, [V]
R	Resistance, [Ω]

$$\frac{\Delta R}{R} = k_{sg}\varepsilon \tag{A.4}$$

where:

ε	Strain, [-]
k_{sg}	Gauge factor, [-]

By inserting Equation (A.4) into Equation (A.3) the strain is found directly from the input and output voltage as seen in the Equation (A.5). Since the force transducer is made by four strain gauges, all ε_i contributes to the result.

$$V_0 = \frac{k_{sg}}{4}\left(\varepsilon_1 - \varepsilon_2 + \varepsilon_3 - \varepsilon_4\right) V_s \tag{A.5}$$

From the Wheatstone full-bridge only one measurement is made, wich is the output voltage. Since the input voltage and gauge factor are constants it is possible to get a measurement of the strain combination from the four strain gauges, as shown in Equation (A.6).

$$\frac{V_0}{V_s}\frac{4}{k_{sg}} = \left(\varepsilon_1 - \varepsilon_2 + \varepsilon_3 - \varepsilon_4\right) = \varepsilon_r \tag{A.6}$$

where:

ε_r	Resultant strain measured from the Wheatstone bridge, [-]

The load applied to the force transducer is then found from the resultant strain, stated in Equation (A.6) and inserted into Equation (A.7). To calculate the normal force applied to the force transducer, it is necessary to know the material parameters of the transducer as seen in Equation (A.7). The material that is used for the force transducer is steel of the type St50-2 EN10025 which has the material parameters listed in Table A.4.

$$F_n = \frac{\varepsilon_r E}{2\left(1+\nu\right)} A_t \tag{A.7}$$

where:

F_n	Normal force, [N]
E	Modulus of Elasticity, [GPa]
ν	Poison's Ratio, [-]
A_t	Cross sectional area of the transducer, $\left[mm^2\right]$

St50-2 EN10025	
E	210GPa
ν	0.3
σ_y	285MPa

Table A.4 Material parameters of the material used in the force transducers.

Strain gauge measurement results are easily contaminated by errors. To prevent errors, precautions are discussed here. The strain gauges are connected directly into a Wheatstone bridge so the wires are so short that they do not add measurable resistance to unbalance the

Wheatstone bridge. Further more, the wires connecting the D-sub plug to the Wheatstone bridge is of equal length and type, thus the extra resistance of the wires are considered negligible.

According to Hoffmann [1989], the transverse effects can be neglected if the transverse sensitivity of the strain gauges are below 1%. According to Table A.3 none of the strain gauges used have a transverse sensitivities above 1%, whereby this effect is neglected.

Misalignment between the active direction of the strain gauge and the expected measurement direction can be neglected if it is less than 5° [Hoffmann, 1989]. The position has subsequently been checked and no misalignment has been detected on the mounted gauges, thus the misalignment error is neglected as well.

Since the strain gauges are connected in a full bridge, temperature changes affects all resistors in the bridge and contributes with the same amount of resistance change. Furthermore the gauges used are temperature compensated for mild steel, thus temperature effects are neglected.

Strain gauge error

The accuracy of strain gauge measurements are dependent on the data acquisition devices used. This section deals with the errors that the strain gauge measurements, which is carried out during the tests, contain. The error is evaluated by the accumulation law stated in Equation (A.8). This equation allows errors to be accumulated to one relative error. The equation do not take systematic errors or coarse errors, that is performed during testing, into account.

$$s(R) = \sqrt{\left(\frac{\partial R}{\partial x} s(x)\right)^2 + \left(\frac{\partial R}{\partial y} s(y)\right)^2 + \left(\frac{\partial R}{\partial z} s(z)\right)^2 + \cdots} \tag{A.8}$$

where:

$s(R)$	Relative error, [-]

To evaluate which instrumental inaccuracies contributes to the error of the strain gauge measurement, it is necessary to evaluate how the measurement is done and how they are able to contribute. For a strain gauge measurement, the strain is found by Equation (A.6), by inserting the equation into Table A.5, it is seen that the unlinearity of the Wheatstone bridge, the data acquisition device and the gauge factor contributes to the error. The tolerances are seen in Table A.5.

	Tolerance
Non-linearity of the Wheatstone bridge [Mouritsen, 2010]	0.05%
Error tolerance on data acquisition device	0.1%
Gauge factor [Tokyo Sokki Kenkyujo Co., Ltd., 2012]	1%

Table A.5 The errors that is taken into account when calculating the empirical deviation.

It is assumed that the tolerance of the data acquisition equipment is equal to two times the empirical scattering [Mouritsen, 2010]. By inserting Equation (A.6) into Equation (A.8), the error can be found for a strain gauge, as stated in Equation (A.9).

$$\frac{s(\varepsilon_r)}{\varepsilon_r} = \sqrt{\left(1\frac{s(k_{sg})}{k_{sg}}\right)^2 + \left(1\frac{s\left(\frac{V_0}{V}\right)}{\left(\frac{V_0}{V}\right)}\right)^2} \tag{A.9}$$

It is not possible to insert the error of the data acquisition device directly into Equation (A.9), since several tolerances are linked to the data acquisition. By utilizing the errors in Table A.5 and the accumulation law, a total error is found, which is done in Equation (A.10).

$$\frac{s\left(\frac{V_0}{V}\right)}{\left(\frac{V_0}{V}\right)} = \sqrt{(0.025\%)^2 + (0.05\%)^2} = 0.056\% \tag{A.10}$$

The total error of the strain gauges in the Wheatstone bridge is found in Equation (A.11).

$$\frac{s\left(k_{sg}\right)}{\left(k_{sg}\right)} = \sqrt{\left(\frac{1}{4}\cdot 0.5\%\right)^2 + \left(-\frac{1}{4}\cdot 0.5\%\right)^2 + \left(\frac{1}{4}\cdot 0.5\%\right)^2 + \left(-\frac{1}{4}\cdot 0.5\%\right)^2} = 0.25\% \tag{A.11}$$

Utilizing the result from Equation (A.10) and Equation (A.11) the total error of the strain measurement is found in Equation (A.12).

$$\frac{s\left(\varepsilon_r\right)}{\left(\varepsilon_r\right)} = \sqrt{(-1\cdot 0.056\%)^2 + (1\cdot 0.25\%)^2} = 0.256\% \tag{A.12}$$

The errors from the strain gauges and data acquisition devices are now found but if Equation (A.7) is inserted into the accumulation law, it is seen that the contributions of the area and material parameters has to be included as shown in Equation (A.13).

$$\frac{s\left(F_n\right)}{\left(F_n\right)} = \sqrt{+1\cdot\left(\frac{s\left(\varepsilon_r\right)}{\left(\varepsilon_r\right)}\right)^2 + \left(+1\cdot\frac{s\left(E\right)}{\left(E\right)}\right)^2 + \left(+1\cdot\frac{s\left(A_t\right)}{\left(A_t\right)}\right)^2 + \left(-2\cdot\frac{s\left(\nu\right)}{\left(\nu\right)}\right)^2} \tag{A.13}$$

The precision of the material parameters is not known and tensile tests of the material used, is not performed. Thus the material parameters influence on the empirical scattering is neglected, but still knowing that they are important to the empirical scattering. The area of the transducer is known and the empirical scattering of the area is found, by inserting the formula for a circle containing a hole, into the accumulation law, this gives the expression stated in Equation (A.14).

$$s\left(A\right) = \sqrt{\left(\frac{\pi D}{2}s\left(D\right)\right)^2 + \left(-\frac{\pi d}{2}s\left(d\right)\right)^2} \tag{A.14}$$

The area is measured by vernier caliper and the accuracy, for the digital vernier caliper used for measuring the diameters, is 0.01mm. Thus the empirical scattering of the area is calculated in Equation (A.15) for a inner diameter of 12.05m and outer diameter of 23.66mm.

$$s\left(A\right) = \sqrt{\left(\frac{\pi 23mm}{2} \cdot \frac{0.01mm}{2}\right)^2 + \left(-\frac{\pi 12mm}{2} \cdot \frac{0.01mm}{2}\right)^2} = 0.207mm^2 \tag{A.15}$$

$$\frac{s\left(A\right)}{\left(A\right)} = \frac{0.207mm^2}{\frac{\pi}{4}D^2 - \frac{\pi}{4}d^2} = \frac{0.207mm^2}{320.639mm^2} = 0.065\% \tag{A.16}$$

The final empirical scattering on the measured normal force is then found in Equation (A.17) when the results from Equation (A.12) and Equation (A.16) are inserted into Equation (A.13), while neglecting the material parameters effect.

$$\frac{s\left(F\right)}{\left(F\right)} = \sqrt{\left(+1 \cdot 0.256\right)^2 + \left(-1 \cdot 0.065\right)^2} = 0.263\% \tag{A.17}$$

A.1.2 Transducer connection to equipment

The transeducer has to be connected to a HBM Spider8-30 box, thus it is necessary to connect the four strain gauges mounted in a bridgestone full bridge to a 15 pin D-sub plug. The connection to the D-sub plug is shown in Figure A.4, where it is important to wire the wheatstone bridge correctly to the exact pins on the D-sub plug.

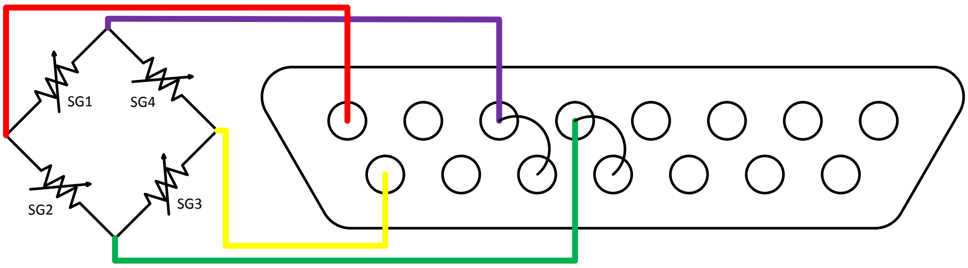

Figure A.4 Illustrates how the wheatstone bridge is hooked up to the D-sub plug.

From Figure A.4 it is not possible to change any of the wiring, as every wire is mounted according to Figure A.5 and the poles of the measured and applied voltages must not be changed in the wheatstone bridge.

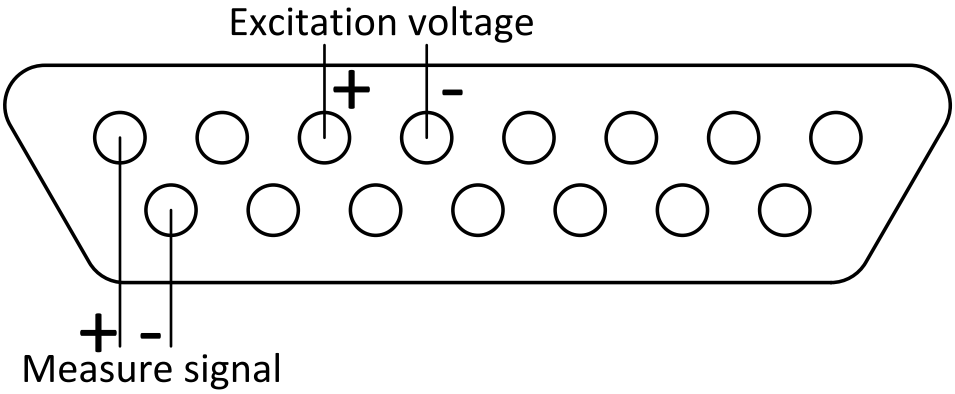

Figure A.5 Illustrates how the D-sub plug is configured.

A.1.3 Transducer calibration

When the transducers are manufactured, they have to be calibrated to ensure that the measured load is equal to the applied. For data acquisition a HBM Spider8-30 box is used along with the software CATMAN EASY. This software do not utilize the material parameters and the transducer shape, as expected in the calculation of the empirical scattering of the transducer. Instead the software requires two measurements, where very well defined loads are applied, and the software uses the defined loads as calibration references.

The calibration is carried out when the transducer is applied with a load of 20.36kN and the output voltage is measured as a reference. Then a load of 33.93kN is applied on the force transducer. The output voltage is measured and a reference is made to the load applied.

The loads are applied by the ZWICK Z100 tensile test machine as shown in Figure A.6. The tensile test machine is used as this is the only available equipment that accurately can apply more than a 1kN.

Figure A.6 The M12 transducer mounted in the tensile test machine

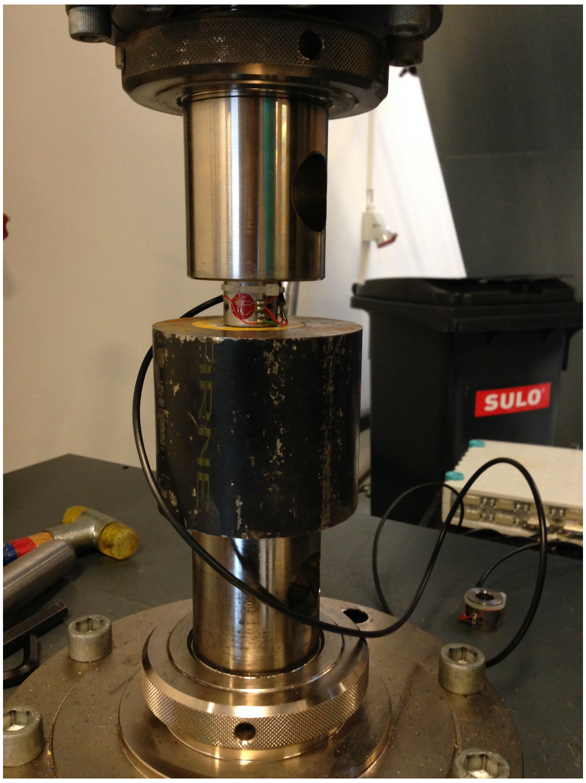

Figure A.7 The M12 transducer mounted in the tensile test machine

A third step is carried out where a two other loads are applied to see if the load reading from the transducer match the one from the tensile test machine. If the final reading is correct the transducer is calibrated.

In this way of calibrating the load transducer, it is not possible to get the same accuracy of the transducer. As the results is observed to deviate and the transducer is needed to be calibrated every time is has been unplugged from the software.

Working drawings B

I this appendix the working drawings for the manufactured pieces are found. Tolerances are given by DIN ISO 2768-m unless other tolerances are given in the drawings.

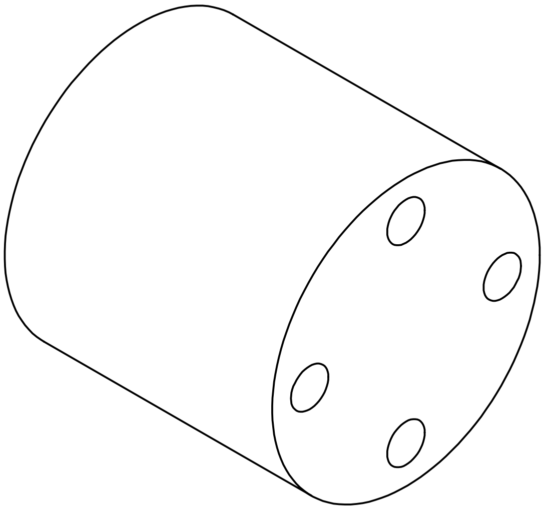

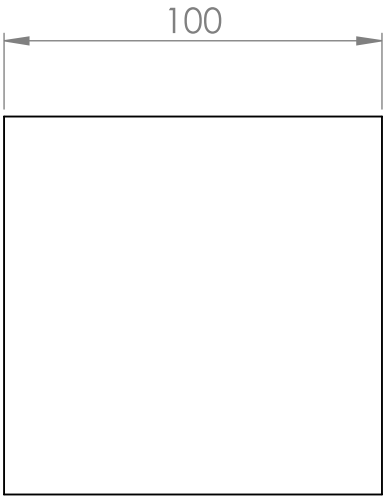

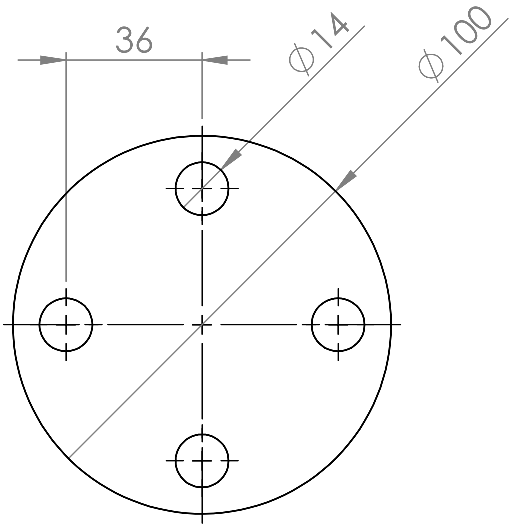

UNLESS OTHERWISE SPECIFIED:
DIMENSIONS ARE IN MILLIMETERS
SURFACE FINISH:
TOLERANCES:
LINEAR:
ANGULAR:

FINISH:

DEBUR AND
BREAK SHARP
EDGES

DO NOT SCALE DRAWING

REVISION

	NAME	SIGNATURE	DATE
DRAWN			
CHK'D			
APPV'D			
MFG			
Q.A			

TITLE:

MATERIAL:

WEIGHT:

DWG NO.

multibolt

A4

SCALE:1:1

SHEET 1 OF 1

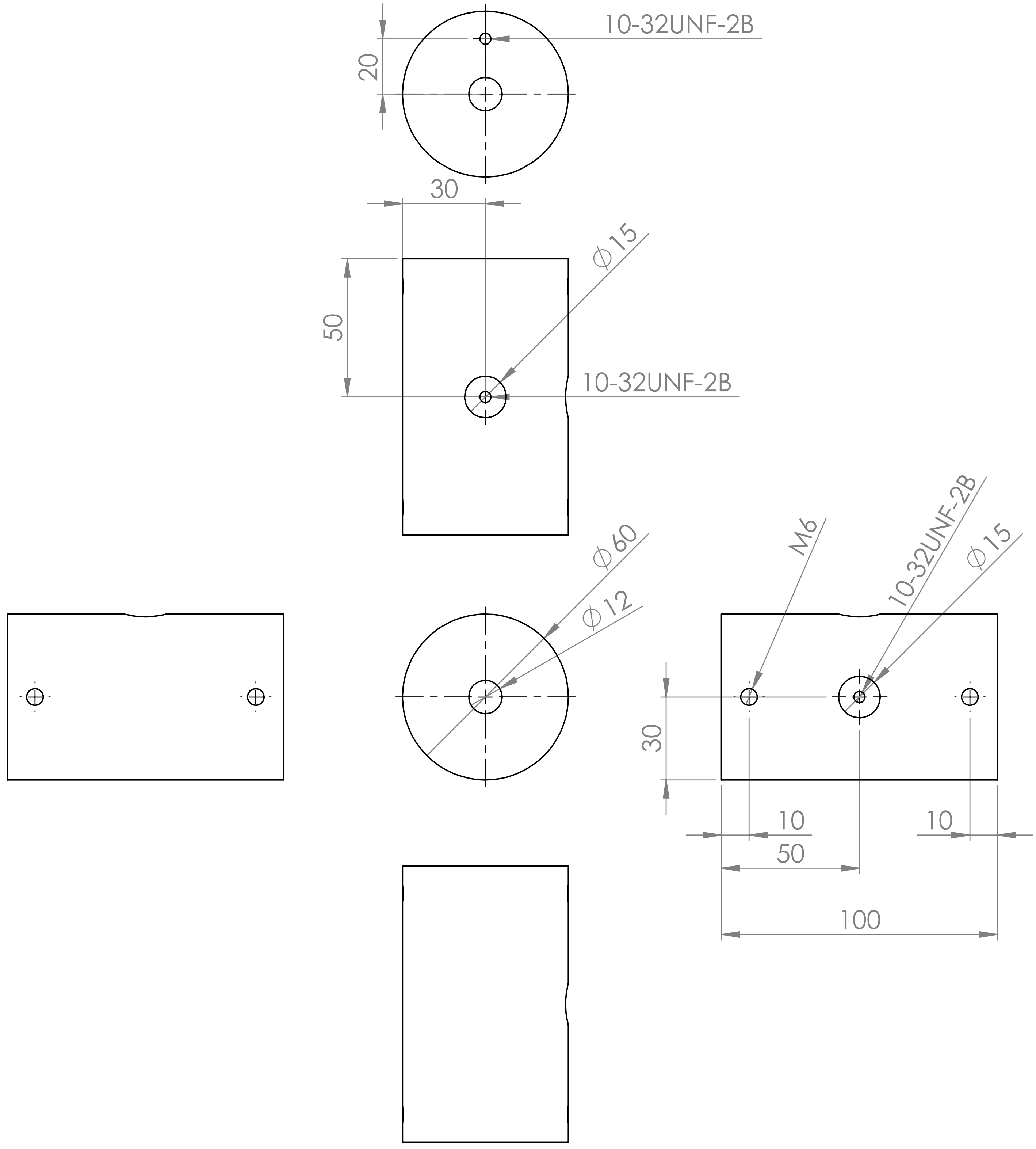

UNLESS OTHERWISE SPECIFIED: DIMENSIONS ARE IN MILLIMETERS SURFACE FINISH: TOLERANCES: LINEAR: ANGULAR:	FINISH:	DEBUR AND BREAK SHARP EDGES

DO NOT SCALE DRAWING

REVISION

	NAME	SIGNATURE	DATE
DRAWN			
CHK'D			
APPV'D			
MFG			
Q.A			

TITLE:

MATERIAL:

DWG NO.

singlebolt

A4

WEIGHT:

SCALE:1:2

SHEET 1 OF 1

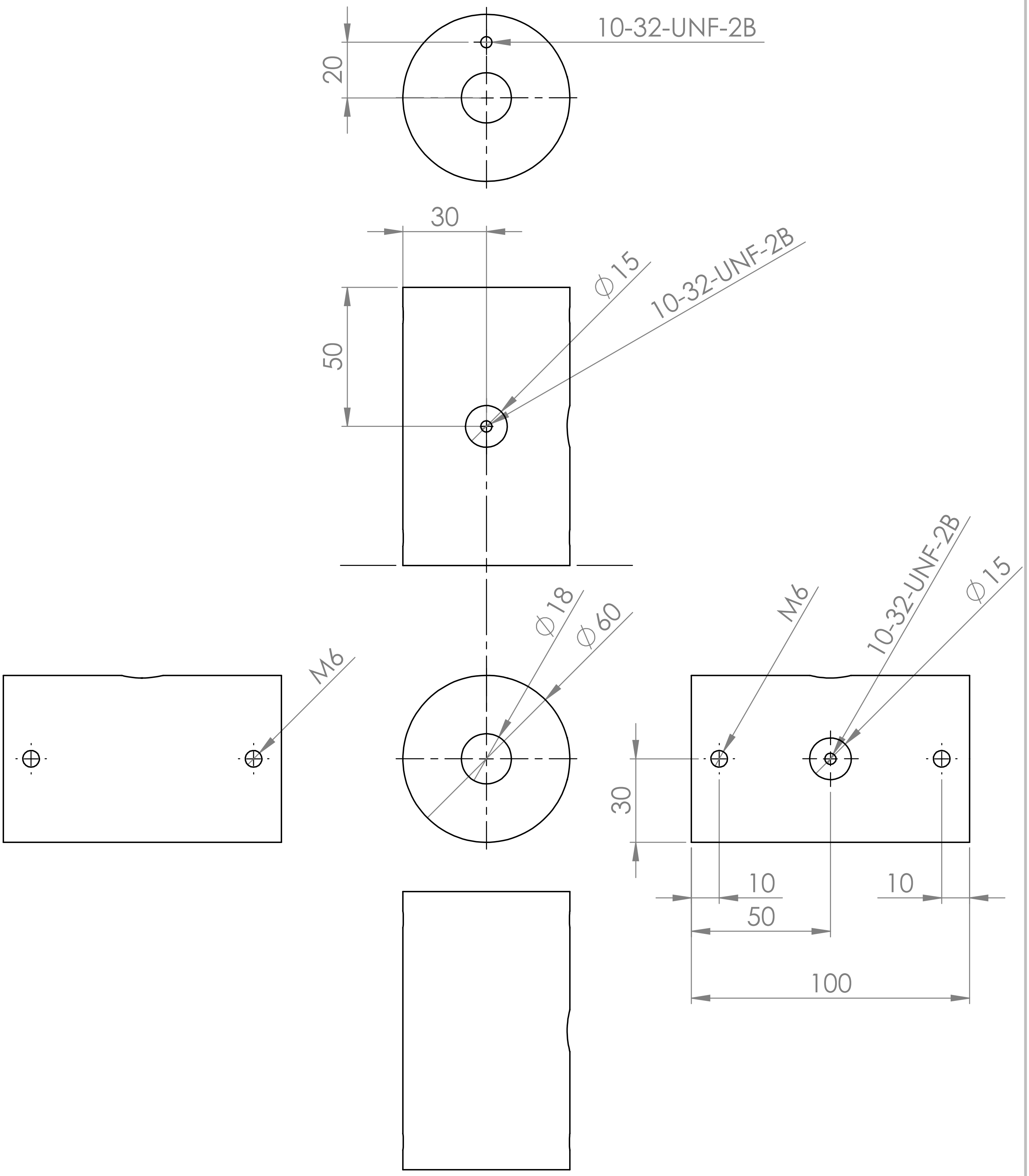

UNLESS OTHERWISE SPECIFIED:
DIMENSIONS ARE IN MILLIMETERS
SURFACE FINISH:
TOLERANCES:
LINEAR:
ANGULAR:

FINISH:

DEBUR AND
BREAK SHARP
EDGES

DO NOT SCALE DRAWING

REVISION

	NAME	SIGNATURE	DATE			
DRAWN						
CHK'D						
APPV'D						
MFG						
Q.A						

TITLE:

MATERIAL:

DWG NO.

singlebolt M18

A4

WEIGHT:

SCALE:1:2

SHEET 1 OF 1

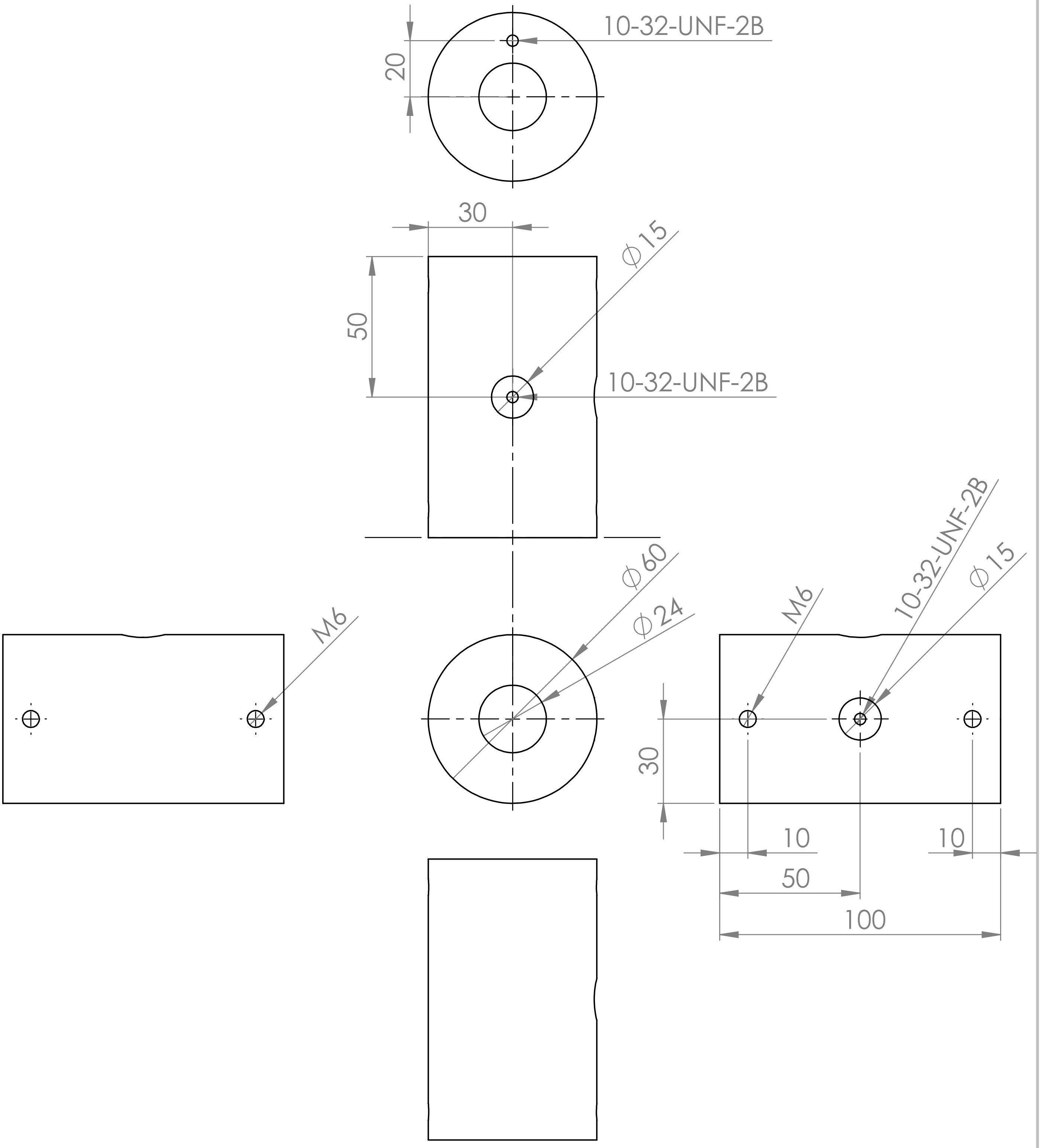

UNLESS OTHERWISE SPECIFIED:
DIMENSIONS ARE IN MILLIMETERS
SURFACE FINISH:
TOLERANCES:
LINEAR:
ANGULAR:

FINISH:

DEBUR AND
BREAK SHARP
EDGES

DO NOT SCALE DRAWING

REVISION

	NAME	SIGNATURE	DATE		
DRAWN					
CHK'D					
APPV'D					
MFG					
Q.A					

TITLE:

MATERIAL:

WEIGHT:

DWG NO.

singlebolt M24

A4

SCALE:1:2

SHEET 1 OF 1

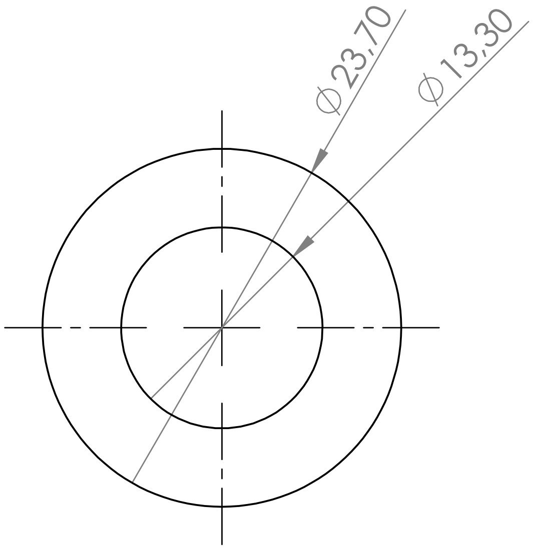

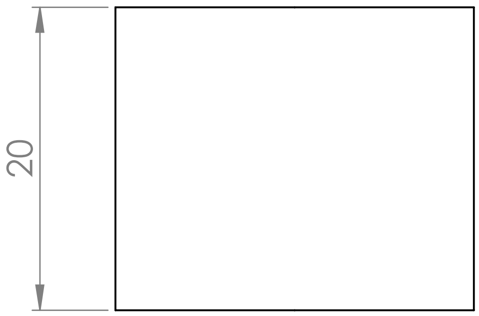

UNLESS OTHERWISE SPECIFIED: DIMENSIONS ARE IN MILLIMETERS SURFACE FINISH: TOLERANCES: LINEAR: ANGULAR:	FINISH:	DEBUR AND BREAK SHARP EDGES	DO NOT SCALE DRAWING

REVISION

	NAME	SIGNATURE	DATE
DRAWN			
CHK'D			
APPV'D			
MFG			
Q.A			

TITLE:

MATERIAL:

WEIGHT:

DWG NO.

M12 transducer

A4

SCALE:2:1

SHEET 1 OF 1

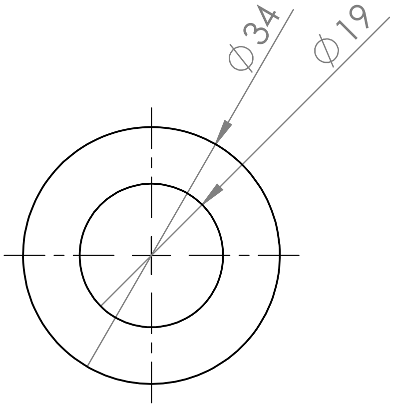

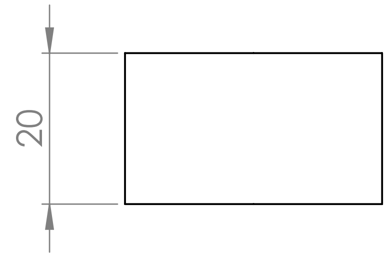

UNLESS OTHERWISE SPECIFIED:
DIMENSIONS ARE IN MILLIMETERS
SURFACE FINISH: $\sqrt{}$ U Ra 3,2 / L Ra 1,6
TOLERANCES:
LINEAR:
ANGULAR:

FINISH:

DEBUR AND
BREAK SHARP
EDGES

DO NOT SCALE DRAWING

REVISION

	NAME	SIGNATURE	DATE
DRAWN			
CHK'D			
APPV'D			
MFG			
Q.A			

TITLE:

MATERIAL: S355J2

WEIGHT:

DWG NO.

M18 transducer

A4

SCALE:1:1

SHEET 1 OF 1

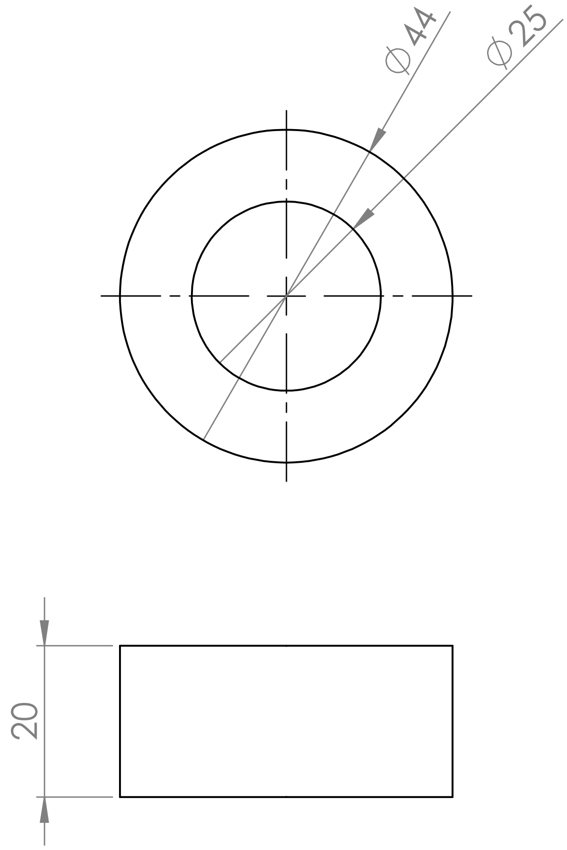

UNLESS OTHERWISE SPECIFIED:
DIMENSIONS ARE IN MILLIMETERS
SURFACE FINISH: √ U Ra 3,2 L Ra 1,6
TOLERANCES:
LINEAR:
ANGULAR:

FINISH:

DEBUR AND
BREAK SHARP
EDGES

DO NOT SCALE DRAWING

REVISION

	NAME	SIGNATURE	DATE
DRAWN			
CHK'D			
APPV'D			
MFG			
Q.A			

TITLE:

MATERIAL: S355J2

WEIGHT:

DWG NO. M24 transducer

A4

SCALE:1:1

SHEET 1 OF 1

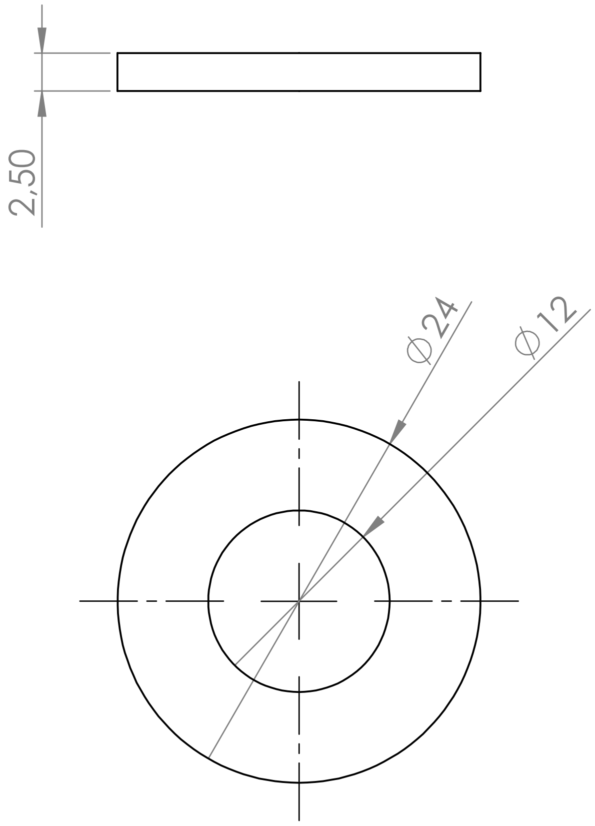

UNLESS OTHERWISE SPECIFIED:
DIMENSIONS ARE IN MILLIMETERS
SURFACE FINISH:
TOLERANCES:
LINEAR:
ANGULAR:

FINISH:

DEBUR AND
BREAK SHARP
EDGES

DO NOT SCALE DRAWING

REVISION

	NAME	SIGNATURE	DATE
DRAWN			
CHK'D			
APPV'D			
MFG			
Q.A			

TITLE:

MATERIAL:

WEIGHT:

DWG NO.

washer_standard

A4

SCALE:2:1

SHEET 1 OF 1

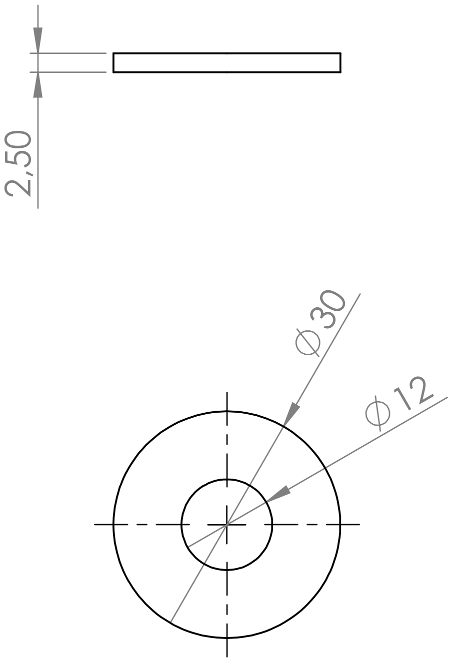

UNLESS OTHERWISE SPECIFIED:
DIMENSIONS ARE IN MILLIMETERS
SURFACE FINISH:
TOLERANCES:
LINEAR:
ANGULAR:

FINISH:

DEBUR AND
BREAK SHARP
EDGES

DO NOT SCALE DRAWING

REVISION

	NAME	SIGNATURE	DATE
DRAWN			
CHK'D			
APPV'D			
MFG			
Q.A			

TITLE:

MATERIAL:

DWG NO.

washer_large

A4

WEIGHT:

SCALE:1:1

SHEET 1 OF 1

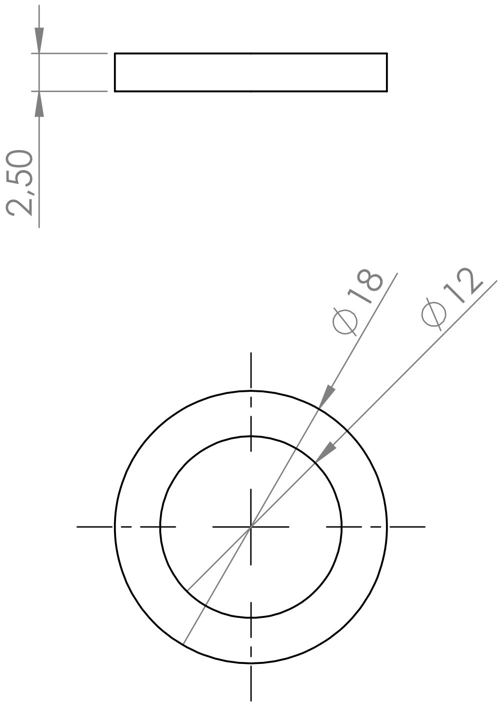

UNLESS OTHERWISE SPECIFIED:
DIMENSIONS ARE IN MILLIMETERS
SURFACE FINISH:
TOLERANCES:
LINEAR:
ANGULAR:

FINISH:

DEBUR AND
BREAK SHARP
EDGES

DO NOT SCALE DRAWING

REVISION

	NAME	SIGNATURE	DATE
DRAWN			
CHK'D			
APPV'D			
MFG			
Q.A			

TITLE:

MATERIAL:

WEIGHT:

DWG NO.

washer_small

A4

SCALE:2:1

SHEET 1 OF 1

Equipment information C

This appendix contains the information about the equipment used in the project, divided into equipment categories. All equipment is Brüel & Kjær products unless otherwise stated.

C.1 Pulse system

The pulse system is used in collaboration with a pc, for data acquisition and signal processing.

Pulse analyzer

Designation	**Type**	**IP**	**Subnet**
Pulse analyzer	3560C	10.10.10.50	255.0.0.0

Table C.1 Equipment information for the pulse system setup.

C.2 Impact hammer

The steel tipped impact hammer setup consists of the hammer itself, a transducer inside the hammer, and a preamplifier to connect it to the pulse analyzer. The equipment information is found in Table C.1

B&K Steel tippped impact hammer

Designation	**Type**	**Serial number**
Impact hammer	8202	1123601
Transducer	8200	1183178
Preamplifier	2647-A	2207156

Table C.2 Equipment information for the impact hammer setup.

The aluminum tipped impact hammer made by Endeveco and the setup contains the same components as the steel tipped hammer, although the preamplifier is build into the hammer.

Endeveco Aluminum tipped impact hammer

Designation	**Type**	**Serial number**
Impact hammer	2302-10	-

Table C.3 Equipment information for the impact hammer setup.

C.3 Microphones

The microphone contains a built in preamplifier and so it is connected directly to the analyzer. Information on the microphone can be seen in Table C.4.

Microphone (mic)

Designation	**Type**	**Serial number**
Accelerometer	4189	2275511

Table C.4 Equipment information for the microphone.

C.4 Accelerometers

In total three different accelerometers are used for the measurements, acc1, acc2, and acc3. Each of these are connected to the pulse system through a preamplifier, equipment information about each setup can be found in Table C.5, C.6, and C.7.

Accelerometer 1 (acc 1)

Designation	**Type**	**Serial number**
Accelerometer	4384V	2220425
Preamplifier	2647-A	2207157

Table C.5 Equipment information for accelerometer 1.

Accelerometer 2 (acc 2)

Designation	**Type**	**Serial number**
Accelerometer	4382V	2232112
Preamplifier	2647-A	2207158

Table C.6 Equipment information for accelerometer 2.

Accelerometer 3 (acc 3)

Designation	**Type**	**Serial number**
Accelerometer	4382V	2232113
Preamplifier	2647-A	2207159

Table C.7 Equipment information for accelerometer 3.

Verification of model

D

A model of the beam, spring, damper, and mass has been established in Section 6.1. However the accuracy and correctness of the model is unknown, so to verify the model, it is compared to elementary case for a beam. In this way it is possible to see if the derivation of equations is done correctly and if the model is usable. The cantilever beam is initially tested followed by a test of the spring/mass system and finally the coupled system is verified.

D.1 Beam verification

For the test of the cantilever beam, the weight of the mass in the spring/mass part of the system is set to a very small value. The stiffness of the spring is also set to a large number compared to the equivalent spring constant for the beam. In this way the spring and mass can be considered to be decoupled from the beam as they will not influence the resonant frequency of the beam. Furthermore the model is based on Bernoulli Euler theory so the cantilever beam has to be long and slender. The parameters used for the verification is stated in Table D.1. The beam is set to have a circular cross section. The MATLAB script, created to run the Bernoulli-Euler model where the spring/mass is decoupled, is attached on the Appendix CD[1].

Model test parameters	
E	$70GPa$
ρ	$2700\frac{kg}{m^3}$
L	$2m$
d	$0.06m$
I	$\frac{\pi}{64}d^4 = 6.3617 \cdot 10^{-7}m^4$
A	$\frac{\pi}{4}d^2 = 0.0028m^2$
m	$0.0001kg$
c	$0\frac{N\,s}{m}$
k	$10^{10}\frac{N}{m}$
F	100N

Table D.1 Input parameters for the analytical model for verifying the beam system of the model.

The equivalent spring constant for the beam is calculated in Equation (D.1) by inserting the parameters listed in Table D.1. The spring stiffness has to be at least 10 times larger than the equivalent beam stiffness to ensure that the spring and mass do not influence the beams resonance frequencies.

$$k_{beam} = \frac{3EI}{L^3} = 16700\frac{N}{m} \tag{D.1}$$

---

[1] Appendix CD\MATLAB \Analytical\BeamMassForVeryficateBeam.m

where:

k_{beam} | Equavalent stiffness of a cantilever beam, $[\frac{N}{m}]$

The spring constant is compared the equivalent spring stiffness of the beam to ensure that the spring is sufficiently stiff. Hence motion of the mass follows the beam. It is concluded that the spring stiffness is large enough as it is alot larger than the equivalent beam stiffness. The elementary eigenfrequencies for a cantilever beam is found in Rao [2011] and the eigenfrequencies is calculated from Equation (D.2) and values of βL is listed in Table D.2 along with the four first modal frequencies, found by Equation (D.2).

$$f = \frac{(\beta L)\sqrt{\frac{EI}{\rho A_c L^4}}}{2\pi} \tag{D.2}$$

	βL	**Modal freq. [Hz]**
f_1	1.875104	10.68
f_2	4.694091	66.96
f_3	7.854757	187.49
f_4	10.995541	367.41

Table D.2 The modal frequencies from the elementary model.

For the analytical model, the frequencies are discretized and the response is calculated for frequencies from 0Hz to 400Hz with intervals of 2Hz. At frequencies close to the expected modal frequencies from Table D.2 a finer discretization, of 0.025Hz, is used. As the amplitude along the length of the beam is of no interest a 2D plot is created, as seen in Figure D.1.

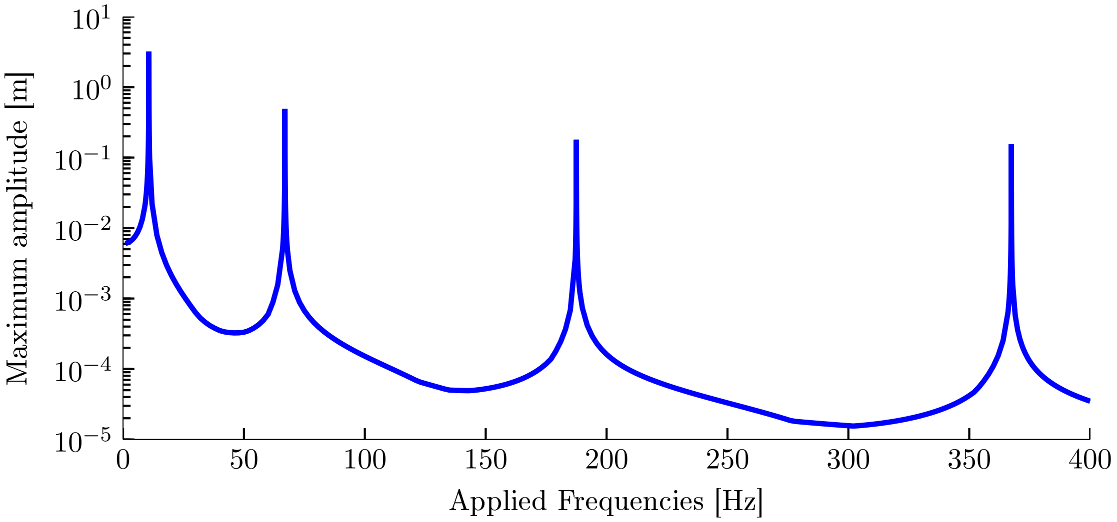

Figure D.1 The resonance frequencies of the beam in the the analytical model when the mass and spring is decoupled

From Figure D.1 the four first modal frequencies are seen and these are compared to the elementary model stated in Table D.2. The comparison of the resonance frequencies are seen in Table D.3, from which it is concluded that the model is sufficiently accurate as the frequencies are within 0.000456% of each other. Hence the difference is neglectable and the analytical model for the beam part is good.

Mode	Analytical model Hz	Elementary model Hz	Difference
1	10.68	10.68	0.000456%
2	66.95	66.96	0.000163%
3	187.5	187.49	-3.9665e-05%
4	367.4	367.41	2.899e-05%

Table D.3 Resonance frequencies from elementary model and the analytical model.

D.2 Spring/mass verification

The spring/mass part of the model also has to be verified. This is done by increasing the beam parameters so the beam is very stiff and will not move to the forcing of the spring and mass and acts as ground. The MATLAB script, created to run the Bernoulli-Euler model where the spring/mass is decoupled, is attached on the Appendix CD[2]. Equation (D.3) is used as a reference to the eigenfrequency of the spring/mass system in the analytical model.

$$f_r = \frac{\sqrt{\frac{k}{m}}}{2\pi} \tag{D.3}$$

where:

f_r	Undamped resonant frequency, [Hz]

The parameters used for verifying the spring mass part of the analytical model is stated in Table D.4.

Model test parameters	
E	$1000GPa$
ρ	$1\frac{kg}{m^3}$
L	$2m$
d	$1m$
I	$\frac{\pi}{64}d^4 = 0.04909m^4$
A	$\frac{\pi}{4}d^2 = 0.7854m^2$
m	$0.5kg$
c	$0\frac{N\,s}{m}$
k	$8000\frac{N}{m}$

Table D.4 Input parameters for the analytical model for verifying the spring/mass part of the model.

Inserting the parameters from Table D.4 into Equation (D.3) the eigenfrequency is found for the spring/mass system to be 20.13Hz. The response of the analytical model is calculated with discretized frequencies from 0Hz to 50Hz with intervals of 1Hz. At frequencies close to the expected frequency of 20.13Hz a finer discretization of 0.01Hz is used. The result is shown in Figure D.2.

---

[2] Appendix CD\MATLAB \Analytical\BeamMassForVeryficateMass.m

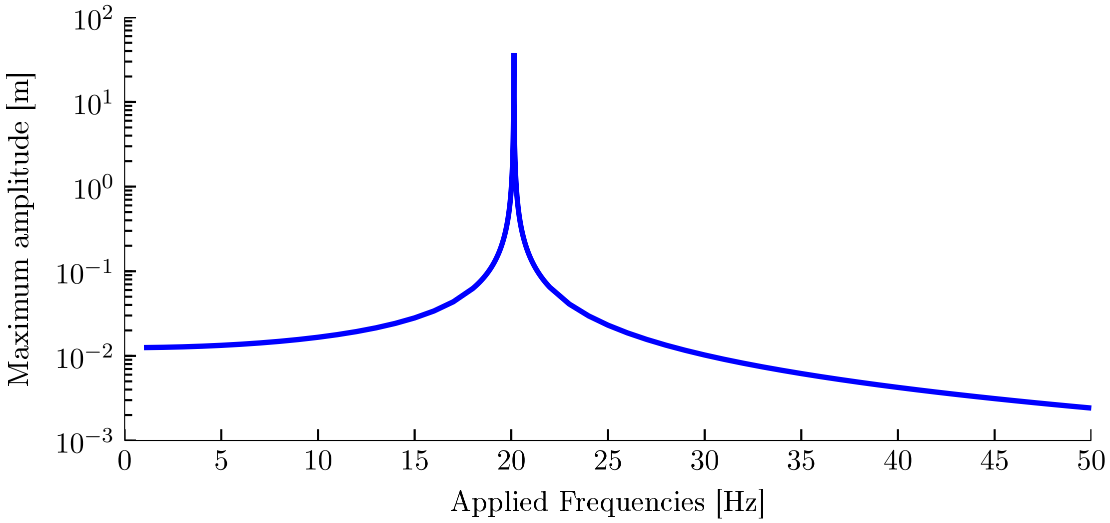

Figure D.2 The modal frequencies of the spring and mass in the the analytical model when the beam is anticipated as ground.

In Figure D.2 the resonant frequency is found to be 20.13Hz, which is exactly the same value as found by Equation (D.3). Thus the model is expected to produce valid results.

D.3 verification of weak/strong coupled system

The model has now been tested, for both beam and spring/mass response, where each part of the system is decoupled and verified according to elementary solutions. During this section the coupled system is going to be tested, to see if the system produce acceptable results. Furthermore the system is tested by letting the resonant frequency of the beam and spring/mass system being very close to each other.

Initially the coupled system is solved for parameters stated in Table D.5. The coupled system is expected to show a resonant frequency of the mass and beam and between the two resonance frequencies an antiressonance is expected to appear.

Model test parameters	
E	$200GPa$
ρ	$7800\frac{kg}{m^3}$
L	$1m$
d	$0.06m$
m	$0.5kg$
c	$0\frac{N\,s}{m}$
k	$10000\frac{N}{m}$

Table D.5 Input parameters for the coupled model.

The system response is calculated for a frequency range of 0Hz to 80Hz with intervals of 0.1Hz. The calculated response of the the beam is seen in Figure D.3 and the deflection of the mass is seen in Figure D.4. By using Equation (D.3) and inserting parameters from Table D.5 the spring/mass resonant frequency is found to be 22.51Hz, which is also seen as a resonance point on Figure D.3 and Figure D.4. The first resonant frequency of the beam is also seen on the figures at a frequency of 43.2Hz.

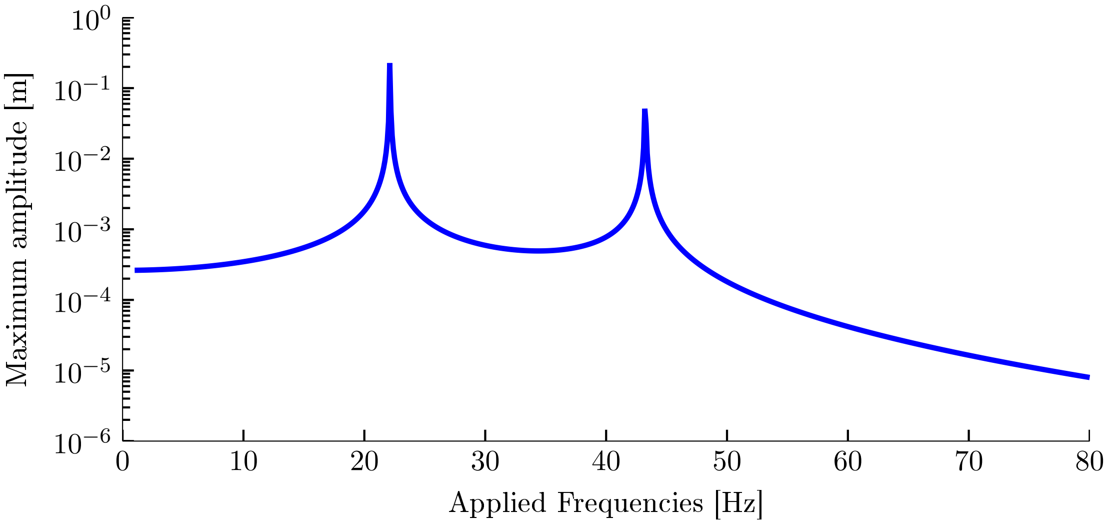

Figure D.3 The response from the beam deflection when the system is coupled.

The calculated response of the mass indicates a anti-resonance point between the two resonances, just as expected. The location of the anti-resonance is dependent on the resonance points on each side of the anti-resonance. In this case, the anti-resonance is very close to the beam response, which could be due to the beam having a lot higher stiffness than the spring/mass.

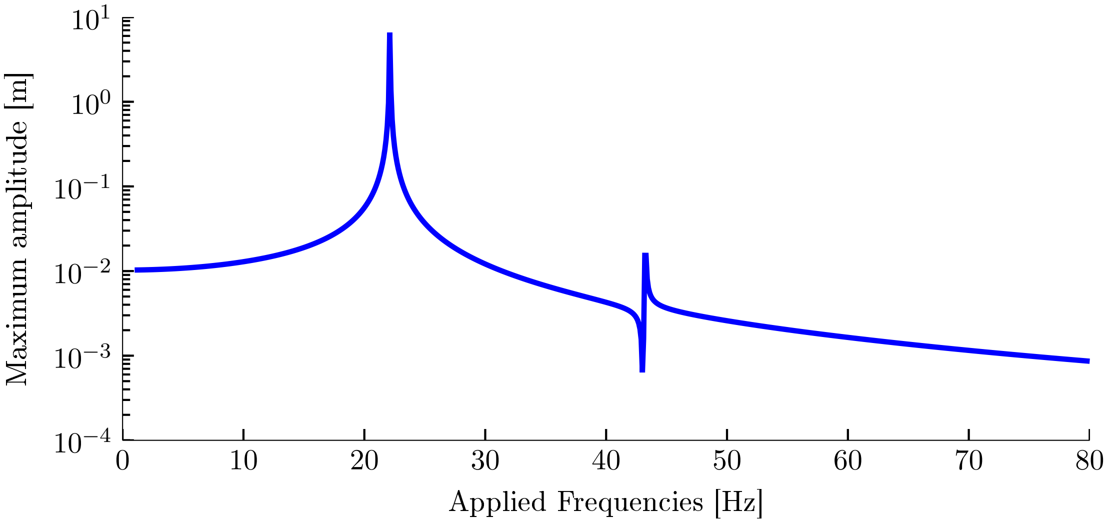

Figure D.4 The response from the mass deflection when the system is coupled.

The coupled system is considered as yielding correct results, as results match elementary solutions. It is still necessary to investigate what happens when the resonant frequency of the spring/mass and the first resonant frequency of the beam is very close.

To evaluate the coupled model for resonance frequencies of the beam and spring/mass being close, it it necessary to find the required by parameters, by fitting the response of the decoupled system, as done in Appendix D.1 and Appendix D.2. It is expected that the two frequencies will change in the coupled system, compared to the decoupled system.

By using the parameters in Table D.5, the first resonant frequency of the beam is found to 42.5Hz and by increasing the spring constant to $k = 36000\frac{N}{m}$ the eigenfrequency of the spring/mass is 42.7Hz. The calculated response of the system with two close resonance frequencies is seen on Figure D.5 and Figure D.6, where it is seen that the freuquencies is pushed away from each other. This change in frequencies is caused by the merging of the two systems, where the components now acts as part of a single system rather than two individual systems, and thus influence each other directly.

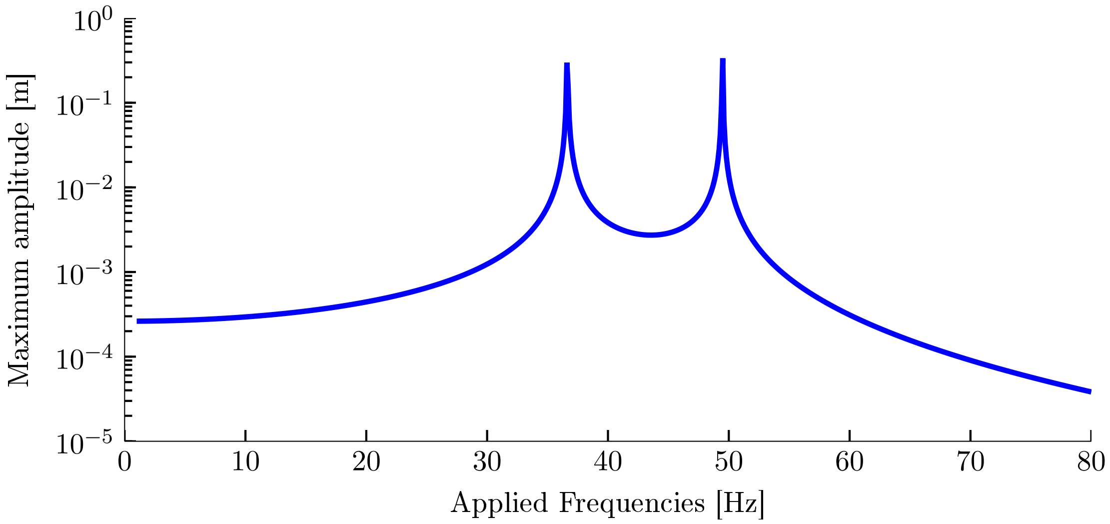

Figure D.5 The amplitude of the beam when resonance frequencies of the beam and spring/mass are located closely to each other.

From Figure D.6 it is seen that the antiresonance of the spring/mass is no longer very close to the beam resonance but i the middle of the two resonance peaks. This is due to the increased stiffness of the spring, which also increase the resonant frequency.

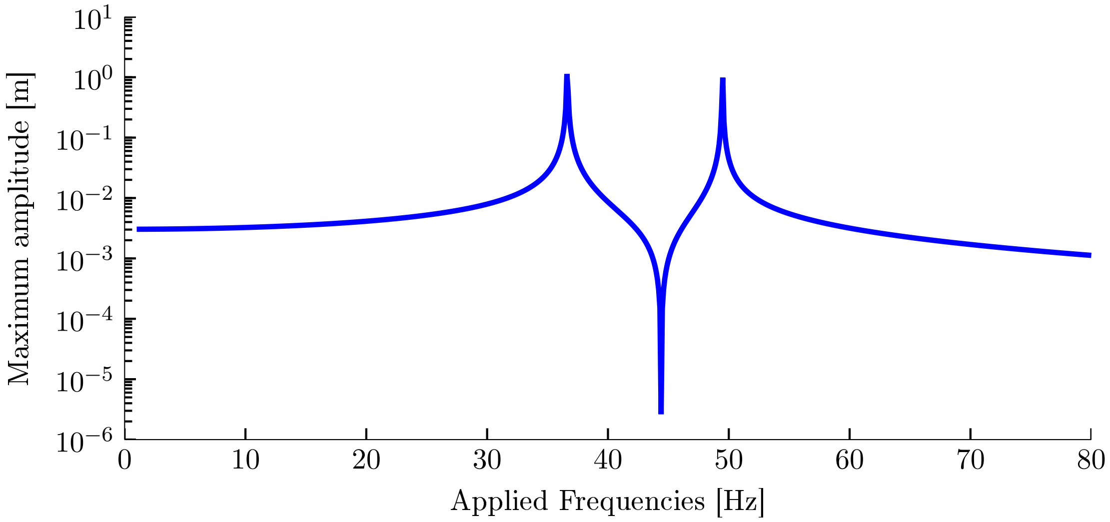

Figure D.6 The amplitude of the mass when resonance frequencies of the beam and spring/mass are located closely to each other.

From all the tests carried out on the model, it seems that the system produce the results that are expected and is thereby considered as valid when the damper is not included. A study when the damper is included is carried out in Section 6.5.1.

Analytical model with Timoshenko beam theory E

This appendix will deal with expanding the analytical model from Chapter 6 from Bernoulli-Euler beam theory to Timoshenko beam theory. This is due to the interest of higher order eigenfrequencies of the bolt. The Timoshenko theory includes the shear deformation of the beam where the Bernoulli-Euler theory assumes infinite shear stiffness.

E.1 Deriving the governing equations

As for the Bernouilli-Euler beam theory the timoshenko theory is initiated by stating the boundary conditions. For the Timoshenko beam theory the boundary conditions is not only stated by the derivatives of the deflection but stated by the deflection and the angle deflection. The Timoshenko boundary conditions for the cantilever beam is stated in Equation (E.1) to Equation (E.3). For a cantilever beam the deflection and angle deflection at the clamped end is equal to zero as stated in Equation (E.1) and Equation (E.2). The free end is subjected to a shear force by the spring and damper but no moment is present at the free end. Thus no curvature exists at the the free end as stated in Equation (E.3).

$$w(0,t) = 0 \tag{E.1}$$

$$\psi(0) = 0 \tag{E.2}$$

$$\psi'(L) = 0 \tag{E.3}$$

where:

$w(x,t)$	Deflection along the length of the beam, [m]

The kinetic energy is stated in Equation (E.4) and the potential energy is stated in Equation (E.5). The first part of each equation is for the timoshenko beam theory and the last part is for the spring and mass. For the initial considerations the damper and applied force can be moved to the right hand side as explained in Section 6.1. The method of writing derivatives introduced in Section 6.1 is also used throughout this appendix.

$$T = \frac{1}{2}\int_0^L \rho A_c \dot{w}^2 \,\mathrm{d}x + \frac{1}{2}\int_0^L \rho I \dot{\psi}^2 \,\mathrm{d}x + \frac{1}{2} m \dot{z}^2 \tag{E.4}$$

$$V = \frac{1}{2}\int_0^L EI\psi'^2 \,\mathrm{d}x + \frac{1}{2}\int_0^L \kappa G A_c \big(w' - \psi\big)^2 \,\mathrm{d}x + \frac{1}{2} k \big(w(L) - z\big)^2 \tag{E.5}$$

where:

T	Kinetic energy, [J]
V	Potential energy, [J]
L	Length, [m]
ρ	Density, $\left[\frac{kg}{m^3}\right]$
A_c	Cross sectional area, $\left[m^2\right]$
m	Mass, [kg]
E	Modulus of Elasticity, [GPa]
I	Area moment of inertia, $\left[m^4\right]$
k	Spring constant, $\left[\frac{N}{m}\right]$
$z(t)$	Mass deflection, [m]
κ	Timoshenko shear coefficient, [-]
G	Shear modulus, [GPa]

The kinetic and potential energy are inserted into Hamilton's principle.

$$\begin{aligned}\delta \int_{t_1}^{t_2} \Bigg[\frac{1}{2}\int_0^L \rho A_c \dot{w}^2 \,\mathrm{d}x + \frac{1}{2}\int_0^L \rho I \dot{\psi}^2 \,\mathrm{d}x + \frac{1}{2} m \dot{z}^2 - \frac{1}{2}\int_0^L EI\psi'^2 \,\mathrm{d}x \\ -\frac{1}{2}\int_0^L \kappa G A_c \big(w' - \psi\big)^2 \,\mathrm{d}x - \frac{1}{2} k\big(w(L) - z\big)^2 \Bigg] \,\mathrm{d}t = 0\end{aligned} \tag{E.6}$$

where:

t	Time, [s]
t_1	Start time, [s]
t_2	end time, [s]

Collecting the length integral terms from Equation (6.7) into one combined integral simplifies the expression as shown in Equation (E.7).

$$\begin{aligned}\delta \int_{t_1}^{t_2} \Bigg\{ \frac{1}{2}\int_0^L \Big[\rho A_c \dot{w}^2 + \rho I \dot{\psi}^2 - EI\psi'^2 - \kappa G A_c \big(w' - \psi\big)^2 \Big] \,\mathrm{d}x \\ + \frac{1}{2} m \dot{z}^2 - \frac{1}{2} k\big(w(L) - z\big)^2 \Bigg\} \,\mathrm{d}t = 0\end{aligned} \tag{E.7}$$

As all terms of Equation (6.8) is timed by a half, this constant scaling is removed in Equation (6.9).

$$\begin{aligned}\delta \int_{t_1}^{t_2} \Bigg\{ \int_0^L \Big[\rho A_c \dot{w}^2 + \rho I \dot{\psi}^2 - EI\psi'^2 - \kappa G A_c \big(w' - \psi\big)^2 \Big] \,\mathrm{d}x \\ + m \dot{z}^2 - k\big(w(L) - z\big)^2 \Bigg\} \,\mathrm{d}t = 0\end{aligned} \tag{E.8}$$

The delta operator is used to indicate the first variation. The variation of variables is carried out in Equation (E.9).

$$\begin{aligned}\int_{t_1}^{t_2}\left\{\int_0^L\Big[\rho A_c\dot{w}\,\delta\dot{w}+\rho I\dot{\psi}\,\delta\dot{\psi}-EI\psi'\,\delta\psi'-\kappa GA_c\big(w'-\psi\big)\big(\delta w'-\delta\psi\big)\Big]\,\mathrm{d}x\right.\\ \left.+m\dot{z}\,\delta\dot{z}-k\big(w(L)-z\big)\big(\delta w(L)-\delta z\big)\right\}\mathrm{d}t=0\end{aligned} \tag{E.9}$$

To solve the variation of variables, integration by parts is utilized. The method of integration by parts is explained in Section 6.1, and the result is stated in Equation (E.10)

$$\begin{aligned}\int_{t_1}^{t_2}\left\{\int_0^L\Big[-\rho A_c\ddot{w}\,\delta w-\rho I\ddot{\psi}\,\delta\psi+EI\psi''\,\delta\psi+\kappa GA_c\big(w''-\psi'\big)\delta w\right.\\ +\kappa GA_c\big(w'-\psi\big)\delta\psi\Big]\,\mathrm{d}x-m\ddot{z}\,\delta z-kw(L)\,\delta w(L)+kz\,\delta w(L)\\ \left.+kw(L)\,\delta z-kz\,\delta z-\kappa GA_c\big(w'(L)-\psi(L)\big)\delta w(L)\right\}\mathrm{d}t=0\end{aligned} \tag{E.10}$$

The parts in Equation (E.10) that contain common variational terms are grouped in Equation (E.11).

$$\begin{aligned}\int_{t_1}^{t_2}\left\{\int_0^L\Big[\big(\kappa GA_c\big(w''-\psi'\big)-\rho A_c\ddot{w}\big)\delta w+\big(\kappa GA_c\big(w'-\psi\big)-\rho I\ddot{\psi}+EI\psi''\big)\delta\psi\Big]\,\mathrm{d}x\right.\\ \left.\big(kw(L)-kz-m\ddot{z}\big)\delta z+\Big(kz-kw(L)-\kappa GA_c\big(w'(L)-\psi(L)\big)\Big)\delta w(L)\right\}\mathrm{d}t=0\end{aligned} \tag{E.11}$$

As Equation (E.11) has to be equal to zero and the four terms δw, $\delta w(L)$, $\delta\psi$, and δz are arbitrary of value, the rest of the four terms must be equal to zero. Thus four equations can be derived and these are stated in Equation (E.12) to Equation (E.15).

$$\kappa GA_c\big(w''-\psi'\big)-\rho A_c\ddot{w}=0 \tag{E.12}$$

$$\kappa GA_c\big(w'-\psi\big)-\rho I\ddot{\psi}+EI\psi''=0 \tag{E.13}$$

$$kw(L)-kz-m\ddot{z}=0 \tag{E.14}$$

$$kz-kw(L)-\kappa GA_c\big(w'(L)-\psi(L)\big)=0 \tag{E.15}$$

Equation (E.12) to Equation (E.15) is no longer terms of energy but is purely force and moment equilibrium, thus the applied load and damper force can be added according to the Rayleighs dissipation function as explained in Section 6.1. The damping force acts opposite to the direction of the relative movement of the mass and the beam. The force and damping force is added to Equation (E.14) as this equation describes motion of the mass. The damping force is additionally added to Equation (E.15) as this equation describes motion of the beam tip.

$$\kappa GA_c\big(w''-\psi'\big)-\rho A_c\ddot{w}=0 \tag{E.16}$$

$$\kappa GA_c\big(w'-\psi\big)-\rho I\ddot{\psi}+EI\psi''=0 \tag{E.17}$$

$$kz-kw(L)+m\ddot{z}+c\big(\dot{z}-\dot{w}(L)\big)=F \tag{E.18}$$

$$kz-kw(L)-\kappa GA_c\big(w'(L)-\psi(L)\big)-c\big(\dot{w}(L)-\dot{z}\big)=0 \tag{E.19}$$

The deflection $w(x,t)$ and angle deflection $\psi(x,t)$ in Equation (E.16), (E.17), (E.18), and (E.19) is found by the method separation of variables as stated in Equation (E.20) and Equation (E.21).

$$w(x) = W(x)\,\mathrm{e}^{i\omega t} \tag{E.20}$$

$$\psi(x) = \Psi(x)\,\mathrm{e}^{i\omega t} \tag{E.21}$$

where:

$W(x)$	Assumed solution for the beam deflection, [m]
$\Psi(x)$	Assumed solution for the beam angular displacement, [-]

A solution for the deflection and angle deflection as a function of the beam length, x, is stated in Equation (E.22) and Equation (E.23).

$$W(x) = \beta\,\mathrm{e}^{\lambda x} \tag{E.22}$$

$$\Psi(x) = \gamma\,\mathrm{e}^{\lambda x} \tag{E.23}$$

Inserting Equation (E.22) and Equation (E.23) into Equation (E.20) and Equation (E.21) gives the initial assumed solution using the method of separation of variables.

$$w(x) = \beta\,\mathrm{e}^{\lambda x}\,\mathrm{e}^{i\omega t} \tag{E.24}$$

$$\psi(x) = \gamma\,\mathrm{e}^{\lambda x}\,\mathrm{e}^{i\omega t} \tag{E.25}$$

Equation (E.24) and Equation (E.25) is inserted into Equation (E.16) and Equation (E.17) to attemp to find a final solution for the deflection and angle deflection.

$$\kappa G A_c \lambda^2 \beta\,\mathrm{e}^{\lambda x}\,\mathrm{e}^{i\omega t} - \kappa G A_c \lambda \gamma\,\mathrm{e}^{\lambda x}\,\mathrm{e}^{i\omega t} + \rho A_c \omega^2 \beta\,\mathrm{e}^{\lambda x}\,\mathrm{e}^{i\omega t} = 0 \tag{E.26}$$

$$\kappa G A_c \lambda \beta\,\mathrm{e}^{\lambda x}\,\mathrm{e}^{i\omega t} - \kappa G A_c \gamma\,\mathrm{e}^{\lambda x}\,\mathrm{e}^{i\omega t} + \rho I \omega^2 \gamma\,\mathrm{e}^{\lambda x}\,\mathrm{e}^{i\omega t} + E I \lambda^2 \gamma\,\mathrm{e}^{\lambda x}\,\mathrm{e}^{i\omega t} = 0 \tag{E.27}$$

The exponential terms can be canceled out, which simplifies Equation (E.26) and Equation (E.27).

$$\kappa G A_c \lambda^2 \beta - \kappa G A_c \lambda \gamma + \rho A_c \omega^2 \beta = 0 \tag{E.28}$$

$$\kappa G A_c \lambda \beta - \kappa G A_c \gamma + \rho I \omega^2 \gamma + E I \lambda^2 \gamma = 0 \tag{E.29}$$

To find a solution for λ and to find this solution it is necessary to set the two equation up in matrix form as stated in Equation (E.30).

$$\begin{bmatrix} \kappa G A_c \lambda^2 \beta + \rho A_c \omega^2 \beta & -\kappa G A_c \lambda \gamma \\ \kappa G A_c \lambda \beta & \rho I \omega^2 \gamma + E I \lambda^2 \gamma - \kappa G A_c \gamma \end{bmatrix} \tag{E.30}$$

The determinant of the two by two matriw is found and is stated in Equation (E.31).

$$A_c\beta\gamma I\omega^4\rho^2 - A_c^2\beta\gamma G\kappa\omega^2\rho + A_c\beta\gamma EGI\kappa\lambda^4 + A_c\beta\gamma EI\lambda^2\omega^2\rho + A_c\beta\gamma GI\kappa\lambda^2\omega^2\rho = 0 \tag{E.31}$$

The determinant is solved according to λ, which yields four equations. If the material parameters and beam parameters is inserted to the equations, it is possible to find four solutions for λ and these are stated in Equation (E.32) when the parameters from Table E.1 is used.

$$\begin{array}{rcrcr} 0 & + & 1.1446i & = & \lambda_1 \\ 1.1439 & + & 0 & = & \lambda_2 \\ 0 & - & 1.1446i & = & -\lambda_1 \\ -1.1439 & + & 0 & = & -\lambda_2 \end{array} \tag{E.32}$$

Model test parameters			
E	$70GPa$	ρ	$2700\frac{kg}{m^3}$
L	$2m$	d	$0.06m$
m	$0.0001kg$	c	$0\frac{N\,s}{m}$
k	$10^{10}\frac{N}{m}$	F	100N
ν	0.25	G	$\frac{E}{2(1+\nu)} = 28GPa$
κ	$\frac{6(1+\nu)}{7+6\nu} = 0.8824$	ω	$100\frac{rad}{s}$

Table E.1 Input parameters used to find values of λ.

By considering the results of solving Equation (E.31) according to λ it is possible to see that λ can be expanded to λ_1 and λ_2 as shown in Equation (E.32). Hence it is not possible to state only one constant of λ in Equation (E.24). Thus Equation (E.24) is expanded to contain both λ_1 and λ_2 as stated in Equation (E.33).

$$W(x) = \beta_1\,\mathrm{e}^{\lambda_2 x} + \beta_2\,\mathrm{e}^{-\lambda_2 x} + \beta_3\,\mathrm{e}^{i\lambda_1 x} + \beta_4\,\mathrm{e}^{-i\lambda_1 x} \tag{E.33}$$

The shape function of the Timoshenko beam stated in Equation (E.33) can be expressed by sine and cosine terms as stated in Equation (E.34).

$$W(x) = \beta_1\cosh(\lambda_2 x) + \beta_2\sinh(\lambda_2 x) + \beta_3\cos(\lambda_1 x) + \beta_4\sin(\lambda_1 x) \tag{E.34}$$

The same expansion and reformulation of Ψ, stated in Equation (E.25), can be carried out. The results is stated in Equation (E.35).

$$\Psi(x) = \gamma_1\cosh(\lambda_2 x) + \gamma_2\sinh(\lambda_2 x) + \gamma_3\cos(\lambda_1 x) + \gamma_4\sin(\lambda_1 x) \tag{E.35}$$

The system is now based on five equations but nine unknowns, so it is not yet possible to find a solution. To reduce the number of unknowns, the constants γ_i can be calculated from the constants β_i, material parameters, and beam parameters. This is done by using Equation (E.16) where Equation (E.34) and Equation (E.35) is inserted as stated in Equation (E.36).

$$\begin{aligned}\kappa G A_c\Big(\beta_1\lambda_2^2\cosh(\lambda_2 x)+\beta_2\lambda_2^2\sinh(\lambda_2 x)-\beta_3\lambda_1^2\cos(\lambda_1 x)-\beta_4\lambda_1^2\sin(\lambda_1 x)\Big)\\ -\kappa G A_c\Big(\gamma_1\lambda_2\cosh(\lambda_2 x)+\gamma_2\lambda_2\sinh(\lambda_2 x)-\gamma_3\lambda_1\cos(\lambda_1 x)-\gamma_4\lambda_1\sin(\lambda_1 x)\Big)\\ +\omega^2\rho A_c\Big(\beta_1\cosh(\lambda_2 x)+\beta_2\sinh(\lambda_2 x)-\beta_3\cos(\lambda_1 x)-\beta_4\sin(\lambda_1 x)\Big)=0\end{aligned}\tag{E.36}$$

In Equation (E.36) each part of the equation either contain a cosine, sine, hyperbolic cosine, or hyperbolic sine part which is most likely not equal to zero, why all parts in front of fx. cosine must be equal to zero as stated in Equation (E.37). This is done for every sine and cosine term and is stated in Equation (E.37) through Equation (E.40).

$$\kappa G A_c\beta_1\lambda_2^2-\kappa G A_c\gamma_2\lambda_2+\rho A_c\beta_1\omega^2=0\tag{E.37}$$
$$\kappa G A_c\beta_2\lambda_2^2-\kappa G A_c\gamma_1\lambda_2+\rho A_c\beta_2\omega^2=0\tag{E.38}$$
$$-\kappa G A_c\beta_3\lambda_1^2-\kappa G A_c\gamma_4\lambda_1+\rho A_c\beta_3\omega^2=0\tag{E.39}$$
$$-\kappa G A_c\beta_4\lambda_1^2+\kappa G A_c\gamma_3\lambda_1+\rho A_c\beta_4\omega^2=0\tag{E.40}$$

As each of the equations (E.37) through Equation (E.40) only contain one of the of the γ constants, it is possible to isolate γ_i in each equation. This is done in Equation (E.41) to Equation (E.44).

$$\frac{\kappa G\beta_1\lambda_2^2+\rho\beta_1\omega^2}{\kappa G\lambda_2}=\gamma_2\tag{E.41}$$
$$\frac{\kappa G\beta_2\lambda_2^2+\rho\beta_2\omega^2}{\kappa G\lambda_2}=\gamma_1\tag{E.42}$$
$$\frac{\rho\beta_3\omega^2-\kappa G\beta_3\lambda_1^2}{\kappa G\lambda_1}=\gamma_4\tag{E.43}$$
$$\frac{\kappa G\beta_4\lambda_1^2-\rho\beta_4\omega^2}{\kappa G\lambda_1}=\gamma_3\tag{E.44}$$

Inserting Equation (E.41) to Equation (E.44) into Equation (E.35) yields a new expression of $\Psi(x)$ where the constant γ is replaced, as stated in Equation (E.45).

$$\begin{aligned}\Psi(x)=&\frac{\kappa G\beta_2\lambda_2^2+\rho\beta_2\omega^2}{\kappa G\lambda_2}\cos(\lambda_1 x)+\frac{\kappa G\beta_1\lambda_2^2+\rho\beta_1\omega^2}{\kappa G\lambda_2}\sin(\lambda_1 x)\\ &+\frac{\kappa G\beta_4\lambda_1^2-\rho\beta_4\omega^2}{\kappa G\lambda_1}\cosh(\lambda_2 x)+\frac{\rho\beta_3\omega^2-\kappa G\beta_3\lambda_1^2}{\kappa G\lambda_1}\sinh(\lambda_2 x)\end{aligned}\tag{E.45}$$

Equation (E.16) and Equation (E.17) is used to find two solutions for beam deflection and angle deflection. Where Equation (E.18) and Equation (E.19) is used as two of the five equations to find the five unknowns along with the boundary conditions stated in Equation (E.1) to Equation (E.3). The five equations is restated in Equation (E.46) and Equation (E.48).

$$kz - kw(L) + m\ddot{z} + c\big(\dot{z} - \dot{w}(L)\big) = F \tag{E.46}$$

$$kz - kw(L) - \kappa G A_c\big(w'(L) - \psi(L)\big) - c\big(\dot{w}(L) - \dot{z}\big) = 0 \tag{E.47}$$

$$w(0,t) = 0 \tag{E.48}$$

$$\psi(0) = 0 \tag{E.49}$$

$$\psi'(0) = 0 \tag{E.50}$$

The deflection of the mass is also dependent on the time as stated in Equation (E.49).

$$z(t) = Z_0\,\mathrm{e}^{i\omega t} \tag{E.51}$$

where:

Z_0 | The amplitude of motion of the mass, [m]

The applied force is a oscillating force that is time dependent as stated in Equation (E.50).

$$F(t) = F_0\,\mathrm{e}^{i\omega t} \tag{E.52}$$

where:

F_0 | The amplitude of the applied force, [N]

Inserting Equation (E.45) and Equation (E.34) into Equation (E.20) and Equation (E.21) yields the final expressions for the deflection and angle deflection.

$$w(x) = \Big(\beta_1\cos(\lambda_1 x) + \beta_2\sin(\lambda_1 x) + \beta_3\cosh(\lambda_2 x) + \beta_4\sinh(\lambda_2 x)\Big)\,\mathrm{e}^{i\omega t} \tag{E.53}$$

$$\begin{aligned}\psi(x) = \Bigg(&\frac{\kappa G\beta_2\lambda_2^2 + \rho\beta_2\omega^2}{\kappa G\lambda_2}\cos(\lambda_1 x) + \frac{\kappa G\beta_1\lambda_2^2 + \rho\beta_1\omega^2}{\kappa G\lambda_2}\sin(\lambda_1 x)\\ &+\frac{\kappa G\beta_4\lambda_1^2 - \rho\beta_4\omega^2}{\kappa G\lambda_1}\cosh(\lambda_2 x) + \frac{\rho\beta_3\omega^2 - \kappa G\beta_3\lambda_1^2}{\kappa G\lambda_1}\sinh(\lambda_2 x)\Bigg)\,\mathrm{e}^{i\omega t}\end{aligned} \tag{E.54}$$

The derivatives need in Equation (E.46) and Equation (E.48) is stated below.

$$\dot{z} = i\omega Z_0\,\mathrm{e}^{i\omega t} \tag{E.55}$$

$$\ddot{z} = -\omega^2 Z_0\,\mathrm{e}^{i\omega t} \tag{E.56}$$

$$\dot{w} = i\omega W(x)\,\mathrm{e}^{i\omega t} \tag{E.57}$$

$$w' = W'(x)\,\mathrm{e}^{i\omega t} \tag{E.58}$$

$$\psi' = \Psi'(x)\,\mathrm{e}^{i\omega t} \tag{E.59}$$

The derivatives is then inserted into Equation (E.46) and Equation (E.48) and it is seen that every part contains the exponential expression.

$$kZ_0\,\mathrm{e}^{i\omega t} - kW(L)\,\mathrm{e}^{i\omega t} - m\omega^2 Z_0\,\mathrm{e}^{i\omega t} + c\big(i\omega Z_0\,\mathrm{e}^{i\omega t} - i\omega W(x)\,\mathrm{e}^{i\omega t}\big) = F \tag{E.60}$$

$$\begin{split} kZ_0\,\mathrm{e}^{i\omega t} - kW(L)\,\mathrm{e}^{i\omega t} - \kappa G A_c\big(W'(x)\,\mathrm{e}^{i\omega t} - \Psi(L)\,\mathrm{e}^{i\omega t}\big) \\ -c\big(i\omega W(x)\,\mathrm{e}^{i\omega t} - i\omega Z_0\,\mathrm{e}^{i\omega t}\big) = 0 \end{split} \tag{E.61}$$

$$W(0)\,\mathrm{e}^{i\omega t} = 0 \tag{E.62}$$

$$\Psi(0)\,\mathrm{e}^{i\omega t} = 0 \tag{E.63}$$

$$\Psi'(L)\,\mathrm{e}^{i\omega t} = 0 \tag{E.64}$$

The exponential expression is canceled out, which means that the equation of motion is no longer dependent on time.

$$kZ_0 - kW(L) - m\omega^2 Z_0 + c\big(i\omega Z_0 - i\omega W(x)\big) = F \tag{E.65}$$

$$kZ_0 - kW(L) - \kappa G A_c\big(W'(x) - \Psi(L)\big) - c\big(i\omega W(x) - i\omega Z_0\big) = 0 \tag{E.66}$$

$$W(0) = 0 \tag{E.67}$$

$$\Psi(0) = 0 \tag{E.68}$$

$$\Psi'(L) = 0 \tag{E.69}$$

The five equations in Equation (E.65) and Equation (E.69) is solved to find a solution for a specific frequency. By doing so for a span of frequencies and finding the amplitude, the eigenfrequencies are located by evaluating the amplitude.

E.2 Verification of Timoshenko model

The Bernoulli-Euler model is compared to elementary models and yields exact solutions. Thus it is not requisite to compare the Timoshenko model to elementary models but only to the Bernoulli-Euler model. It is expected that the Timoshenko model and the Bernoulli-Euler model yields the same results for the first eigenfrequency but for higher order resonance it is expected that the Timoshenko model yields results that are lower compared to Bernoulli-Euler.

E.2.1 Beam verification

Initially the beam part is verified by using the parameters stated in Table E.1. The response is calculated for frequencies from 0Hz to 400Hz with intervals of 2Hz. At frequencies close to the expected modal frequencies a finer discretization, of 0.025Hz, is used. The response of the Timoshenko beam can be seen on Figure E.1.

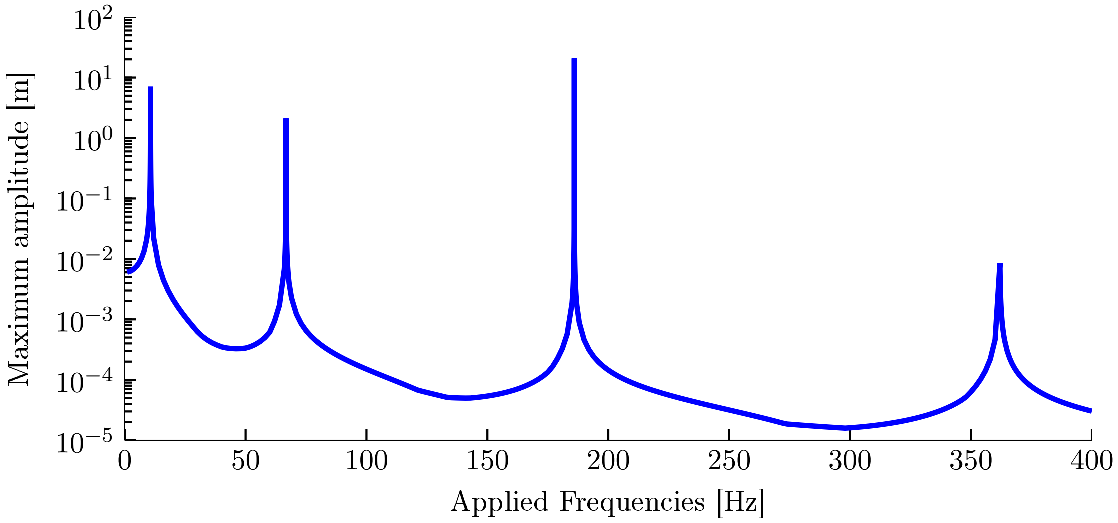

Figure E.1 The eigenfrequencies of the Timoshenko beam when the mass and spring is decoupled.

If the frequencies from the two different analytical models are compared, it is seen from Table E.2 that the first modal frequency is identical and the rest of the Timoeshenko eigenfrequencies are lower than those found with Bernoulli-Euler theory. Thus it is considered that the beam part of the model is correct.

Mode	Bernoulli-Euler	Timoshenko
1	10.68	10.68
2	66.96	66.73
3	187.49	185.95
4	367.41	362.0

Table E.2 The modal frequencies from the two analytical models.

E.2.2 Spring/mass verification

The spring/mass part of the system is solved as well where the beam is set to be so stiff that it acts as ground and thereby considered as decoupled from the system. The parameters used during the calculation of the response is stated in Table E.3.

Model test parameters			
E	$1000GPa$	ρ	$1\frac{kg}{m^3}$
L	$2m$	d	$1m$
I	$\frac{\pi}{64}d^4 = 0.04909m^4$	A_c	$\frac{\pi}{4}d^2 = 0.7854m^2$
m	$0.5kg$	c	$0\frac{N\,s}{m}$
k	$8000\frac{N}{m}$	ν	0.25
G	$\frac{E}{(2(1+\nu))} = 333.3GPa$	κ	$\frac{6(1+\nu)}{7+6\nu} = 0.9$

Table E.3 Input parameters for the analytical model for verifying the spring/mass part of the model.

The calculated response for the spring/mass system is seen in Figure E.2 and the eigenfrequency is found to 20.13Hz indicated by the peak. This results is the exact same as the Bernoulli-Euler model and the general solutions. Thus the spring/mass part is considered as valid.

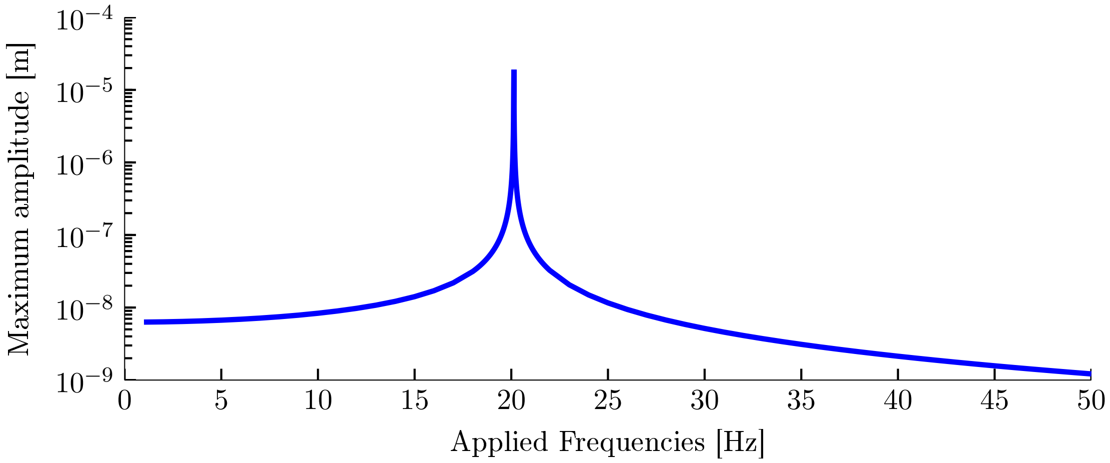

Figure E.2 The eigenfrequencies of the Timoshenko spring/mass when the beam is decoupled.

E.2.3 verification of coupled system

The model has now been tested both where each part of the system is decoupled and verified according to solutions from the Bernoulli-Euler. During this section the coupled system is going to be tested, to see if the system produce acceptable results. Furthermore the system is tested by letting the eigenfrequency of the beam and spring/mass system being very close to each other.

Initially the coupled system is solved for parameters stated in Table E.4. The coupled system is expected to show a eigenfrequency of the mass and beam and between the two eigenfrequencies an antiressonance is expected to appear.

Model test parameters			
E	$200GPa$	ρ	$7800\frac{kg}{m^3}$
L	$1m$	d	$0.06m$
m	$0.5kg$	c	$0\frac{N\,s}{m}$
k	$10000\frac{N}{m}$	ν	0.3
G	$\frac{E}{(2(1+\nu))} = 79.92GPa$	κ	$\frac{6(1+\nu)}{7+6\nu} = 0.886$

Table E.4 Input parameters for the coupled Timoshenko model.

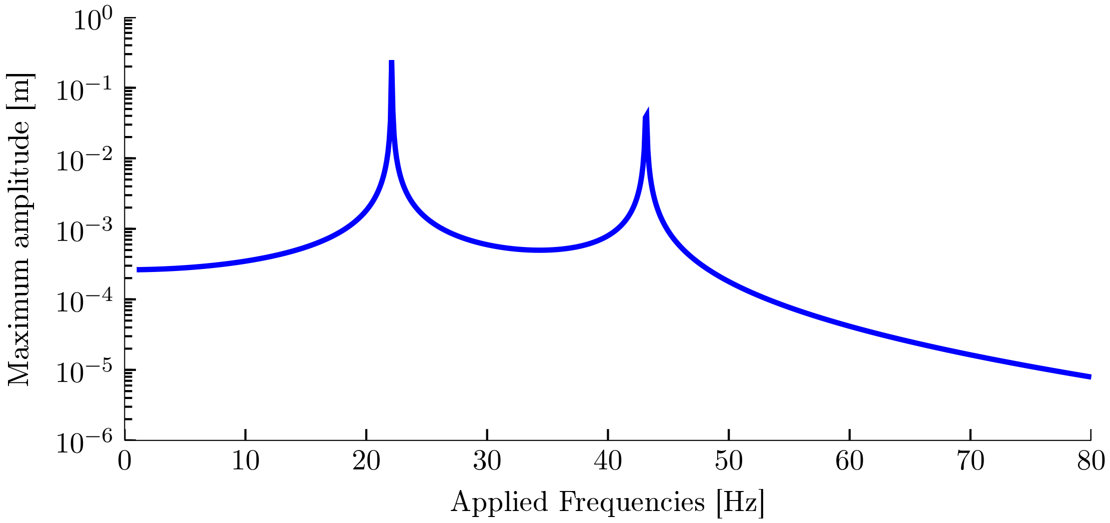

Figure E.3 The eigenfrequencies of the Timoshenko spring/mass when the beam is decoupled.

The system response is calculated for a frequency range of 0Hz to 80Hz with intervals of 0.1Hz. The calculated response of the the beam is seen in Figure E.3 and the deflection of the mass is seen in Figure E.4. The two eigenfrequencies is located at 22.51Hz and 43.2Hz which is the exact same as the Bernoulli-Euler model.

The anti resonance is also located at the same position as the the Bernoulli-Euler solution by comparing Figure D.4 and Figure E.4.

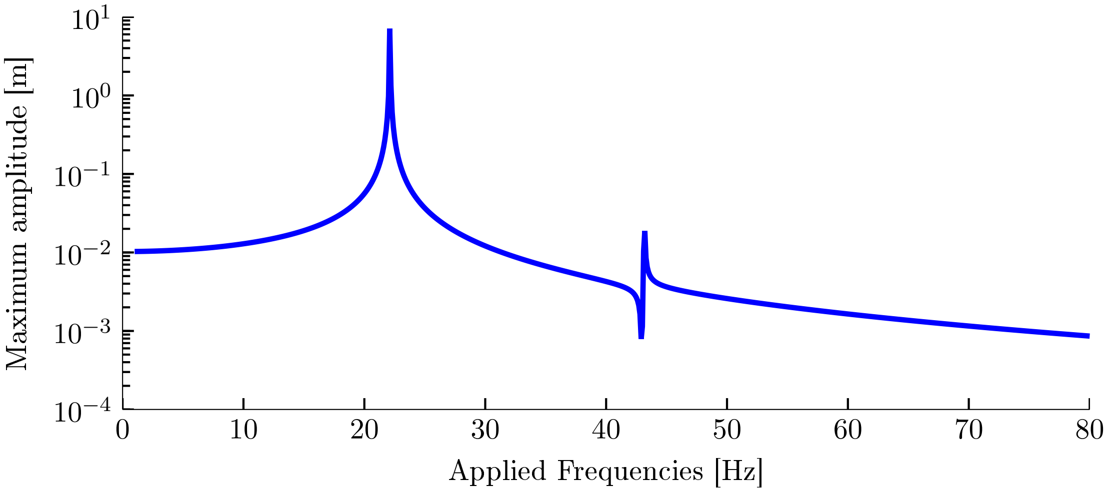

Figure E.4 The eigenfrequencies of the Timoshenko spring/mass when the beam is decoupled.

The coupled Timoshenko system is considered as yielding correct results. Hence it is still necessary to investigate what happens when the eigenfrequency of the spring/mass and the first eigenfrequency of the beam is very close.

By using the parameters in Table E.4, the first eigenfrequency of the beam is found to 42.5Hz and by increasing the spring constant to $k = 36000\frac{N}{m}$ the eigenfrequency of the spring/mass is 42.7Hz. The calculated response of the system with two close eigenfrequencies is seen on Figure E.5 and Figure E.6, where it is seen that the frequencies is pushed away from each other. This change in frequencies equivalent to the one observed in Appendix D.3. Thus it is considered that the Timoshenko model i valid and can be used in replacement of the Bernoulli-Euler model as it yields better solutions for higher order modes.

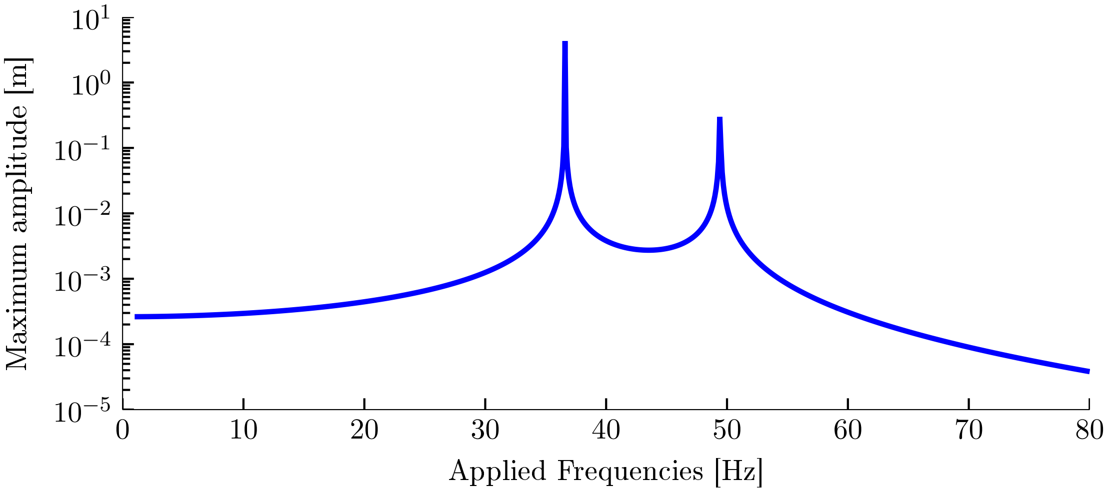

Figure E.5 The eigenfrequencies of the Timoshenko spring/mass when the beam is decoupled.

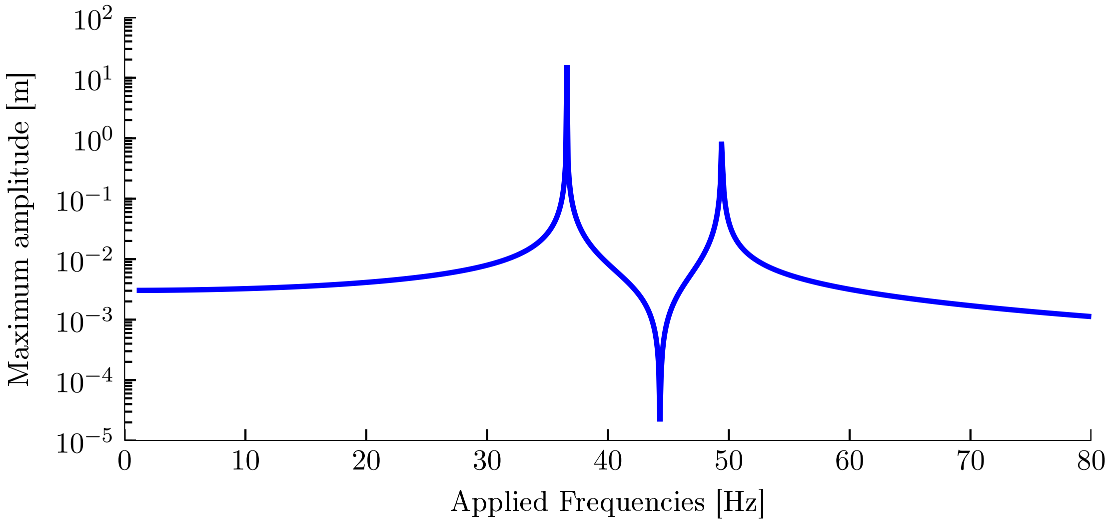

Figure E.6 The eigenfrequencies of the Timoshenko spring/mass when the beam is decoupled.

E.3 Damper Response

During this section the response of the Timoshenko model is evaluated, when the beam is decoupled and a damper is added. The response is initially seen in Figure 6.7, but in order to see the response for each individual damping constant more clearly, each results is plotted individually below. The damping constants are stated in Table 6.1.

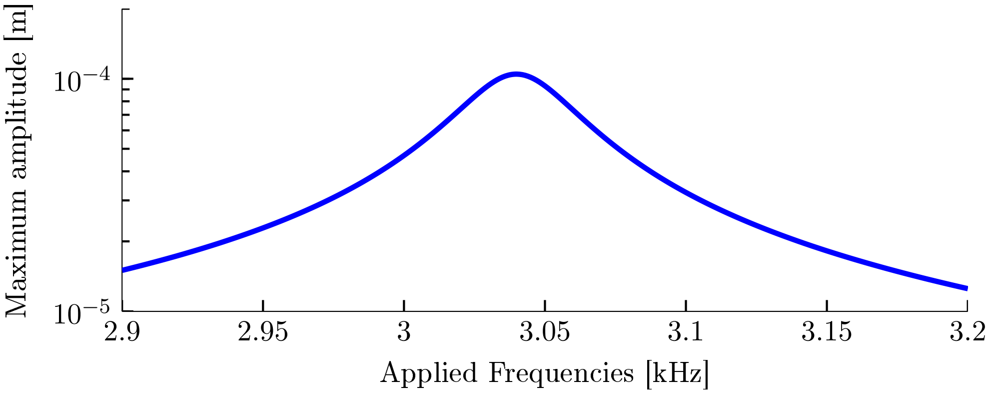

Figure E.7 Response obtained of the spring/mass/damper system with a damping constant of $10\frac{Ns}{m}$.

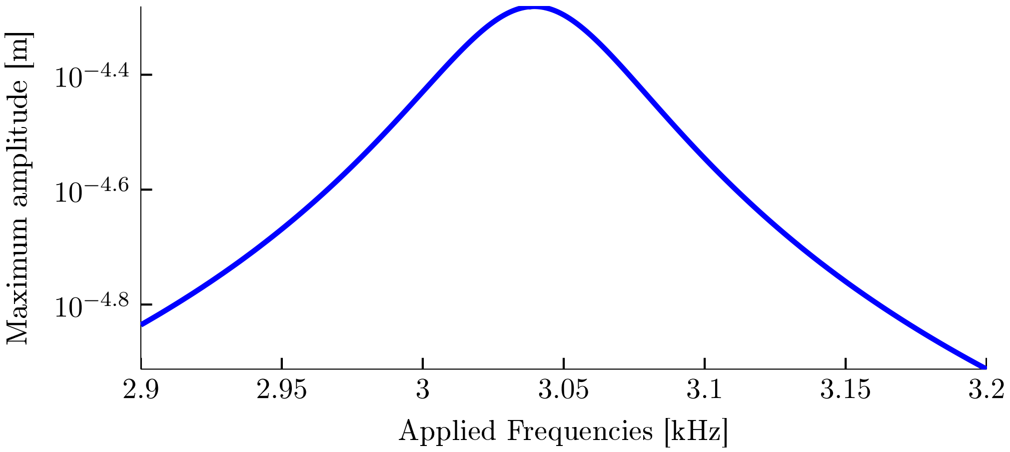

Figure E.8 Response obtained of the spring/mass/damper system with a damping constant of $20\frac{Ns}{m}$.

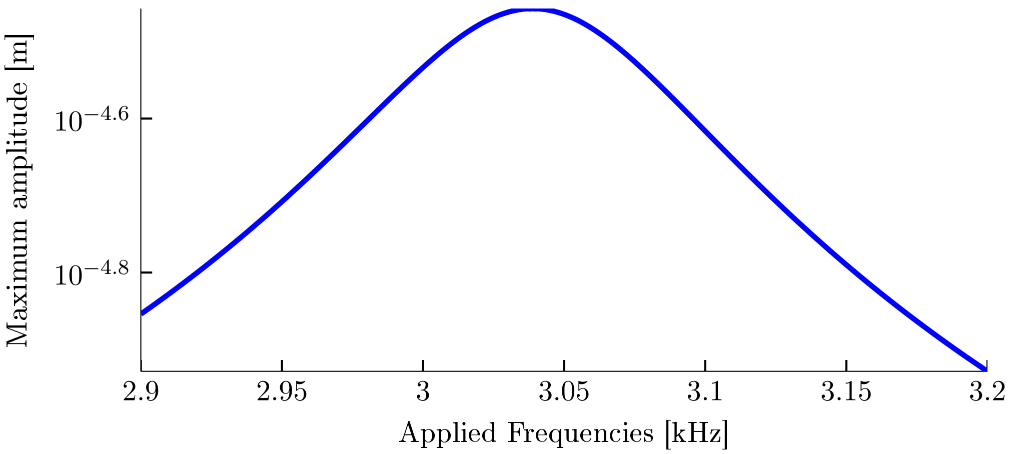

Figure E.9 Response obtained of the spring/mass/damper system with a damping constant of $30 \frac{Ns}{m}$.

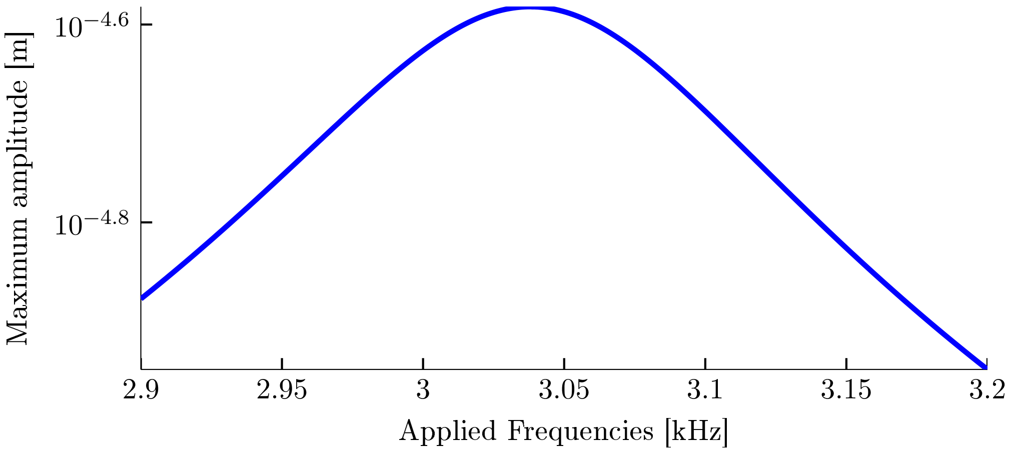

Figure E.10 Response obtained of the spring/mass/damper system with a damping constant of $40 \frac{Ns}{m}$.

E.4 Eigenfrequency

$$\begin{bmatrix} \frac{\rho(f2\pi)^2+G\kappa\lambda_1^2}{G\kappa} & 0 & \frac{\rho(f2\pi)^2-G\kappa\lambda_2^2}{G\kappa} & 0 \\ 0 & \lambda_1-\frac{\rho(f2\pi)^2+G\kappa\lambda_1^2}{G\kappa\lambda_1} & 0 & \lambda_2-\frac{G\kappa\lambda_2^2-\rho(f2\pi)^2}{G\kappa\lambda_2} \\ \cosh(\lambda_1 L)\,\frac{\rho(f2\pi)^2+G\kappa\lambda_1^2}{G\kappa} & \sinh(\lambda_1 L)\,\frac{\rho(f2\pi)^2+G\kappa\lambda_1^2}{G\kappa} & \cos(\lambda_2 L)\,\frac{\rho(f2\pi)^2-G\kappa\lambda_2^2}{G\kappa} & \sin(\lambda_2 L)\,\frac{\rho(f2\pi)^2-G\kappa\lambda_2^2}{G*\kappa} \\ \sinh(\lambda_1 L)\left(\lambda_1-\frac{\rho(f2\pi)^2+G\kappa\lambda_1^2}{G\kappa\lambda_1}\right) & \cosh(\lambda_1 L)\left(\lambda_1-\frac{\rho(f2\pi)^2+G\kappa\lambda_1^2}{G\kappa\lambda_1}\right) & \sin(\lambda_2 L)\left(-\lambda_2-\frac{\rho(f2\pi)^2-G\kappa\lambda_2^2}{G\kappa\lambda_2}\right) & \cos(\lambda_2 L)\left(\lambda_2-\frac{G\kappa\lambda_2^2-\rho(f2\pi)^2}{G\kappa\lambda_2}\right) \end{bmatrix} \tag{E.70}$$

E.5 Harmonic excitation damping

This section derives the expression for damped eigenfreqiencies for harmonically excited structures. Which is used to verify the analytical model. The amplitude ratio stated in Equation (E.71), describes the response of damped system under harmonic forcing.

$$M = \frac{1}{\left[\left(1-\left(\frac{\omega}{\omega_r}\right)^2\right)^2 + \left(2\zeta\frac{\omega}{\omega_r}\right)^2\right]^{\frac{1}{2}}} \tag{E.71}$$

where: citepbib:rao

M	Amplitude ratio, [-]

The eigenfrequency can be found from the amplitude ratio by finding the derivative according to the frequency when the slope is equal to zero, as stated in Equation (E.73).

$$\frac{\mathrm{d}M}{\mathrm{d}\omega} = 0 \tag{E.72}$$

The derivative of the amplitude ratio is found in Equation (E.73).

$$\begin{aligned} \frac{\mathrm{d}M}{\mathrm{d}\omega} = -\frac{1}{2}\frac{1}{\left[\left(1-\left(\frac{\omega}{\omega_r}\right)^2\right)^2 + \left(2\zeta\frac{\omega}{\omega_r}\right)^2\right]^{\frac{3}{2}}} \\ \left[2\left(1-\left(\frac{\omega}{\omega_r}\right)^2\right)\left(-\frac{2\omega}{\omega_r^2}\right) + 2\cdot 2\zeta\frac{\omega}{\omega_r}2\zeta\frac{1}{\omega_r}\right] = 0 \end{aligned} \tag{E.73}$$

Equation (E.73) can be simplified by neglecting the fraction, as it will never be equal to zero, and collecting terms.

$$-\frac{4\omega}{\omega_r^2}\left(1-\frac{\omega^2}{\omega_r^2}\right) + 8\zeta^2\frac{\omega}{\omega_r^2} = 0 \tag{E.74}$$

Equation (E.74) is simplified even further by dividing both terms with $-\frac{4\omega}{\omega_r^2}$ and the new expression obtained is stated in Equation (E.75) and Equation (E.76).

$$1-\frac{\omega^2}{\omega_r^2} - 2\zeta^2 = 0 \tag{E.75}$$

Moving $\frac{\omega^2}{\omega_r^2}$ to the other side of the equality.

$$1-\frac{\omega^2}{\omega_r^2} = 2\zeta^2 \tag{E.76}$$

$$\frac{\omega^2}{\omega_r^2} = 1-2\zeta^2 \tag{E.77}$$

Equation (E.77) is solved for ω to obtain a solution for the damped eigenfrequency, as stated in Equation (E.78). The negative solution and the solution at zero are neglected, as the solution at $\omega = 0$ is not a eigenfrequency.

$$\omega = \omega_r \sqrt{1 - 2\zeta^2} \tag{E.78}$$

An expression for the damped harmonically excited eigenfrequency is now obtained.